THESIS FOR THE DEGREE OF DOCTOR OF PHILOSOPHY

Dielectrically Loaded Quad-ridge Flared Horns for Ultra Wideband Reflector Feed Applications in Radio Astronomy

Jonas Flygare

Department of Space, Earth and Environment
Chalmers University of Technology
Gothenburg, Sweden, 2022

Dielectrically Loaded Quad-ridge Flared Horns for Ultra Wideband Reflector Feed Applications in Radio Astronomy

Jonas Flygare
ISBN 978-91-7905-649-0

Contact author: jonas.b.flygare@gmail.com

Doktorsavhandlingar vid Chalmers tekniska högskola
Ny serie nr 5115
ISSN 0346-718X

Department of Space, Earth and Environment
Chalmers University of Technology
SE-412 96 Gothenburg, Sweden
Phone: +46 (0)31 772 1000

Cover:
An ultra wideband quad-ridge flared horn with a dielectric load.

Printed by Chalmers Reproservice
Gothenburg, Sweden, March 2022

Come out to the coast, we'll get together, have a few laughs...

Dielectrically Loaded Quad-ridge Flared Horns for Ultra Wideband Reflector Feed Applications in Radio Astronomy

Jonas Flygare
Department of Space, Earth and Environment
Chalmers University of Technology

Abstract

Reflector-based radio telescopes are used as tools for observations in both radio astronomy and space geodesy. To observe the weak sources in space, highly sensitive receivers, fronted by optimized reflector feeds, are therefore needed. Wideband and ultra-wideband (UWB) systems enable large continuous frequency bandwidth and reduce the number of receivers that are needed to cover the radio spectrum. Therefore, they are attractive for existing and next generation of reflector arrays such as the Square Kilometre Array (SKA), Allen Telescope Array (ATA), Deep Synoptic Array (DSA), and the Next Generation Very Large Array (ngVLA). To achieve sensitive wideband and UWB performance with reflector feeds, a near-constant beamwidth and good impedance match are required over large frequency bands. The quad-ridge flared horn (QRFH) is a robust and compact UWB feed technology for this purpose, and is easily designed with single-ended excitation for 50-Ω ports. The QRFH is dual-linear polarized and can typically achieve good performance up to 6:1 bandwidth with high band-average aperture efficiency and good impedance match. A drawback in existing state-of-the-art QRFH designs, is that they suffer from gradually narrowing beamwidth and increasing cross-polarization in the upper part of the frequency band. This is especially challenging for QRFHs that are designed to illuminate deep reflector geometries. The narrowing beamwidth leads to reduced aperture efficiency, and therefore also reduced sensitivity. To meet the demand for high sensitivity observations over large bandwidths, these challenges need to be addressed. This thesis introduces and investigates low-loss, dielectric loading of the QRFH design to achieve ultra-wideband performance that reaches beyond decade bandwidth exemplified with 20:1 bandwidth in one single QRFH. The dielectric load is homogeneous, with a small and non-intrusive footprint and improves the beamwidth performance over the frequency band, while keeping the complexity low and the QRFH footprint compact. Keeping the QRFH ro-

bustness and compact footprint is favorable for practical receiver installation in real-world applications for radio observations. Three quad-ridge designs with dielectric loading are investigated, both for room temperature and cryogenic applications, and are shown to be highly suitable for wideband operation in existing and future reflector arrays.

Keywords: quad-ridge flared horn (qrfh), radio astronomy, reflector antenna feeds, ultra wideband antennas, broadband antennas, horn antennas, dielectric materials, dielectric loaded antennas, radio receivers, aperture antennas.

List of Publications

This thesis is based on the following publications:

[**A**] **Jonas Flygare**, Miroslav Pantaleev, and Simon Olvhammar, "BRAND: Ultra-wideband feed development for the European VLBI network - A dielectrically loaded decade bandwidth quad-ridge flared horn". in *Proceedings of the 12th European Conference on Antennas and Propagation (EuCAP)*, London, UK, Apr. 2018.
 DOI: 10.1049/cp.2018.0817

[**B**] **Jonas Flygare** and Miroslav Pantaleev, "Dielectrically Loaded Quad-Ridge Flared Horn for Beamwidth Control Over Decade Bandwidth - Optimization, Manufacture, and Measurement". in *IEEE Transactions on Antennas and Propagation*, vol. 68, no. 1, pp. 207–216, Jan. 2020
 10.1109/TAP.2019.2940529

[**C**] **Jonas Flygare** and Jian Yang, "Strategy and Overview for Development of Beyond-Decade-Bandwidth Quad-ridge Flared Horns for Radio Astronomy". in *Proceedings of the 15th European Conference on Antennas and Propagation (EuCAP)*, Dusseldorf, Germany, Mar. 2021.
 DOI: 10.23919/EuCAP51087.2021.9410964

[**D**] **Jonas Flygare**, Jian Yang, Alexander W. Pollak, Robert E. J. Watkins, Fiona Hillier, Leif Helldner, and Sven-Erik Ferm, "Beyond-decade Ultra-wideband Quad-ridge Flared Horn with Dielectric Load for Beamwidth Stability over 1-20 GHz". *Submitted to IEEE Transactions on Antennas and Propagation*

[**E**] **Jonas Flygare**, Sander Weinreb, and David P. Woody, "Quad-ridge Choke Horn with Dielectric Load as a Wideband Feed for Non-cryogenic Reflector Arrays in Radio Astronomy". *Submitted to IEEE Transactions on Antennas and Propagation*

Other publications by the author, not included in this thesis but sometimes referenced, are:

[F] P. Forkman, **J. Flygare**, and G. Elgered, "Water vapour radiometry in geodetic very long baseline interferometry telescopes: assessed through simulations.". in *Journal of Geodesy*, vol. 95, 117, Oct. 2021.

[G] L. Connor, K. A. Shila, S. R. Kulkarni, **J. Flygare**, G. Hallinan, D. Li, W. Lu, V. Ravi, and S. Weinreb, "Galactic Radio Explorer: An All-sky Monitor for Bright Radio Bursts". in *Publications of the Astronomical Society of the Pacific*, vol. 133 075001, no. 1025, Jul. 2021.

[H] A. Pellegrini, **J. Flygare**, I. P. Theron, R. Lehmensiek, A. Peens-Hough, J. Leech, M. E. Jones, A. C. Taylor, R. E. J. Watkins, L. Liu, A. Hector, B. Du, and Y. Wu, "MID-Radio Telescope, Single Pixel Feed Packages for the Square Kilometer Array: An Overview". in *IEEE Journal of Microwaves*, vol. 1, no. 1, pp. 428–437, Jan. 2021.

[I] K. A. Abdalmalak, G. Santamaria Botello, S. Llorente-Romano, A. Rivera-Lavado, **J. Flygare**, J. A. Lopez Fernandez, J. M. Serna Puente, L. E. Garcia-Castillo, D. Segovia-Vargas, M. Pantaleev, and L. E. Garcia-Munoz, "Ultrawideband Conical Log-Spiral Circularly Polarized Feed for Radio Astronomy". in *IEEE Transactions of Antennas and Propagation*, vol. 68, no. 3, pp. 1995–2007, Mar. 2020.

[J] **J. Flygare**, B. Dong, J. Yang, L. Helldner, M. Dahlgren, J. Chengjin, M. Pantaleev, G. Hovey, and J. Conway, "Wideband single pixel feed system over 4.6–24 GHz for the Square Kilometre Array". in *Proceedings of 2019 International Conference on Electromagnetics in Advanced Applications (ICEAA)*, Granada, Spain, Sep. 2019, pp. 0630–0635.

[K] **J. Flygare**, A. Peens-Hough, L. Helldner, M. Dahlgren, G. Smit; P. Kotze; R. Wingdén, T. D. Carrozi, U. Kylenfall, L. Pettersson, M. Pantaleev, "Sensitivity simulation and measurement of the SKA Band 1 wideband feed package on MeerKAT". in *Proceedings of the 13th European Conference on Antennas and Propagation (EuCAP)*, Krakow, Poland, Apr. 2019.

[L] W. Alef, G. Tuccari, S. Dornbusch, A. L. Roy, M. Wunderlich, C. Kasemann, M. Nalbach, M. Pantaleev, **J. Flygare**, J. D. Gallego, J. A. López Pérez,

F. Tercero Martínez, G. W. Schoonderbeek, J. Hargreaves, R. de Wild, and V. Bezrukovs, "BRAND – A Wideband Receiver for Astronomy and Geodesy". in *Proceedings of the 24th European VLBI Group for Geodesy and Astrometry Working Meeting (EVGA)*, Mar. 2019, pp. 31–36.

[M] B. Dong, J. Yang, J. Dahlström, **J. Flygare**, M. Pantaleev, B. Billade, "Optimization and Realization of Quadruple-ridge Flared Horn with New Spline-defined Profiles as a High-efficiency Feed over 4.6-24 GHz". in *IEEE Transactions of Antennas and Propagation*, vol. 67, no. 1, Jan. 2019, pp. 585–590.

[N] W. Alef, G. Tuccari, S. Dornbusch, M. Wunderlich, M. Pantaleev, **J. Flygare**, F. Tercero, G. Schoonderbeek, J. Hargreaves, R. de Wild, V. Bezrukovs, J. D. Gallego, and J. A. López-Pérez, "BRAND - the next generation receiver for VLBI". in *Proceedings of 14th European VLBI Network Symposium & Users Meeting - PoS (EVN)*, Granada, Spain, Oct. 2018.

[O] **J. Flygare**, B. Billade, M. Dahlgren, M. Pantaleev, J. Dahlström, B. Wästberg, G. Hovey, R. Hellyer,R. Messing, B. Veidt, G. Lacy, and M. Islam, "Beam pattern measurement on offset Gregorian reflector mounted with a wideband room temperature receiver for the Square Kilometre Array". in *Proceedings of the 2018 IEEE International Symposium on Antennas and Propagation & USNC/URSI National Radio Science Meeting (APSURSI)*, Boston, MA, USA, Jul. 2018, pp. 1759–1760.

[P] T. D. Carozzi and **J. Flygare**, "Enhancing SKA Band 1 Polarimetry by Using Two Different Feed Rotations". in *Proceedings of the 2nd URSI Atlantic Radio Science Meeting (AT-RASC)*, Gran Canaria, Spain, Jun. 2018.

[Q] **J. Flygare**, M. Pantaleev, J. Conway, M. Lindqvist, and R. Haas, "Design trade-offs in feed systems for ultra-wideband VLBI observations". in *Proceedings of the 10th General Meeting, International VLBI Service for Geodesy and Astrometry (IVS)*, Longyearbyen, Svalbard/Norway, Jun. 2018, pp. 37-41.

[R] **J. Flygare**, M. Pantaleev, J. Conway, M. Lindqvist, L. Helldner, M. Dahlgren, R. Haas, and P. Forkman, "Ultra-wideband feed systems for the EVN and SKA - evaluated for VGOS". in *Proceedings of the 10th General Meeting,*

International VLBI Service for Geodesy and Astrometry (IVS), Longyearbyen, Svalbard/Norway, Jun. 2018, pp. 42-46.

[S] B. Dong, J. Yang, M. Pantaleev, **J. Flygare**, and B. Billade, "Design of an Asymmetrical Quadruple-ridge Flared Horn Feed: a Solution to Eliminate Polarization Discrepancy in the Offset Reflecting Systems". in *Proceedings of the 12th European Conference on Antennas and Propagation (EuCAP)*, London, UK, Apr. 2018.

[T] S. Weinreb, H. Mani, W. Zhong, **J. Flygare**, B. Billade, A. Akgiray, and L. Dong, "Cryogenic 1.2 to 116 GHz Receiver for Large Arrays". in *Proceedings of the 12th European Conference on Antennas and Propagation (EuCAP)*, London, UK, Apr. 2018.

[U] **J. Flygare**, B. Billade, M. Dahlgren, B. Wästberg, and M. Pantaleev, "Integrated calibration noise coupler for room temperature SKA band 1 feed system". in *Proceedings of the 2017 IEEE International Symposium on Antennas and Propagation & USNC/URSI National Radio Science Meeting (APSURSI)*, San Diego, CA, USA, Jul. 2017, pp. 777-778.

[V] **J. Flygare**, M. Pantaleev, B. Billade, M. Dahlgren, L. Helldner, and R. Haas, "Sensitivity and Antenna Noise Temperature Analysis of the Feed System for the Onsala Twin Telescopes". in *Proceedings of the 23rd Working Meeting of the Euro. Very Long Baseline Interferometry Group for Geodesy and Astrometry (EVGA)*, Göteborg, Sweden, May 2017, pp. 10-14.

[W] M. Pantaleev, L. Helldner, R. Haas, K.-Å. Johansson, L. Petterson, J. Dahlström, M. Dahlgren, U. Kylenfall, B. Billade, and **J. Flygare**, "Design, Implementation and Tests of the Signal Chain for the Twin Telescopes at Onsala Space Observatory". in *Proceedings of the 23rd Working Meeting of the European Very Long Baseline Interferometry Group for Geodesy and Astrometry (EVGA)*, Göteborg, Sweden, May 2017, pp. 15-19.

[X] G. Tuccari, W. Alef, M. Pantaleev, **J. Flygare**, J. A. López Pérez, J. A. López Fernández, G. W. Schoonderbeek, and V. Bezrukovs, "BRAND: A Very Wide-band Receiver for the EVN". in *Proceedings of the 23rd Working Meeting of the European Very Long Baseline Interferometry Group for Geodesy and Astrometry (EVGA)*, Göteborg, Sweden, May 2017, pp. 81-83.

[Y] G. W. Walker, E. Kalinauskaite, D. N. McCarthy, N A. Trappe, A. Murphy, L. Helldner, M. G. Pantaleev, **J. Flygare**, "Optical design and verification of a 4mm receiver for the 20m telescope at Onsala Space Observatory". in *Proceedings SPIE 9914, Millimeter, Submillimeter, and Far-Infrared Detectors and Instrumentation for Astronomy VIII*, 99142V, Jul. 2016.

[Z] J. Yang, **J. Flygare**, M. Pantaleev, and B. Billade, "Development of quadruple-ridge flared horn with spline-defined profile for band B of the Wide Band Single Pixel Feed (WBSPF) advanced instrumentation programme for SKA". in *Proceedings of the 2016 IEEE International Symposium on Antennas and Propagation (APSURSI)*, Fajardo, PR, USA, Jul. 2016, pp. 1345-1346.

[AA] B. Billade, **J. Flygare**, M. Dahlgren, B. Wästberg, and M. Pantaleev, "A wide-band feed system for SKA band 1 covering frequencies from 350 - 1050 MHz". in *Proceedings of the 10th European Conference on Antennas and Propagation (EuCAP)*, Davos, Switzerland, Apr. 2016.

[AB] A. Algaba Brazález, **J. Flygare**, J. Yang, V. Vassilev, M. Baquero-Escudero, and P.-S. Kildal, "Design of F-Band Transition From Microstrip to Ridge Gap Waveguide Including Monte Carlo Assembly Tolerance Analysis". in *IEEE Transactions on Microwave Theory and Techniques*, vol. 64, no. 4, pp. 1245-1254, Apr. 2016.

[AC] V. Belitsky, I. Lapkin, M. Fredrixon, E. Sundin, L. Helldner, L. Pettersson, S.-E. Ferm, M. Pantaleev, B. Billade, P. Bergman, A. O. H. Olofsson, M. S. Lerner, M. Strandberg, M. Whale, A. Pavolotsky, **J. Flygare**, H. Olofsson, and J. Conway, "A new 3 mm band receiver for the Onsala 20 m antenna". in *Astronomy & Astrophysics*, vol. 580, A29, Aug. 2015.

Preface

This thesis is in partial fulfillment for the degree of Doctor of Philosophy at Chalmers University of Technology, Göteborg, Sweden.

The work resulting in this thesis was carried out between December 2016 and March 2022 through the Onsala Space Observatory, Department of Space, Earth and Environment at Chalmers University of Technology, Onsala/Göteborg, Sweden. The following affiliations are all from Chalmers University of Technology, Sweden.

At the completion of this thesis Prof. Jian Yang, was the main supervisor, Prof. Marianna Ivashina was co-supervisor, both from the Antenna Systems Group, Department of Electrical Engineering, and Prof. John E. Conway from Onsala Space Observatory, Department of Space, Earth and Environment was the examiner.

During Dec. 2018 to Jan. 2020, Prof. Marianna Ivashina was the main supervisor, Associate Prof. Rob Maaskant and Dr. Oleg Iupikov were co-supervisors, all at the Antenna Systems Group, Department of Electrical Engineering.

During Dec. 2016 to Dec. 2018 (licentiate), Prof. Rüdiger Haas from the Division of Geoscience and Remote Sensing, Department of Space, Earth and Environment was the main supervisor, Dr. Miroslav Pantaleev from the Onsala Space Observatory (Now at RUAG Space, Switzerland), and Prof. Jian Yang were co-supervisors.

The project leading to this publication has partly received funding from the European Union's Horizon 2020 research and innovation programme under grant agreement No 730562 [RadioNet].

The project leading to this publication has partly received faculty funding from Chalmers University of Technology.

Acknowledgments

Thank you to all the people that have supported me throughout this work.

A special thank you my main supervisor Jian Yang for all the encouragement and support during the years. I would also like to thank Rüdiger Haas for taking on the fleeting job of being my main supervisor during the licentiate. The same goes for Marianna Ivashina having an even shorter go at it during the year after the licentiate degree, and now finishing the job as co-supervisor. The reader may think I'm very difficult to work with, and who knows, but circumstances such as research areas and projects, combined with strong will, have changed over time and I'm forever grateful for the unselfish and adaptive approach that you all have taken to let me succeed. Thank you also to Miroslav Pantaleev, Rob Maaskant, and Oleg Iupikov for supporting me as co-supervisors during these years.

A second thank you to Miroslav for once upon a time trusting me to enter the SKA project, and giving me a great opportunity from the start. On that note, I would like to thank Peter Forkman and Gunnar Elgered who first brought me to Onsala, and Per-Simon Kildal, Astrid Algaba Brazález, together with Jian Yang for once upon a time putting me on the antenna-path.

Thank you to my examiner John Conway for trusting me and keeping me at the observatory all these years. An extra thank you for seeing this PhD to the finish line in many ways. Don't worry John.

Mamma och pappa, jag älskar er och ni finns alltid där och stöttar mig. Without your never-give-up attitude I have inherited, I don't think this would have been possible.

Courtney my love, thank you for being there with all the support. The last few months have not been easy and you have certainly kept me from derailing.

A special thank you to Roger Hammargren for being there the last couple of years and supporting me, even when you didn't need to.

Till de andra killarna på brandstationen, otherwise known as the technical support group at the Onsala Observatory, you guys are the best and weirdest colleagues one could imagine. Special thanks to Leif, Magnus D., and Ulf (SM6GXV) for all the help and advice, to Lars W., Magnus K., and Ronny for making all the crazy structures I have asked for. Thank you to Sven-Erik at GARD for saving this thesis with your fabrication skills.

Thank you also to:

Sander Weinreb for all the wisdom and opportunity, and teaching me the ways of the force, and to the rest of the CalTech/OVRO-team, especially Gregg Hallinan, for the trust and opportunity to come work with you and be part of so many exciting projects during the last few years.

Alex Pollak, Bob Watkins, Walter Alef, and Gino Tuccari for tremendous trust, patience, and effort in our joint collaborations.

Katarina, Paulina, Pia, and Paula for putting up with me and my many questions.

All my family and friends at home and around the world, for being there. I would need a separate thesis to thank you all properly. Special dedication though to Sofia and Tobias, for always being that inspiration and never saying no to a surf session, to Jim for always being there since the beginning, and to Johan for keeping me level in this crazy world.

All the colleagues at Onsala, Antenna group, Yebes, CalTech, Bonn, BRAND-project, DRAO, SKA, NAOC, ATA, LNF, Haystack, SARAO, and elsewhere, you have been crucial during these years. I would also like to thank the Osher Foundation for enabling the research visit to CalTech in 2020, and the Hvitfeldtska foundation, the STINT project, EU RadioNet, the TICRA Foundation, and the ÅForsk foundation for funding conference participation and research visits over the years.

Jonas Flygare
Göteborg, March 2022

Acronyms

ASH: Analytic-Spline-Hybrid

ATA: Allen Telescope Array

BRAND: BRoad-bAND

CNC: Computer numerical control

DSA-110: Deep Synoptic Array 110

DSA-2000: Deep Synoptic Array 2000

EM: Electromagnetic

EVN: European VLBI Network

FoM: Figure-of-merit

GA: Genetic algorithm

HCTF: Hot-cold test facility

HDPE: High-density Polyethylene

HPBW: Half-power beamwidth (3 dB)

LDPE: Low-density Polyethylene

LNA: Low-noise amplifier

MeerKAT: “More" Karoo Array Telescope

ngVLA: Next Generation Very Large Array

OTT: Onsala twin telescope

PO: Physical optics

POM: Polyoxymethylene

PSO: Particle swarm optimization

PTD: Physical theory of diffraction

PTFE: Polytetrafluoroethylene

PE: Polyethylene

QRFH: Quad-ridge flared horn

QRCH: Quad-ridge choke horn

RF: Radio Frequency

RFI: Radio Frequency Interference

Rx: Receiver

SEFD: System equivalent flux density

SETI: Search for extraterrestrial intelligence

SKA: Square Kilometre Array

SNR: Signal-to-noise ratio

Tx: Transmitter

UWB: Ultra-wideband

VGOS: VLBI Global Observing System

VLA: Very Large Array

VLBI: Very Long Baseline Interferometry

Contents

Abstract i

List of Papers iii

Preface ix

Acknowledgement xi

Acronyms xiii

I Overview 1

1 Introduction 3

1.1 Background 3
1.2 State-of-the-art wideband feed technologies 15
1.3 Contribution and challenges 17
1.4 Structure of the thesis 20

2 Reflector Feed Characterization for Radio Astronomy 21

2.1 Reflector geometry 22
2.2 Efficiencies 23

2.3 Sensitivity . . . 26
2.4 System noise temperature . . . 27
2.5 Antenna noise temperature . . . 28
2.6 Intrinsic cross-polarization . . . 32

3 Numerical Ultra-wideband Feed Design and the Quad-ridge Flared Horn Technology 35
3.1 Ridge waveguide . . . 35
3.2 The Quad-ridge Flared Horn . . . 36
Single-ended excitation . . . 38
Profile shape . . . 41
Analytic-spline-hybrid profile . . . 43
3.3 Design optimization . . . 45
3.4 System simulator . . . 47
Design for high sensitivity . . . 49
3.5 Manufacture and tolerances . . . 53
3.6 Feed measurements . . . 58
3.7 Receiver noise temperature . . . 61
3.8 Low-frequency room temperature system . . . 62

4 Dielectric loading of the Quad-ridge Flared Horn 65
4.1 QRFH with dielectric load . . . 65
Dielectric load - compact footprint . . . 67
4.2 Wide beamwidth for deep reflectors . . . 70
Design for ”Small-D-Big-N“ . . . 72
Dielectric load - decade bandwidth and beyond . . . 73
Dielectrically loaded QRFH compared with log-periodic feed . . . 75
4.3 Wideband dielectric material data . . . 77

5 Contributions and Future Work 81
Future work . . . 82
5.1 Paper A . . . 84
5.2 Paper B . . . 84
5.3 Paper C . . . 85
5.4 Paper D . . . 85
5.5 Paper E . . . 86

References **89**

II Papers 101

A BRAND: Ultra-wideband feed development for the European VLBI network - A dielectrically loaded decade bandwidth quad-ridge flared horn **A1**

1 Introduction A3
2 Specifications for BRAND A4
3 Quad-Ridge Flared Horn A5
3.1 Model for Optimization A6
3.2 Optimization - Stochastic Algorithms A6
4 Feed Performance A7
5 Two-Step Optimization - Analytic-Spline-Hybrid (ASH) A12
6 Conclusions A13
References A14

B Dielectrically Loaded Quad-Ridge Flared Horn for Beamwidth Control Over Decade Bandwidth - Optimization, Manufacture, and Measurement **B1**

1 Introduction B4
2 Feed Design B5
2.1 Quad-Ridge Flared Horn B5
2.2 Dielectric Load B6
2.3 Optimization B7
3 Mechanical design and manufacture B8
3.1 Excitation - Orthogonal Single-Ended Launch-pins . . . B10
4 Simulated and Measured Performance B12
4.1 Beam patterns B12
4.2 Aperture- and sub-efficiencies B15
4.3 Sensitivity - System Equivalent Flux Density (SEFD) . B16
4.4 Intrinsic Cross-polarization Ratio (IXR) B18
5 S-parameters with Tolerance Analysis B19
5.1 Tolerance Parameters B19
5.2 Tolerance Analysis B20
5.3 Tolerances for Production B22

6 Conclusion B23
References B24

C Strategy and Overview for Development of Beyond-Decade-Bandwidth Quad-ridge Flared Horns for Radio Astronomy C1
1 Introduction C3
2 Reflector Feed Sub-efficiencies C5
3 Dielectrically Loaded QRFH C5
4 Design Goal Considerations C7
5 Conclusion C8
References C9

D Beyond-decade Ultra-wideband Quad-ridge Flared Horn with Dielectric Load for Beamwidth Stability over 1-20 GHz D1
1 Introduction D4
2 Electromagnetic Model D6
2.1 Horn Profile D6
2.2 Ridge Profile and Backshort D8
2.3 Dielectric Profile D11
2.4 Optimization D14
3 Mechanical Design D16
3.1 Aluminum alloy D16
3.2 Thermal Analysis D16
3.3 Ohmic Loss D18
3.4 Manufacture - Quarters D20
3.5 Excitation - press-fit termination in blind-hole D22
3.6 Dielectric Load D23
4 Electromagnetic Performance D27
4.1 S-parameters D27
4.2 Aperture efficiency and cross-polarization D28
4.3 Unshaped and shaped reflector D28
5 Feed pattern measurement - Anechoic chamber D32
5.1 Tolerance - Ridge Skew Port 2 . . . . . D36
5.2 Feed loss D38
6 Tests on Allen Telescope Array D39
7 Conclusion D42
References D44

E Quad-ridge Choke Horn with Dielectric Load as a Wideband Feed for Non-cryogenic Reflector Arrays in Radio Astronomy E1
1 Introduction . . . E3
2 Quad-ridge Choke Horn Model . . . E6
3 Electromagnetic Modeling . . . E9
3.1 Optimization . . . E11
3.2 Aperture Efficiency . . . E12
3.3 S-parameters . . . E13
4 Mechanical Design . . . E14
4.1 Dielectric Lid . . . E15
4.2 Connector and Launch-pin . . . E16
4.3 Ridge Contact - Press-fit Receptacle . . . E17
4.4 Feed Patterns . . . E18
4.5 Cross-polarization . . . E20
5 On-dish Performance: Spillover Shield . . . E21
6 Conclusion . . . E24
References . . . E24

Part I

Overview

CHAPTER 1

Introduction

This chapter briefly describes the main application areas (radio astronomy and related space geodesy observations) to which the antenna research described in this thesis is directed. An overview of design challenges in ultra-wideband reflector feeds, with overwhelming focus on the quad-ridge flared horn, is presented together with a summary of other state-of-the-art feed technologies. Finally, contributions of this work and proposed solutions to the challenges presented are summarized.

1.1 Background

In 1928, Bell Laboratories in Holmdel, New Jersey wanted to study transatlantic radio frequency interference (RFI) for short-wave communications. The newly graduated engineer Karl G. Jansky, with a degree in physics, was hired to do the job. Jansky designed an antenna for 20.5 MHz (λ=14.6 m) mounted on a large rotational platform that used tires from a model T-ford to turn 360 degrees. Jansky studied the radio waves in all directions for quite some time and found that the most common noise the antenna picked up was the electromagnetic waves generated from accelerating charges in thunderstorms [1].

But he also found a weaker signal that came about and disappeared once a day. Curious about its origin he continued to study it for several months. A qualified guess was that the signal came from the Sun, however the time period was slightly less than 24 hours. Could it be from something outside our solar system? The conclusion was that the signal came from the center of our Milky Way galaxy where the star constellation Sagittarius is located. Jansky had, unintentionally, performed one of the first ever radio astronomical observations and these results were published in 1932. Jansky was very keen on continuing his work within this newly discovered field, however Bell Laboratories had other plans for him. Sadly he was moved to other assignments within the company, and died at the age of 44. The field of radio astronomy did however live on and today, and the projects around the world involving radio telescopes no doubt reaches far beyond the wildest imagination of Jansky. To honor Jansky, the flux density strength of observed radio sources has been

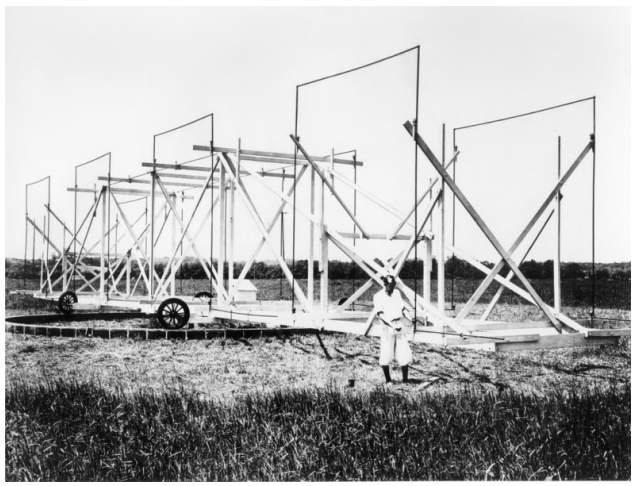

Figure 1.1: Jansky in ca 1930 with his giant 20.5 MHz radio receiver, unintentionally the world's first radio telescope. Image credit: NRAO/AUI under CC-BY-3.0.

given the unit with his name, also shortened as Jy. Radio sources in space vary vastly in strength where a flux density above 1 Jy $=10^{-26}$ W m^{-2} Hz^{-1} would be considered relatively strong but also quite uncommon. For comparison, a cell-phone's flux density measured from a distance of 1 km at 1.8 GHz

corresponds to roughly $1.1 \cdot 10^8$ Jy. Many astronomical sources of interest to today's astronomers are much weaker than 1 Jy and as low as micro-Jy (μJy, 10^{-6}). The *sensitivity* figure-of-merit (FoM) of radio receivers needed to detect these sources is commonly given in the same unit and called system equivalent flux density (SEFD). The signal-to-noise ratio (SNR) from observing a source with known flux density S_ν has the following dependence on the receiving SEFD

$$\mathrm{SNR} = \frac{S_\nu}{\mathrm{SEFD}}\sqrt{t\Delta\nu},$$

where t is the integration time and $\Delta\nu$ is the available frequency bandwidth [2]. Simply put, to improve the SNR we can (i) improve sensitivity, (ii) increase bandwidth, or (iii) increase observation time, where the last point is undesired for several reasons. The SEFD is inversely proportional to the telescope's " G/T " or more commonly expressed as the noise temperature over effective aperture area, i.e. SEFD $\propto \frac{T}{A}$. To improve sensitivity by decreasing SEFD, we can therefore either increase the area i.e. make a larger telescope with better optimized feed illumination, or reduce the system noise temperature i.e. minimize feed and LNA loss, as well as reduce spill-over pick-up from the ground.

Large ground-based radio telescopes (Fig. 1.2) operating in the radio-window (Fig. 1.4) are most commonly in the form of a large mechanically steerable reflector with single-pixel feed receiver(s) (single feed with single beam) [1]. The reflector collects incoming energy and focuses it in the single point where the feed and adjacent receiver system are located. Another option is to instead of the single-pixel system to use a phased array feed (PAF) or focal-plane array for more custom beam properties (e.g. pattern shape, multi-beam) [3]. There are other telescope concepts to maximize collecting area such as synthesized aperture arrays for low frequencies [4] or fixed giant reflectors that can steer the beam within a limited angle by suspended movable receiving systems [5], [6]. Synthesized large apertures can be formed by telescopes through interferometry both over short and long distances with increased sensitivity and observational resolution compared to each telescope on its own.

The possibility of reducing noise in the receiver has been greatly advanced the last few decades. Today, the internal noise contribution of front-end components, including the first stage LNA's internal noise, is on the same level or better than the sky brightness even for the centimeter and sub-centimeter wavelengths, see Fig. 1.3. The LNA technology has matured immensely and

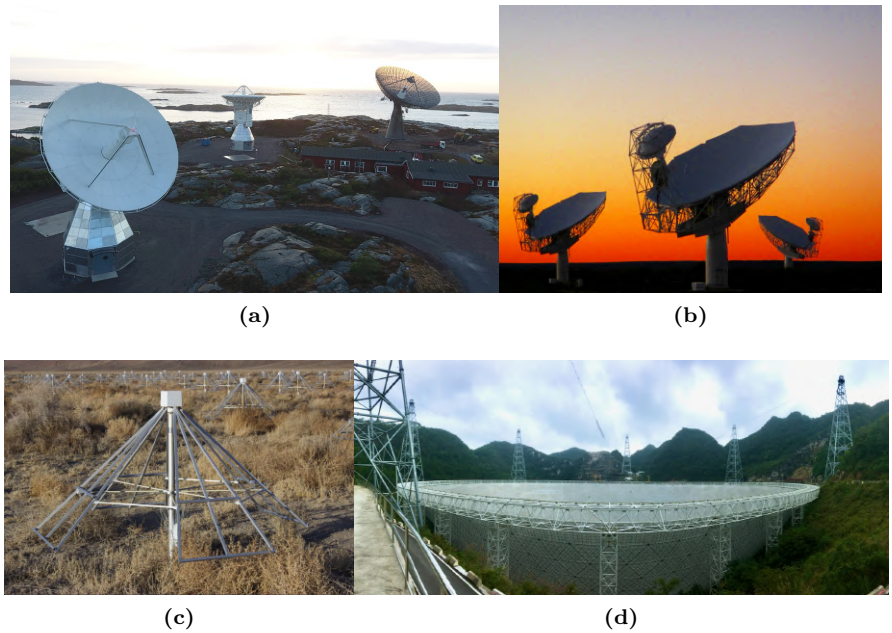

Figure 1.2: (a) Onsala Twin Telescope's two 13 m reflectors shown on the left, and the 25 m telescope on the right, located in Onsala, Sweden. Image credit: Roger Hammargren, OSO; (b) Three of the 64 offset Gregorian reflectors in the MeerKAT array, each 13.5 m in diameter, located in the Karoo desert, South Africa. Image credit: Leif Helldner, OSO; (c) The Owens Valley Long Wavelength Array (OVRO-LWA) consists of 288 crossed dipoles, located in Owens Valley, CA, USA; (d) Five-hundred-meter Aperture Spherical Telescope (FAST) located in Guizhou province, China.

can deliver very low noise-performance even over wide bandwidths [9]–[11]. The development is not limited to the cryogenic regime, but includes room-temperature advancements as well [12], [13].

To reap the rewards of the large physical area of a reflector telescope, while minimizing the spill-over noise picked up from ground and achieving a good match to the LNA inputs - a good low-loss *feed* is needed before the rest of

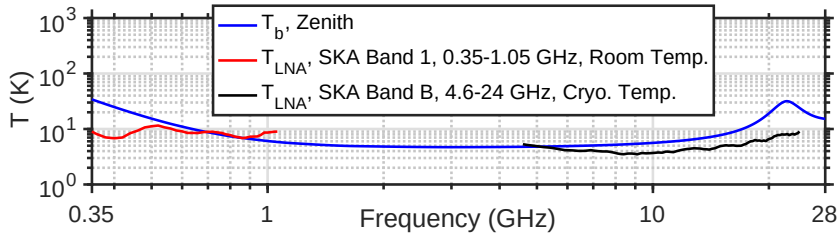

Figure 1.3: Sky brightness from sub-meter to sub-centimeter overlayed with noise of two wideband LNAs optimized for room temperature [7] and cryogenic temperature [8] operation.

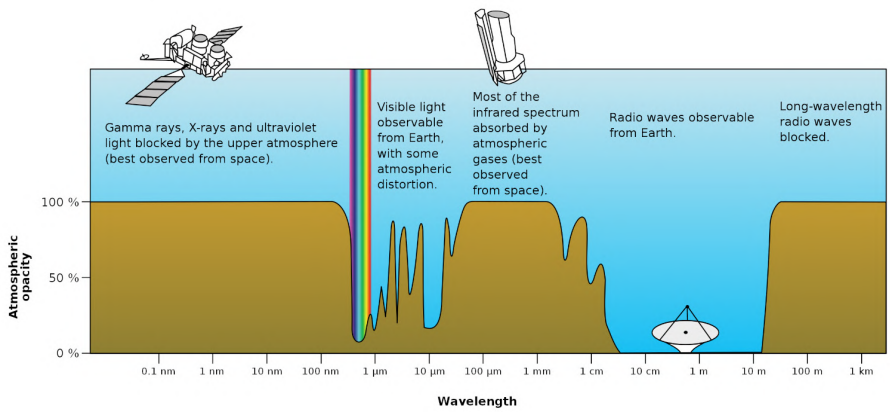

Figure 1.4: The electromagnetic frequency spectrum, with the ground-observable radio window seen to the right. Image credit: NASA(Original)/Mysid.

the receiver chain. If all these aspects are accounted for, the receiver system is very likely to enable high-sensitivity observations. Properly designed octave feeds (typically conical, axial-corrugated horns) will yield a very good feed pattern-symmetry and cross-polarization, which results in low spill-over and high aperture efficiency, even in unshaped reflectors [14]. The choice of octave or instead a wideband system is dictated by the application and science goals as well as the cost and system constraints. Each of these categories can be divided further into multiple sub-categories where the benefits and trade-offs must be assessed.

The advantages of using a good wideband feed system in the sense of large bandwidth ratio are several in the meter to sub-centimeter wavelengths. On that note, this thesis treads lightly around mm-wave astronomy where very different design techniques, receiver systems and environmental circumstances apply. For millimeter wavelengths octave feed design in the form of corrugated horns and quasi-optics together with Cassegrain reflector system is the common choice. The long effective focus of such dishes is more forgiving in phase misalignment relative to the "focal point", which could be even more challenging to design otherwise at these wavelengths. The fact that the ~ 1 GHz absolute bandwidth available from an octave feed starting at 1 GHz, is 100 times larger for a feed starting at 100 GHz, makes the distinction between "wideband and wideband" quite important as well. Therefore, within the context of this work wideband refers to bandwidth ratio $> 2{:}1$, i.e. the highest frequency of operation is more than 2 times that of the lowest. The wideband feed applications concerned in this thesis range from UHF-band, or perhaps lower depending on the reflector size, well up to $\sim$50 GHz. Some practical and scientific reasons for wideband feed and receiver systems include but are not limited to:

1. **The cost**: In reflector arrays, the cost savings of developing, building, and maintaining only one wideband system compared to multiple octave receivers can be enormous. For a 100-m single-dish telescope, the cost of covering two octaves with two separate receivers is most likely negligible compared to the cost of the reflector itself. However, for an array of 10-m dishes to cover (almost) equivalent collecting we would need 100 reflectors. Reasonably assuming the price for an octave system and a wideband system is similar, the cost reduction is obvious.

2. **Physical space**: What can be useful for large single-dish telescopes, is the reduction of allocated space needed for equipment in the receiver cabin, specifically in the sub-meter to centimeter range, where a wideband system covering e.g. 1-16 GHz would save a lot of space compared to four octave systems.

3. **"Small-D-Big-N"**: In combination with the development of room temperature LNA technology [7], [13], and smart data processing, compact wideband feeds enable the concept of large arrays with small-diameter, low-cost reflectors as a different type of radio instrument. For such

"Small-D-Big-N" arrays the low cost per covered bandwidth and physical space advantages (point 1 and 2 above) of a wideband system are essential to realize the concept. This type of array allows for low to mid-range budget proposals to surpass the very expensive large-reflector arrays in both survey speed and sensitivity over the same frequency range (Fig. 1.7).

4. **Large instantaneous available bandwidth**: In a single-pixel-fed reflector telescope, only one receiver package at a time can be used (excl. some Nasmyth-Cassegrain, and tertiary mirror concepts). For simultaneous access to the entire bandwidth while observing, and improved continuum measurement sensitivity (2.9), a wideband system can be used. There are several *scientific motivations* for the use of wideband receivers:
    - *Spectral line searches* - while normally high sensitivity is required for observations, the search for strong red shifts over multiple frequencies at the same time is attractive.
    - *Search for extraterrestrial intelligence (SETI)* - where the benefit of monitoring as many frequencies as possible is quite obvious.
    - *Pulsar searches and timing* - which can occur over multi-decade bandwidth [15]. An extremely interesting application of pulsar timing is the detection of low-frequency gravitational waves.
    - *Fast radio burst (FRB)* - which at the time may be one of the most popular science goals in meter and centimeter observations. The FRB transient spectrum is short-lived on the order of milliseconds and may only happen once from its direction, so large field-of-view, wide bandwidth, and high sensitivity are required for localization.
    - *Astrometric and Geodetic VLBI* - By separating telescopes with very large distances, the technique of Very-Long Baseline Interferometry (VLBI) can yield extreme angular resolution in observations, proportional to the longest baseline separation of the telescopes [2]. It can also be used to study Earth by observing known sources as references that are stable in its position relative to us. With several of these telescopes spread across the globe, and looking at the same source, we can very accurately determine the separation between them due to the geometric delay in the signal. This

is done by high-precision timing of when the signal is received at each telescope, using atomic clocks. In fact, this geodetic VLBI technique is the only space-based technique that can determine all five Earth orientation parameters (EOP), and give us a direct connection between the space-based and the earth-fixed reference frame [16]. This gives knowledge about the irregularities in the rotation of Earth, universal time, and the direction of the earth rotation vector. The main observable of geodetic/astrometric delay is the group delay which is the phase gradient over frequency. A large instantaneous frequency range gives a more accurate group delay. Very wide observing bandwidths also allow such observations to remove the corrupting effect of the ionosphere because of their unique signature over a wide frequency range.

- *Polarization observations of Faraday rotation* - The effect of rotation on the polarization vectors as they travel through magneto-ionized media, occurs over large bandwidths [17]

Below we exemplify a few current and future projects that use or will use wideband feed and receiver systems. The next generation of space-geodetic VLBI is realized through the VLBI Global Observing System (VGOS), where each telescope requires a very wide simultaneous bandwidth [18],[19]. The idea is to have a rather standardized observation system of telescopes with reflector diameters in the range of 12-13 m and located at VLBI stations around the world, to continuously observe and provide geodynamical data – 24 hours a day. The data from VGOS will improve the global navigation satellite systems (GNSS) predicted location precision to be in the order of 1 mm which is crucial for our society's growing demand in electronic localization. One of the most recently inaugurated VGOS stations is the Onsala Twin Telescope (OTT), consisting of two identical reflectors, see Fig. 1.2a, that can achieve continuous observation of sources. The continuous coverage is achieved by moving the non-observing telescope to a new source while the other is actively observing [20]. The receiver system of VGOS is based on dual-polarized wideband feed architecture to observe sources over many different wavelengths simultaneously. Requirements of low-noise as well as noise and phase calibration are also crucial.

One of the strongest drivers for wideband feed development the last few decades is the move in astronomy towards interferometric arrays with reflector

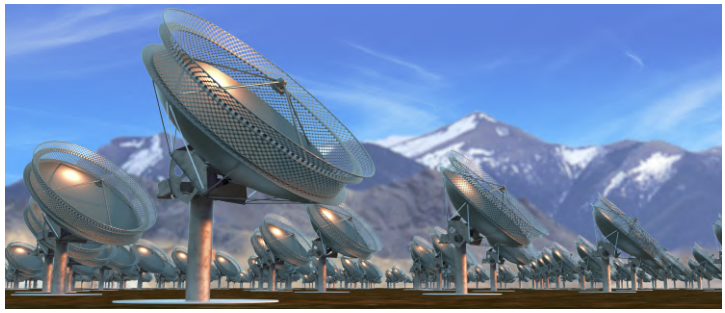

Figure 1.5: DSA-2000 array concept: 2000 × 5 m axially-symmetric prime-focus reflectors, each equipped with a room temperature wideband feed package covering 0.7-2 GHz, and a spill-over shield. Image credit: C. Carter/DSA

geometries of medium to low f/D (reflector focal length over diameter). Below follows a short intro to some of these projects

- The *Deep Synoptic Array 2000 (DSA-2000)* is aiming to be a world-leading radio survey telescope utilizing the *"Small-D-Big-N"* approach for huge survey speed and continuum sensitivity (Fig. 1.7). It will consist of 2000 reflectors each with a 5 m diameter (Fig. 1.5), and equipped with a ground-breaking room temperature receiver package covering the wideband frequency range 0.7–2 GHz with an exceptional system noise temperature predicted to be 25 K [13], [21]. The proposed feed design is equipped with a low-loss dielectric lid on a choke-type quad-ridge structure to achieve a symmetric broad feed pattern over a wideband frequency range, further described in Paper E. Due to the consistent broad feed pattern and excellent receiver noise, the stand-alone feed package presents another application: the Galactic Radio Explorer (GReX), an all-sky monitor to find the brightest bursts in the radio sky [22].

- The *Square Kilometre Array (SKA)* is an international project well underway to build the world's largest radio telescope with highest sensitivity in its frequency range [23]. In the final form it will enable science with unprecedented sensitivity and survey speed. The SKA-MID will consist of nearly 200 offset Gregorian reflector telescopes, where 64 of them constitutes the MeerKAT ("More" Karoo Array Telescope) [24]. The SKA

reflectors will be 15 m diameter dishes with a spill-over shield on the sub-reflector rim. In total it will constitute a 150-km diameter array in the Karoo desert in South Africa. Each antenna will be equipped with multiple feed packages spanning 350 MHz to 15.4 GHz with a potential of even higher frequency coverage [25]. The lowest frequency band of the SKA-MID, *Band 1* covers 350–1050 MHz with a completely room (ambient) temperature wideband feed package (including the LNAs) with high sensitivity [7], [26]. As a potential upgrade under the advanced instrumentation programme - wideband single-pixel feed (WBSPF) of the SKA, a 2-feed dewar is proposed to cover the upper bands of the SKA and further over 1.6-24 GHz. The proposed Band B covers 4.6-24 GHz with a single feed package [8], [27].

- *The Allen Telescope Array (ATA)* where the existing single-pixel feed receivers currently cover more than a decade in bandwidth divided in four sub-bands, and dedicated to constantly monitoring a large frequency range in search for extraterrestrial intelligence (SETI) [28]. The 42 hydroformed ATA reflectors at the Hat Creek Observatory in California, USA have an offset Gregorian configuration with a shroud shielding the feed from spill-over noise pick-up from the ground, see Fig. 1.6. Currently the frequency range covers 0.9-14 GHz with a log-periodic antenna with different phase centers for the sub-bands requiring re-focusing. A new ultra-wideband QRFH upgrade covering 1-20 GHz in one single feed was tested in 2022, and is further described in Paper D.

Figure 1.6: Reflector in the Allen Telescope Array (ATA) with shroud shielding against ground. Image credit: Alex Pollak, ATA/SETI.

- The future successor to the iconic Jansky Very Large Array ((J)VLA), is simply called the *next generation Very Large Array (ngVLA)* and is planned to deploy 244 × 18 m and 19 × 6 m reflectors in Southwestern United States, and northern Mexico each of which will cover 1.2-116 GHz with six cryogenic feed packages where the two lowest frequency bands will use wideband feed technology [29]–[31].

As briefly mentioned before, most radio sources are very weak, so to be able to study these sources with a realistic integration time we need to increase the sensitivity. A major reason to use large arrays of reflectors instead of one giant dish to increase reflector area for sensitivity is to maintain a reasonable size and cost per reflector. A somewhat "hand-waving" estimate of reflector production cost is proportional to $\sim D^3$, where D is the diameter. Array sensitivity increases proportionally with the number of telescopes, N (for large N) but also with the frequency bandwidth (continuum) available in the receivers. Another reason for using arrays is the large and small baseline spread, enabling for UV-plane coverage within the array itself. This further emphasises the need for wideband systems in reflector arrays. Wideband systems

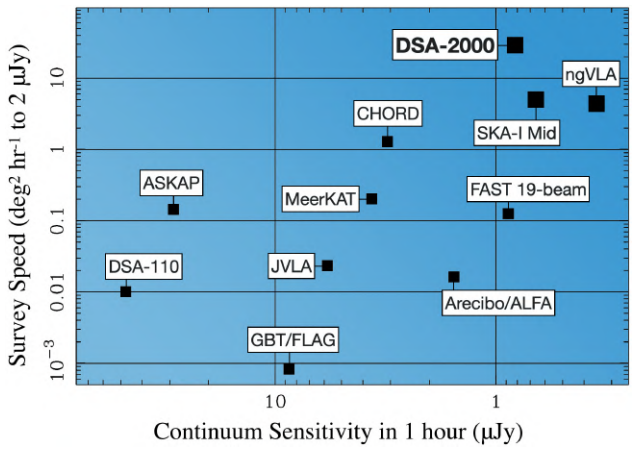

Figure 1.7: Survey speed vs continuum sensitivity of the DSA-2000 and other current (small squares) and planned (large squares) radio telescopes that operate at 1.4 GHz. Image credit: DSA/CalTech.

provide potential upgrades for existing interferometric telescopes as well such as the European VLBI Network (EVN). The RadioNet sponsored EU Horizon 2020 project BRoad-bAND (BRAND) is an international joint research activity that aims to cover L-,S-,C-,X-, and Ku-band with one single receiver [32]. The BRAND-goal is to offer a complete astronomy receiver package for applicable telescopes, and be compatible with the VGOS frequency range 2–14 GHz. The work in this thesis has led to the dielectrically loaded QRFH feed covering 1.5–15.5 GHz for the BRAND project, further described in Papers A-C. The first prototype is designed for the deep primary focus position of the 100 m reflector in Effelsberg (Fig. 1.8)

Figure 1.8: Effelsberg 100 m reflector (MPIfRA) in Bad Münstereifel, Germany.

As briefly alluded to, there is no free lunch not even in broadband frequency ranges. For a wideband feed, consistent reflector illumination over frequency is a challenge to achieve. The feed pattern evolution over frequency is much more fickle in a wideband feed than for octave counterparts. Unlike the corrugated or conical octave horns, none of the established ultra-wideband feed technologies are BOR antennas (Body-of-revolution), meaning none of them are circular symmetric in structure [33]. Most of them possess some type of rotational symmetry around the boresight or propagation direction. This means that mitigating the power lost to high order azimuth modes is important for a consistent gain and feed pattern evolution across the frequency band [34]. Generally the impedance match is challenging to achieve for very wide band-

widths as well. It must therefore be taken into account in parallel during the design to reduce the effect on system noise from mismatch between feed and LNA in a receiver. This requires an understanding of how feed performance changes over the entire frequency band so designing for λ-performance is not possible. Most wideband feeds are therefore not analytically defined in the sense of specific design-equations being readily available for the desired frequency range and performance. Rather the design is done numerically through global and local optimization of the feed model and it is evaluated based on the intended reflector geometry.

1.2 State-of-the-art wideband feed technologies

There are a multitude of ultra-wideband feed concepts that have been proposed and developed during the last two decades. Below we briefly introduce some of them used for reflector telescopes in radio astronomy and space-geodesy applications today:

- The *ATA feed (or Antonio Feed)* developed for the Allen Telescope Array [28]. This is a log-periodic frequency independent structure, with linear dual-polarization in a pyramidal form. The feed achieves good feed pattern symmetry over decade bandwidth and beyond, but suffers from a large footprint, and strong phase variation over the band. This requires re-focusing for different sub-bands, limiting the instantaneous bandwidth available.

- The *Eleven-Feed* developed at Chalmers University of Technology is a more compact log-periodic feed (to the right in Fig. 1.9), with linear dual-polarization [35], [36]. The feed has good feed pattern symmetry, impedance match over 5:1 to 10:1 bandwidth, and the phase center variation is small. The main drawback of the Eleven-Feed is the difficulty to adapt to vastly different f/D, and the complex feeding network to satisfy the differential input.

- The *Quasi-Self-Complementary Feed (QSC)* developed at Cornell [37]. Another compact log-periodic structure with linear dual-polarization. The pattern symmetry is good over decade bandwidth, and it achieves very good input match. Again the feed requires a differential input, and has a delicate structure to manufacture.

- The *Dyson Quad-Spiral Array* developed at Carlos III University of Madrid is a dual-circularly polarized feed with interesting wideband performance [38]. The structure is based on Dyson conical log-spirals in an array configuration, with a self-complementary structure that yields a semi-real impedance. The structure is difficult to manufacture and assemble properly for higher frequencies due to the tolerances required.
- The *Quad-ridge Flared Horn (QRFH)* predominantly developed at California Institute of Technology [39], [40]. The QRFH has been further deeply explored in differential configuration with modal-based design in [41], [42]. The all-metal QRFH (to the left in Fig. 1.9) is a low-loss linear dual-polarized feed with near-constant phase center and good E-plane beamwidth over large bandwidths. It is a flared-out waveguide structure and can therefore, like corrugated horns, be adapted to a range of f/D. The single-ended version is easily designed for a coaxial 50-Ω interface resulting in the need for only two single-ended LNAs. The QRFH suffers from poor beamwidth stability particularly over frequency, with under-illumination of the reflector and poor cross-polarization as a result in the upper part of the frequency range.

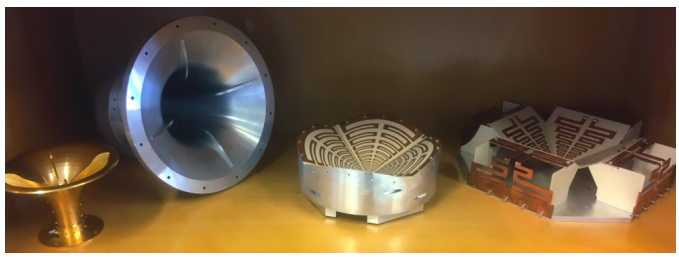

Figure 1.9: Ultra-wideband feeds: two QRFHs (left) and two log-periodic Eleven-Feeds (right), designed for different frequencies and reflectors.

A majority of the concepts presented in the list above are based on log-periodic geometries with differential inputs which complicates the structure and increases cost of the overall system. The QRFH is the only feed of the aforementioned that can easily be designed in single-ended configuration. Typically with a 50-Ω coaxial interface, the QRFH can achieve nominal input

reflection coefficient less than −10 dB for >6:1 bandwidth [39]. Due to the ridge structure, it achieves dual-linear polarization over large bandwidth in a compact form. For large arrays with multiple receivers the cost reduction of only needing two LNAs per feed with no external balun is a great advantage. The waveguide properties give the QRFH a sharp low-frequency cut-off which mitigates the impact of low-frequency RFI. The overall shape and structure is straightforward to manufacture with known machining techniques without complex or expensive methods for assembly. Because of the compact and simple design, it is a preferred choice by technical staff. However, as the radio community wants to push the observational bandwidths above a decade in frequency, there is a need to push the QRFH operational bandwidth and mitigate its drawbacks while maintaining most of the benefits. In the following section we list the challenges facing QRFH design and briefly how that has been addressed in this work.

1.3 Contribution and challenges

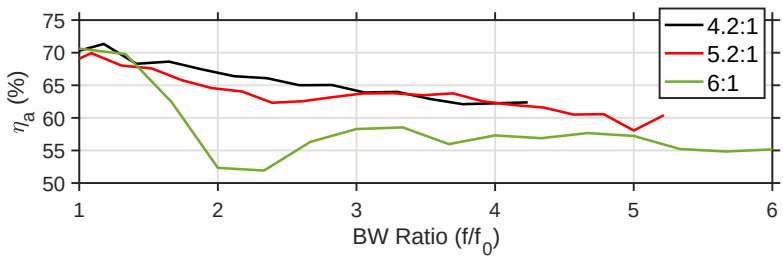

Figure 1.10: Aperture efficiency over normalized bandwidth in an unshaped reflector for three different all-metal QRFH bandwidth ratios.

The biggest drawback of the QRFH feed is the narrowing beamwidth in the upper part of the frequency band especially in the H-plane, the principal plane orthogonal to the polarization (i.e. linear). This occurs as the feed pattern evolves over the design frequency band due to the mode-constellation drastically changing from the fundamental-mode dominated form at the frequency cut-off. The most obvious result of this is under-illumination of the reflector, and a decreasing aperture efficiency over the design band, exemplified

in Fig. 1.10. From the figure it is also visible that increasing the bandwidth ratio reduces the overall efficiency average in the all-metal QRFH. The under-illumination is even more significant in wideband design for applications with deep reflectors (requiring wider feed beamwidth). From the work in this thesis, the following challenges that are related to this topic have been addressed:

Common design challenges identified for ultra-wideband quad-ridge flared horn that are addressed in this work.

I	✓	*Beamwidth stability, as the QRFH pattern typically narrows with frequency. Especially challenging for ≥ 6:1 bandwidths and/or wide beamwidths (deep reflectors with half-subtended angles > 70°)*
II	✓	*Feed pattern cross-polarization, correlated with **I**. Property translates to IXR on dish.*
III	✓	*Improve the QRFH performance without altering its practical, single-ended, and straightforward design, while also keeping its compact footprint for installation in dewar.*

An approach to improve the feed pattern symmetry, is the differential or quadraxial excitation of the QRFH [42], [43]. By using a symmetric differential excitation point, the only asymmetry of the QRFH in single-ended configuration, the coaxial interface, is then removed. This technique mitigates higher-order mode excitation at the launch-point which results in a more symmetric feed pattern over frequency. By using a more advanced throat structure of the QRFH further suppression of higher-order modes could be implemented over very large bandwidths and realized with the emerging technologies of selective laser melting (SLM), 3D-printing, or metal additive manufacturing [44].

The approach taken *in this thesis* to improve beamwidth and cross-polarization over frequency, is dielectric loading of the QRFH. This has previously been investigated in different forms to assess the pattern symmetry even in conical horn structures [45]. With a large dielectric lens covering the QRFH aperture, improved efficiency for high-gain applications over 10:1 bandwidth has been indicated [46]. A dielectric lens has also been used with success for 3:1 bandwidth [47]. A highly sophisticated incorporation of a large smooth-shaped multilayer dielectric spear in a differentially fed QRFH, together with

a choke-skirt, was presented in [48] with extremely symmetric feed pattern as a result over 6:1 bandwidth. The structure is however complex, with a dielectric footprint that can be cumbersome in cryogenic dewars [49]. In Fig. 1.11 the concept of dielectrically loading the QRFH is exemplified with the >10:1 BRAND-feed covering 1.5-15.5 GHz with stable H-plane beamwidth. This feed is further described in Paper A-C.

The main contribution of this thesis is the proposed use of a simple homogeneous and low-loss dielectric load, with little effect on the overall physical footprint, added to the metallic quad-ridge structure to improve feed pattern beamwidth over very large bandwidth.

In conjunction with this we also present and explore:

- Analytic-spline-hybrid (ASH) concept of defining the QRFH profiles.
- 3D-spline ridge structure for low-frequency cross-pol reduction and improved matching.
- The Quad-ridge Choke Horn (QRCH) for wideband and wide beam application in non-cryogenic reflector arrays.
- Simplified press-fit launch-pin termination.

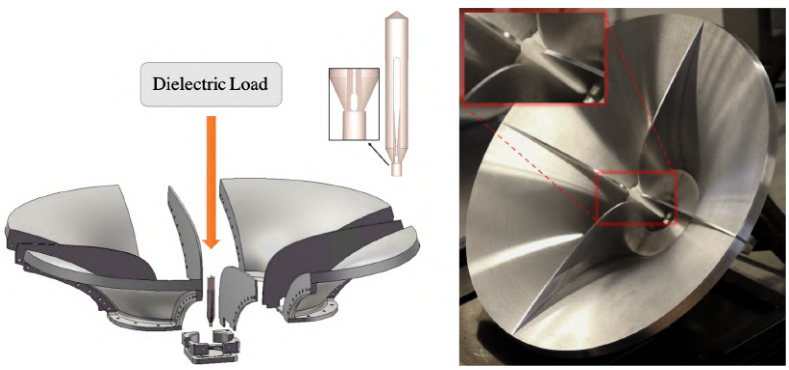

Figure 1.11: Dielectric load/insert in the quad-ridge flared horn for better beamwidth stability and control over decade bandwidth and beyond. The insert has little effect on the overall footprint.

Design, analysis, manufacture, and measurement of the QRFH are approached throughout this work with the mindset of practical implementation in real-world applications. This is something the author feels strongly about as the field falls in-between research and product realization. This work has been developed as part of three larger projects, resulting in three feed prototypes:

1. The BRoad-bAND (BRAND) QRFH feed design covering 1.5-15.5 GHz (10.3:1 bandwidth) for the Effelsberg 100-m reflector's prime-focus [Paper A-C].

2. The beyond-decade-bandwidth QRFH feed design covering 1-20 GHz (20:1 bandwidth), with a first prototype installed and tested on the Allen Telescope Array 6 m offset Gregorian geometry [Paper D].

3. The Quad-ridge Choke Horn (QRCH) feed design covering 0.7-2 GHz (2.85:1 bandwidth) in the deep 5 m prime-focus reflector proposed for DSA-2000 and as a stand-alone antenna for GReX [Paper E].

1.4 Structure of the thesis

The thesis chapters 1–5 introduce the field together with the work presented in the appended papers. Chapter 1 is a short overview of radio astronomy and space-geodesy together with the field of radio telescopes and feed design. In Chapter 2 the most relevant analysis framework used in this work to evaluate feed design for a reflector system is introduced: an overview of aperture efficiency, antenna noise temperature, and sensitivity calculation is given. In Chapter 3 the QRFH concept for UWB design is introduced and continues with the expansion into Chapter 4 of dielectrically loaded QRFHs for better beamwidth control which is the main focus of the appended papers. Finally, Chapter 5 gives a brief summary of the included papers and the future investigations and possibilities that could be derived off of this work.

CHAPTER 2

Reflector Feed Characterization for Radio Astronomy

The characterization and evaluation of a reflector feed design is strongly dependent on the intended application and dish optics. In this work, the evaluation of feed design is therefore predominantly made in that context. As discussed in the introduction, the receiving sensitivity is most commonly the fundamental figure-of-merit for a reflector-feed-receiver system. The aperture efficiency and system noise temperature are therefore important characteristics. However, properties such as polarization purity, field-of-view, and sidelobe levels that are directly dependent on the feed-to-reflector constellation can also be as important depending on the application. In this chapter a brief overview of the most important characteristics for the example designs in this thesis are given. The calculations are given for reflector telescopes equipped with single-pixel feed receivers. The theory given here, general electromagnetic, and antenna concepts are taken mostly from: [1], [2], [50]–[53]. The nomenclature and syntax in the thesis can deviate from these references. The antenna applications presented herein are in receiver configuration, however in the discussion the terminology sometimes describe the antennas as if they were in transmit-mode. This is a common approach due to reciprocity, and makes spill-over and illumination from feed horns more intuitive to understand.

2.1 Reflector geometry

Feed design for reflector-type radio telescopes is strongly dependent on the intended reflector geometry. Parameters such as reflector size, focal length, blockage, and possible sub-reflector configurations are all key parameters influencing the design approach, choice of feed type and achievable performance. Typically, dual-polarization is required for most applications, and so must apply to the feed output as well. The majority of reflector telescopes, symmetric and offset, move in rotation around azimuth scanning parallel to the horizon, therefore defining the direction of horizontal polarization. The vertical polarization is defined as the elevation position scanning orthogonal to the horizon. Depending on the reflector shaping and geometry, special types of feed design can be used to compensate for offset structures over very wideband frequency ranges [54]. The dual-polarization sampled by the telescope does not have to be in vertical/horizontal configuration, but could instead be rotated 45 degrees to sometimes enhance polarimetric response in offset reflector geometry [55]. In Fig. 2.1 the simplest form of a reflector - the unshaped and

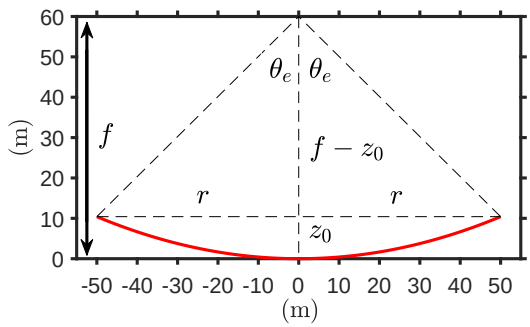

Figure 2.1: Schematics of an unshaped prime-focus axially-symmetric paraboloidal reflector, θ_e is the half-subtended angle from the focal point.

unshielded, prime-focus and axially-symmetric paraboloidal reflector (more commonly referred to as parabolic reflector) - is illustrated which presents a symmetric optical path for both polarizations. The available reflector area is calculated as $A_{\text{phy}} = \pi D^2/4$ where the reflector diameter is $D = 2r$. With basic trigonometry, the half-subtended or half-opening angle θ_{e} (sometimes

also denoted θ_0) can be expressed in terms of the focal length, f, to diameter ratio, f/D, according to

$$\begin{aligned}\tan\theta_e &= \frac{r}{f - z_0} = \left\{ z_0 = \frac{r^2}{4f} \right\} = \frac{r}{f - \frac{r^2}{4f}} \\ &= \left\{ r = \frac{D}{2} \right\} = \frac{\frac{D}{2}}{f - \frac{D^2}{16f}} = \frac{1}{2} \frac{\frac{f}{D}}{(\frac{f}{D})^2 - \frac{1}{16}}. \end{aligned} \tag{2.1}$$

The half-angle identity for arctan

$$\tan\frac{x}{2} = \frac{\sin x}{1 + \cos x} \Rightarrow \arctan x = 2\arctan\frac{x}{1 + \sqrt{1 + x^2}}, \tag{2.2}$$

can be used to simplify (2.1) as

$$\theta_e = 2\arctan\left(\frac{1}{4\frac{f}{D}}\right). \tag{2.3}$$

From (2.3) a correlation is found for large θ_e with low f/D and small θ_e with high f/D as presented in Fig. 2.2c. Typically a low f/D results in a more compact feed design with larger bandwidth and is a popular choice for large reflector arrays [30], [56]. Traditionally, for single dish observations high f/D Cassegrain reflector geometries have been used which require large feeds (i.e. relative to its wavelength) often limited to octave bandwidths. For the sake of feed design, θ_e specifies the break-point of where illuminating power instead becomes spill-over power for the specific reflector geometry. With spill-over power predominantly being an issue when it is picked up from the hot ground. This break-point should not be seen as a hard limit due to diffraction effects and telescope orientation, but is a good reference point. This is further discussed in Section 2.5. When designing the feed for a dual-reflector system, the half-subtended angle from the feed towards the sub-reflector is the most relevant. Often we express this in an effective f/D. To quantify feed illumination properties of a specific θ_e, we can evaluate the resulting reflector performance with the aperture- and sub-efficiencies.

2.2 Efficiencies

For a circular reflector aperture the maximum gain possible, as well as the highest side-lobe levels, is achieved with a uniform illumination distribution.

For most applications this would not be practical or desired, and therefore the power distribution is tapered towards the reflector edge. This yields a lower gain, but also lower side-lobe levels which is desirable. The corresponding lower gain, G, gives an effective reflector area,

$$A_{\text{eff}} = G\frac{\lambda^2}{4\pi}, \tag{2.4}$$

where λ is the wavelength. The effective reflector area tells us "how well" the real physical reflector area, A_{phy}, is illuminated. The relation between these areas is the dimensionless ratio we call aperture efficiency η_{a}

$$A_{\text{eff}} = \eta_{\text{rad}}\eta_{\text{a}}A_{\text{phy}}. \tag{2.5}$$

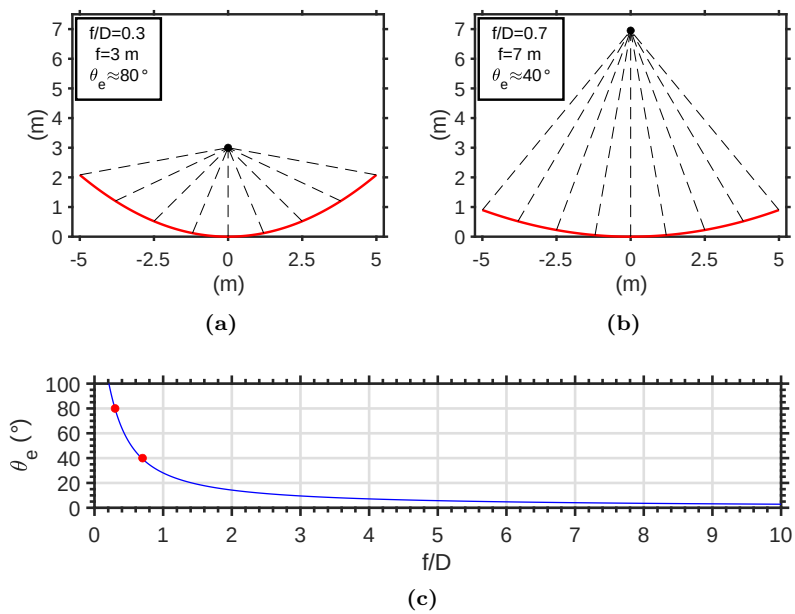

Figure 2.2: Illustration of a "deep" (a) and "shallow" (b) reflector geometry. In (c) the relation from (2.3) is presented, f/D=0.3 and 0.7 highlighted.

where η_{rad} is the antenna radiation efficiency. Most often η_{rad} is not included as it is assumed to be high for most low-noise feed and reflector systems. The product of $\eta_{\text{rad}}\eta_{\text{a}}$ is sometimes referred to as the aperture efficiency in different literature but is rather defined as the antenna efficiency [57]. In reality, more factors affect the final effective area (or gain) achieved and correspondingly reduces the performance. Such effects that are not related to feed illumination properties can be summarized in an additional factor η_{dish} included on the right side of (2.5) that represents all losses in the reflector structure [57] from dissipative and transparency loss, surface error, jitter in pointing, and blockage. Depending on the reflector structure and system, these can be very different (e.g. offset reflector has no blockage). It is common to give system specifications of a certain aperture efficiency (or indirectly through sensitivity) with η_{dish} accounted for as it is mostly (not always e.g. blockage) independent of the feed design. The aperture efficiency η_{a} tells us directly about the feed illumination properties independent of reflector size (assuming it is large enough). The feed dependent aperture efficiency is itself divided into multiple sub-efficiencies [58] that characterize the feed pattern evolution over frequency. For a prime-focus reflector η_{a} is calculated (in linear units) according to

$$\eta_{\text{a}} = \eta_{\text{ill}}\eta_{\text{sp}}\eta_{\text{BOR1}}\eta_{\text{pol}}\eta_{\text{ph}}, \tag{2.6}$$

where η_{ill} is the illumination efficiency and a measure of the aperture illumination; η_{sp} is the spill-over efficiency, quantifying how much power hits the reflector; η_{BOR1} is the BOR1 (azimuth mode) efficiency and a measure of power in first order azimuth modes; η_{pol} is the polarization efficiency for peak cross-pol in the 45 degree plane; and η_{ph} is the phase efficiency quantifying the phase distribution over the aperture. The phase efficiency η_{ph} is dependent on the feed's location relative to the focal point of the reflector. Ideally the phase center of the feed is near-constant resulting in a high phase efficiency over the full bandwidth. The product of $\eta_{\text{ill}}\eta_{\text{sp}}$ is the trade-off between how well the reflector is illuminated and how much power is lost to spill-over. The optimal reflector-edge taper-level at θ_{e} for a system only designed for high η_{a}, can be found as the maximum of $\eta_{\text{ill}}\eta_{\text{sp}}$ as is illustrated in figure 2.3 of [40]. However, a wideband design optimized for high sensitivity, side-lobe levels, or other specifications depends on more factors which is further discussed in Section 3.4. In Fig. 2.2c the difference between a "deep" and "shallow" reflector is illustrated. For the deep case, the feed located at the black focus

point is more protected from the ground temperature and most power hits the reflector. However, it will also result in a less uniform aperture illumination as the tapered pattern drops off quickly towards the reflector edge. The reverse case applies for the shallow reflector where the aperture will be strongly illuminated, but a lot of power will be "spilled" over the reflector edge. For sensitivity; the total system noise temperature has contributions from surrounding sky brightness temperature, internal receiver temperature and together with the spill-over noise picked up from ground it will affect the choice of taper for highest sensitivity over frequency. Due to the variations in noise components with frequency, this trade-off can be complicated over large bandwidths. The possibility to *shape* reflector geometries and use *spill-over shields* also influence the trade-off as generally a much higher η_{a} can be achieved [24], [30] with little penalty from spill-over. In Paper E this trade-off is specifically explored in an unshaped prime-focus reflector with a shielded rim addition together with a wide feed pattern.

2.3 Sensitivity

To study radio sources in space, we must separate their weak radiation from the general surroundings. We quantify the telescope systems ability to do this through the FoM *sensitivity* that characterizes the signal-to-noise ratio for radiometric detection. The specific intensity I_ν (or brightness) is an intrinsic property of the radiating source under observation. The incoming flux density of most radio sources ($\Omega_{\mathrm{src}} \ll 1$ rad) can be calculated as

$$S_\nu = \iint_{\Omega_{\mathrm{src}}} I_\nu \mathrm{d}\Omega, \tag{2.7}$$

where Ω_{src} is the solid angle subtended by the source seen from the observer. In the Rayleigh-Jeans limit of Planck's law the brightness of a radio source can be expressed as a brightness temperature according to

$$T_{\mathrm{b},\nu} = \frac{I_\nu \lambda^2}{2k_{\mathrm{B}}}, \tag{2.8}$$

where λ is the wavelength and k_{B} the Boltzmann constant. The brightness temperature corresponds to the physical temperature an equivalent blackbody source would need in order to produce the brightness I_ν. Flux density and

brightness temperature are therefore proportional as concluded from (2.7) and (2.8). Repeating from the introductory chapter, for S_ν source flux density at the aperture, the SNR from observation on-source is

$$\mathrm{SNR} = \frac{S_\nu}{\mathrm{SEFD}}\sqrt{t\Delta\nu}, \tag{2.9}$$

where t is the integration time and $\Delta\nu$ is the available bandwidth, and aforementioned sensitivity in form of SEFD is

$$\mathrm{SEFD} = \frac{2k_\mathrm{B}T_\mathrm{sys}}{A_\mathrm{eff}}. \tag{2.10}$$

The sensitivity is sometimes also expressed in $A_\mathrm{eff}/T_\mathrm{sys}$ where a larger number means better sensitivity and with units of m^2/K which is just another form of (2.10) as $A_\mathrm{eff}/T_\mathrm{sys} = (2k_\mathrm{B}/\mathrm{SEFD})$. In the SKA project for example, $A_\mathrm{eff}/T_\mathrm{sys}$ is the preferred notation to simplify for proportional expressions of array sensitivity. These expressions include the effective reflector area as a factor which means that a larger reflector would give better sensitivity. To compare sensitivity of different feed/receiver systems without accounting for the size of the reflector, the normalized ratio $T_\mathrm{sys}/\eta_\mathrm{a}$ is a good choice where a lower number means better sensitivity.

2.4 System noise temperature

The total noise power in the receiver system is commonly expressed by an equivalent system noise temperature, T_sys, containing both external and internal contributions. For a single-pixel receiver the system noise temperature can be expressed as

$$T_\mathrm{sys} = \eta_\mathrm{rad}T_\mathrm{a} + (1-\eta_\mathrm{rad})T_\mathrm{phy} + T_\mathrm{rec}, \tag{2.11}$$

where η_rad is the antenna radiation efficiency, T_a is the antenna noise temperature, T_phy the physical antenna temperature, and T_rec the input referred receiver noise temperature. The latter includes the noise contributions from the receiver components such as possible filters, couplers for gain and phase calibration, and the first stage LNA. Possible mismatch between feed and LNA are also included in the receiver noise temperature. It is clear from (2.11) that an antenna at lower physical temperature, is less dependent on high η_rad for

low loss contribution. The same goes for the contribution of T_{rec}. As previously alluded to, this put emphasis on minimization of T_{a} when the T_{rec} is on comparable level as the background noise of the observable sky (Fig. 1.3). The antenna noise temperature T_{a}, represents the noise contribution to the system temperature from brightness sources surrounding the reflector system. In Section 2.5 contributions to T_{a} will be discussed together with the calculation model to estimate it. A typical receiver (Rx) chain is illustrated in Fig. 2.3

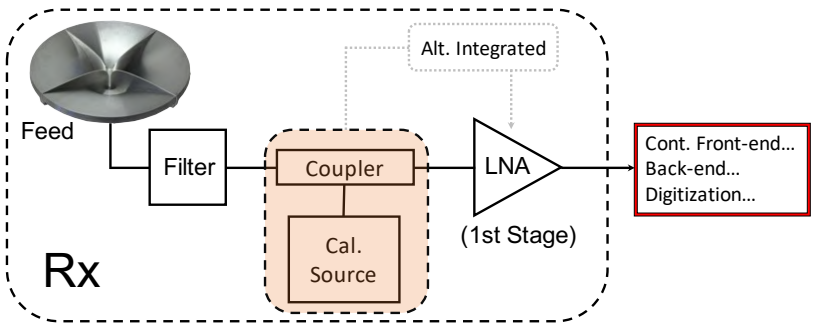

Figure 2.3: Typical wideband receiver chain illustrated including the alternative option to include gain calibration directly in the LNA [13], [25].

where noise before and inside the first component with high gain (first stage LNA) should be minimized due to the cascading effect in Friis's noise formula [2]. The components inside the dashed line can either be cooled to cryogenic temperatures, or operated at room temperature. The instrumentation further down the receiver chain is not noise-less and for a low-noise system, noise contributions from second stage LNAs, cables, digitization, and optical fibers could be significant. Additional noise can depend on radome material around the reflector, and dewar window configuration.

2.5 Antenna noise temperature

In Fig. 2.4a, $P(\hat{\boldsymbol{r}}, \theta, \phi, \nu)$ represents the power pattern of the telescope which is pointing in the $\hat{\boldsymbol{r}}(\theta_{\mathrm{p}})$=$\hat{\boldsymbol{r}}$ direction for observation, θ is the spherical coordinate angle from zenith and ϕ in azimuth, and ν the frequency. The pointing direction is generally referred to by only the angle in degrees given from *zenith*. In this work, this angle is referred to as *zenith angle* or *pointing angle* and

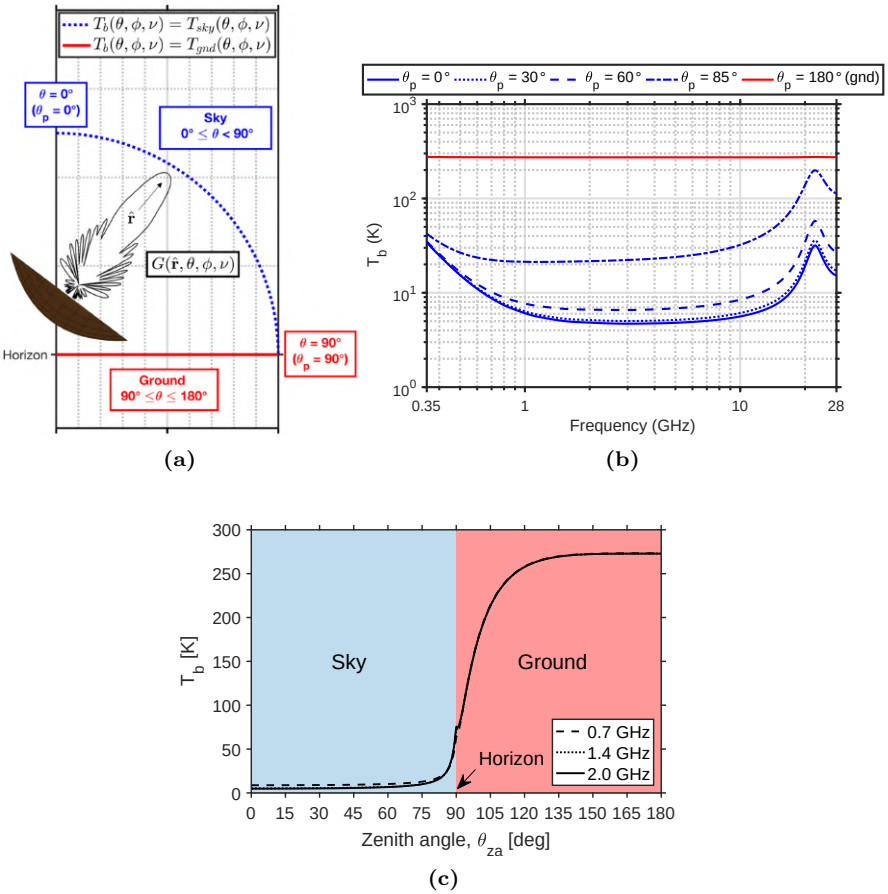

Figure 2.4: The concept of surrounding brightness temperature for a telescope is illustrated in (a). In (b) the brightness temperature, T_b, over 0.35–28 GHz for the SKA general model [59] is presented for a few zenith angles, and in (c) over zenith angle for a few frequencies.

denoted as θ_za or θ_p interchangeably, with zenith being $\theta_\mathrm{za} = \theta_\mathrm{p} = 0°$. Another way of giving the pointing direction can be as relative to the horizon in the form of elevation θ_elev=90 − θ_p. It is unfortunately common to also use the notation θ for elevation which easily is confused with the spherical coordinate from zenith. The model of the surrounding brightness temperature,

$T_{\mathrm{b}}(\theta,\phi,\nu)$, seen by the telescope has several contributions [59]. These are mainly: emission caused by gases and aerosols in our atmosphere; the cosmic microwave background (2.73 K) and the galactic emission; and the emission from the ground as well as scattering. Often an ideal-weather model is assumed during optimization not accounting for daily [60] or seasonal variations, and the solar activity. In Fig. 2.4b, the influence from galactic synchrotron emission in the low-frequency range can be compared to the water-vapor in the atmosphere around 22.2 GHz. The $T_{\mathrm{b}}(\theta,\phi,\nu)$ distribution is a function of angle, but can in its simplest form be thought of as the combination of two regions: above the horizon, and below the horizon:

$$T_{\mathrm{b}}(\theta,\phi,\nu) = \begin{cases} T_{\mathrm{sky}}(\theta,\phi,\nu) & 0^\circ \leq \theta < 90^\circ \\ T_{\mathrm{gnd}}(\theta,\phi,\nu) & 90^\circ \leq \theta \leq 180^\circ \end{cases}, \tag{2.12}$$

with dependence in θ but assumed symmetric in ϕ. Depending on the site and surroundings, the actual $T_{\mathrm{b}}(\theta,\phi,\nu)$ can vary with both θ and ϕ. For non-symmetric surroundings with mountains, buildings, and water, the site specific model is azimuth dependent. The effective ground-temperature, $T_{\mathrm{gnd}}(\theta,\phi,\nu)$, can be strongly varying with angle of incidence given reflections, emission and absorption in ground. In Fig. 2.4c, the result of this together with the atmospheric effect near the horizon is seen in $T_{\mathrm{b}}(\theta,\phi,\nu)$ presented for a few frequencies. A common approximation is to assume a simplified ground temperature as constant ∼290 K in the range $90^\circ \leq \theta \leq 180^\circ$. The difference between such models and effect in antenna noise temperature calculation have been investigated in [61] for example. The total antenna noise temperature, $T_{\mathrm{a}}(\hat{\boldsymbol{r}},\nu)$, is calculated for each direction of pointing and frequency with the integral given in (2.13). The surrounding brightness temperature is weighted with the total power pattern (co and cross-polarization) of the telescope pointing in the direction of $\hat{\boldsymbol{r}}$ and integrated over the full sphere

$$T_{\mathrm{a}}(\hat{\boldsymbol{r}},\nu) = \frac{\int\int_{4\pi} P(\hat{\boldsymbol{r}},\theta,\phi,\nu) T_{\mathrm{b}}(\theta,\phi,\nu)\, \sin\theta\, d\theta\, d\phi}{\int\int_{4\pi} P(\theta,\phi,\nu)\, \sin\theta\, d\theta\, d\phi}. \tag{2.13}$$

In analysis we attempt to separate the contributions to T_{a} for clarity. We can refer to the inevitable background noise picked up by the main-beam as T_{sky}. The other important component to T_{a} is the noise picked up from spill-over power received from the ground which we can limit with good feed and reflector design. This component is denoted as T_{sp} or T_{spill}. Both T_{sky} and T_{sp} are

dependent on the pointing angle of the telescope, as seen in Fig. 2.4c. When the main-beam is pointing closer to the horizon (larger θ_p), the path through the atmosphere is longer, but the effective ground temperature's incident angle also changes, the combined effect is an increased T_a. In Fig. 2.5, the spill-over is simplified and illustrated as blue lines for the feed in a prime-focus reflector. The magnitude of the noise temperature contribution from spill-over depends on how much of it is terminated on the ground compared to on the sky. This can change significantly with θ_p depending on the feed design and reflector geometry and what side-lobe response this yields. With an approximation of (2.13), the antenna noise temperature can be calculated by a simple equation using the spill-over efficiency η_{sp} [51]. The antenna noise temperature is then given according to

$$T_a = \eta_{sp} T_{mb} + (1 - \eta_{sp}) T_{gnd}, \tag{2.14}$$

where the factor $\eta_{sp} T_{mb}$ is main-beam's sky-brightness contribution as we assume all feed power within θ_e is terminated on the sky. This would be the main-beam contribution we call T_{sky}. The term $(1 - \eta_{sp}) T_{gnd}$ represents the spill-over noise temperature, T_{sp}, picked-up from beyond the reflector-rim which is assumed to only be influenced by the ground temperature in this case, T_{gnd}. For an axially-symmetric prime-focus reflector (Fig. 2.5), the feed is pointing toward the ground (symmetric spill-over only for zenith), and this approximation is somewhat reasonable. This of course depends on possible back-lobe and side-lobe levels, diffraction and scattering.

For a dual-reflector system such as an offset Gregorian reflector, spill-over contribution is not as straightforward. In Fig. 2.6 the spill-over from feed towards sub-reflector (blue) and sub-reflector towards main-reflector (red) are illustrated in a simplified way. Due to the asymmetry of the structure, the

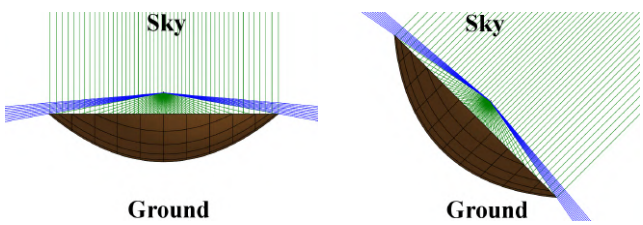

Figure 2.5: A simplified illustration of feed spill-over (blue) for an axially-symmetric prime-focus reflector, dependent of pointing direction.

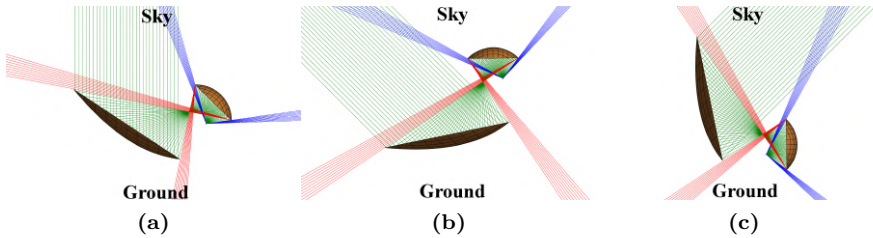

Figure 2.6: Illustration of feed (blue) and sub-reflector (red) spill-over dependence on tipping direction for an offset Gregorian reflector. (a) Zenith; (b) Feed-up configuration; (c) Feed-down configuration.

spill-over contribution is very dependent on which direction the telescope is moving in elevation or tipping [24]. When the feed and sub-reflector moves away from the ground to point the telescope closer to the horizon, it is defined as *feed-up* configuration seen in Fig. 2.6b. If the feed moves towards the ground to point the telescope closer to the horizon, it is defined as *feed-down* configuration seen in Fig. 2.6c. By using a ground or spill-over shield for the feed-down configuration, the spill-over noise can be reduced significantly [24], [30], [56], [62]. Due to the asymmetry of the reflector geometry, the spill-over dependence on zenith angle, can also vary between the two orthogonal polarizations. To account for all the effects of such a complex geometry, the full calculation of (2.13) will give a more representative result than (2.14). This is important in high-sensitivity targeted feed designs (Section 3.4).

2.6 Intrinsic cross-polarization

Radio astronomy observations especially those focusing on the polarization state of sources, require a good polarimetric response from the telescope as well. This firstly means that the telescope, with receiver system, should be able to measure the orthogonal polarization components, i.e. it must be dual-polarized. Systems that can do this separation are generally called polarimeters. Typically, cross-polarization ratios are used as the FoM for how good polarimeters telescopes are. The intrinsic cross-polarization ratio (IXR) introduced in [63], is the only such ratio that is independent of the coordinate

system. It can be understood as a measure of the relative error in a polarimeter. The IXR of a reflector telescope is calculated by extracting the maximum and minimum amplitude gain as the invariants of the reflector beam pattern's Jones-matrix. The Jones-matrix is formed from the two sets of orthogonal components, one set for each polarization, in the reflector beam patterns. Each row is formed from the response of one polarization. The two polarizations are denoted as vertical (V) and horizontal (H) corresponding to the telescope's axes of movement. The Jones-matrix is formed as

$$\mathbf{J} = \begin{pmatrix} \mathbf{G}_{\mathrm{VV}} & \mathbf{G}_{\mathrm{VH}} \\ \mathbf{G}_{\mathrm{HV}} & \mathbf{G}_{\mathrm{HH}} \end{pmatrix}, \tag{2.15}$$

where $\mathbf{G}_{\mathrm{XX}}$ is the reflector beam pattern corresponding to each polarization's orthogonal components (i.e. co- and cross-polarization). From a single-value decomposition of (2.15), the maximum and minimum amplitude gain, denoted as g_{max} and g_{min} respectively, can be extracted. IXR is calculated according to

$$\mathrm{IXR} = \left(\frac{g_{\mathrm{max}} + g_{\mathrm{min}}}{g_{\mathrm{max}} - g_{\mathrm{min}}} \right)^2, \tag{2.16}$$

where a large IXR indicates that g_{max} and g_{min} are close in value, resulting in a better polarimetric response. For the SKA-MID feed systems on the SKA reflector, the IXR is required to be better (more) than 15 dB within half-power beamwidth (HPBW) over the specified frequency bands.

CHAPTER 3

Numerical Ultra-wideband Feed Design and the Quad-ridge Flared Horn Technology

This chapter gives an overview of the Quad(ruple)-ridge Flared Horn as a wideband reflector feed and a brief background of the ridge waveguide technology. In addition, typical design formulation of the horn and ridge profiles, optimization, radiometric system characterization, and manufacture process are presented with qualitative examples from work within the Papers A-E and the development of the SKA Band 1 and Band B QRFHs.

3.1 Ridge waveguide

The ridge waveguide technology was initially realized by loading regular waveguides with a dual-ridge structure [64], [65]. The dual-ridge structure increases the bandwidth (single-mode) as it lowers the cut-off frequency by a factor of four compared to a same-sized regular waveguide. The quad-ridge waveguide [66] actually has less (single-mode) bandwidth than the dual-ridge, due to mode splitting that also reduces the cut-off for high-order modes [67]. Despite this, quad-ridge structures still have high usability as many applications

do not require single-mode bandwidth. The quad-ridge structure also enables dual-linear polarization, which is effectively essential in many applications, e.g. radio astronomy and space geodesy which are the application areas this thesis is targeting.

3.2 The Quad-ridge Flared Horn

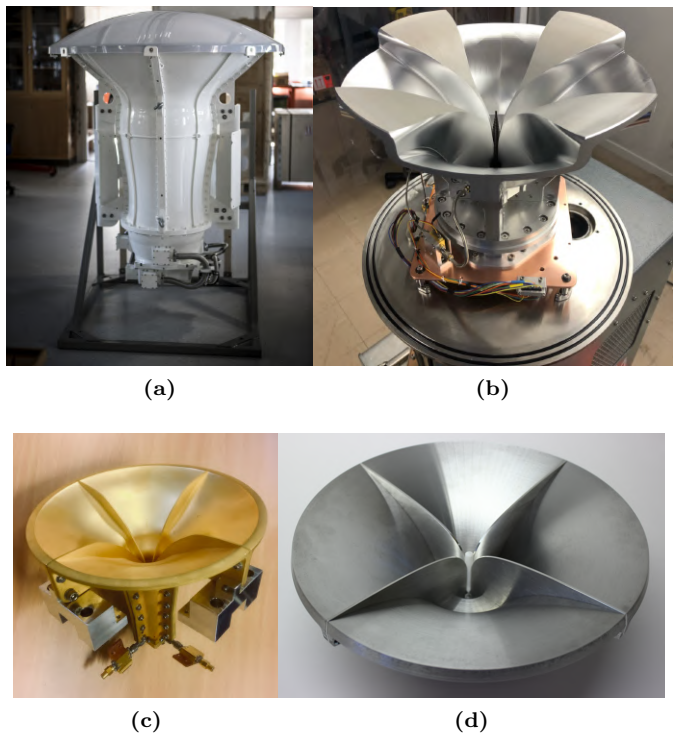

(a) **(b)**

(c) **(d)**

Figure 3.1: Examples of Quad-ridge Flared Horn designs: (a) 0.35-1.05 GHz (SKA Band 1); (b) 1-20 GHz (ATA Prototype); (c) 4.6-24 GHz (SKA Band B); (d) 1.5-15.5 GHz (BRAND/Effelsberg)

The Quad-ridge Flared Horn (QRFH) is a flared-out version of the aforementioned quad-ridge waveguide, and is commonly used as an ultra-wideband

reflector feed. The QRFH has low losses, a sturdy metal structure, and is straightforward to manufacture with proven methods for assembly. In Fig. 3.1, examples of QRFHs completely or partly designed by the author for different frequency ranges and projects are presented. The obvious characteristic features of the QRFH can be separated into the horn waveguide wall, and the four ridges with planar or non-uniform thickness extending from the bottom-center of the structure. The concept design was predominantly developed and refined at California Institute of Technology (CalTech) with single-ended feed configuration [39], [40], and in differential (or quadraxial) setup at Stellenbosch University [41], [42],[44]. The structure itself was known long before that as a functional broadband feed in different configurations [46], [68]. The QRFH also exists in and open-boundary version (i.e. no horn wall), referred to as open-boundary QRFH [69] or less commonly as a Vivaldi-horn antenna. The open-boundary QRFH is a standard wideband probe in many anechoic measurement chambers covering multi-octave frequency ranges. In this thesis, all the work presented is done with standard QRFH that has a horn wall. The quad-ridge structure, see Fig. 3.2a, provides the dual-linear polarization property integrated as part of the horn, removing the need for an external orthomode transducer (OMT) typically used in octave horns [70]. QRFHs have been designed and manufactured as feeds for reflector geometries spanning f/D=0.3-2.5 with varying performance [40] using both square and circular waveguide structure for UWB bandwidth [71]. Typically a semi-constant 10 dB full beamwidth of 90°-130° is possible for 6:1 bandwidth with a co-located phase center over frequency[39]. The circular waveguide structure is most commonly used, and with the best illumination properties achieved for reflector geometries in the range $0.4 \leq f/D \leq 0.5$. For such applications the aperture efficiency band-average is in the range of 55-65 % over 6:1 bandwidth and it decreases with frequency, as previously illustrated in Fig. 1.10. The waveguide base gives a sharp low-frequency cut-off which acts as an intrinsic high-pass filter that mitigates RFI below the operational bandwidth. This is a clear upside compared to non-waveguide type feeds typically based on log-periodic geometry [28], [35], [37] that can be more susceptible to out-of-band interference. The waveguide property also makes it easily scalable in frequency in a straightforward way, reducing design time and cost for adaptation to different frequency bands. With this feature comes also the possibility of producing dewars to span most of the usable radio frequency spectrum with

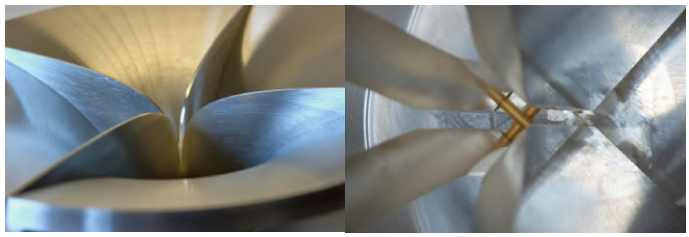

(a) **(b)**

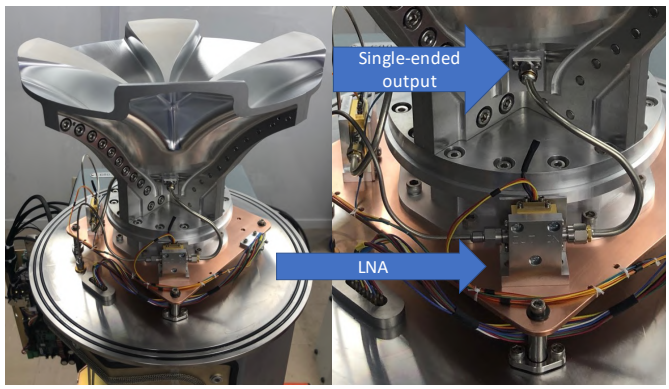

(c)

Figure 3.2: Some advantageous features of the ultra-wideband QRFH: (a) Dual-polarization built-in due to ridge-pairs; (b) Single-ended feeding using simple crossing coaxial launch-pins; (c) Single-ended output makes installation in dewar with LNA straightforward.

only a few feed packages [31].

Single-ended excitation

Arguably the most compelling reason why the QRFH is widely used, other than its bandwidth, is the possibility to design it with single-ended excitation requiring only one LNA per polarization, and thus keeping the complexity and cost low (Fig. 3.2c). To excite the two orthogonal polarizations, coaxial type launch-pins are used. For each set of ridges, the launch-pin is fed through

Figure 3.3: Coaxial single-ended excitation feed-through for a ridge-pair.

a hole in one ridge and contacted or terminated in the opposite ridge. This layout concept is illustrated in Fig. 3.3. In Fig. 3.2b, the crossing launch-pins of the two polarizations can be seen installed at the point of excitation in the QRFH. The region of coaxial excitation is a straight section of the ridge called the channel, and just below it lies the backshort often defined as a rectangular cut in the ridge, see Fig. 3.4. In the same figure, a top-view illustration of parameters defining the chamfered tip of the channel and angle between adjacent ridges is presented. The backshort structure is meant to function as an open reflection to ensure forward propagation but also enables wideband matching. Due to the very wide frequency ranges of QRFHs it is a semi-optimal solution, but it is practical and simple to realize. An optimized QRFH design with such a single-ended excitation can typically achieve input reflection on the order of -10 dB or less for 6:1 bandwidth [39]. In Paper D, a band-average input reflection of less than -13.6 dB over 20:1 bandwidth is reported. To reduce resonant effects in-band for such a super ultra-wideband design, an up-side down isosceles triangle presented the best solution for the backshort, and is illustrated in Fig. 3.5 where one ridge for each polarization is displayed. The single-ended configuration, together with the QRFH compact footprint makes the feed practical and easy to handle for reflectors with f/D around 0.5 or lower and applications in the gigahertz frequency range. These advantages provide for straightforward installation together with LNAs in a cryostat dewar for low-noise applications, see Fig. 3.2c. The drawback of single-ended excitation is clearly the asymmetry needed to offset the launch-pins along the optical axis (Fig. 3.2b). The result of this is a non-ideal mode

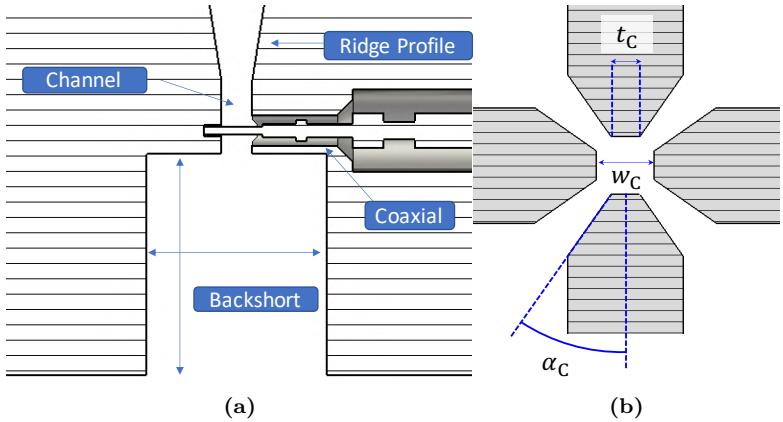

Figure 3.4: (a) Backshort, coaxial excitation and channel region of ridges in cross-sectional side view; (b) Top-view of the ridge-to-ridge separation in the channel region, displayed without launch-pins for visualization.

distribution which has been extensively studied in [42]. The practical result of this is different input reflection coefficients for the two polarizations and an unpredictable pattern asymmetry of usually low magnitude. This can be compensated for to a degree, by removing a distance close, or equal to the offset from the backshort of the ridge-pair corresponding to the offset polarization, see Fig. 3.5. A more critical issue is in the practical implementation

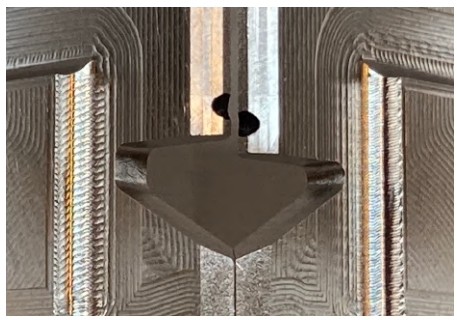

Figure 3.5: Offset between the two polarizations coaxial hole, and compensatory backshort-offset for QRFH in Paper D.

where a severe enough misalignment or asymmetry in the feed can trigger excitation of an unwanted even mode with low-frequency cut-off. The even mode cut-off is rapidly increasing with frequency as the ridges flare towards the aperture with increasing ridge-to-ridge distance and therefore the mode becomes evanescent. This results in what is sometimes called a trapped mode that can cause detrimental resonances in the QRFH [70]. To remove the last asymmetry it has been shown that quadraxial or differential feeding can be used in the QRFH with success and effective high-order mode suppression through pure-mode excitation [41]. With emerging manufacture technologies, the quadraxial technique can potentially realize pure-mode excitation over 8.5:1 bandwidth [44] with increased complexity of the QRFH throat structure as the penalty. The feed pattern evolution and symmetry benefits from a pure-mode excitation of the fundamental mode (circular waveguide: TE_{11}) at the feed point and limited number of high-order modes in the throat section of the horn (e.g TE_{12},TE_{13}...). This approach unfortunately increases complexity in receiver installation, and requires either differential LNAs, which are more expensive and difficult to realize, or a hybrid setup with single-ended LNAs that are phase and amplitude balanced which is not so straightforward to achieve and maintain during installation, maintenance and possible replacement inside a receiver. It is therefore less preferred compared to the single-ended solution from a practical stand-point.

Profile shape

The flaring profile cross-section of the QRFH's horn and ridges are separately defined, as illustrated in Fig. 3.6. These profiles are typically modeled by analytic functions (e.g. exponential, sinusoidal, tangential) with design parameters for adaptation to different reflector geometries available to a certain extent [39], [41]. This approach has proven to give good performance over multi-octave bandwidths and semi-stable beamwidths, with few parameters to include in the optimization. The example profile in Fig. 3.6, defined separately for the horn and ridge, is the exponential profile

$$\begin{aligned} x(z) = A\left(\frac{r_\mathrm{a}-r_\mathrm{t}}{e^{RL}-1}e^{Rz}+\frac{r_\mathrm{t}e^{RL}-r_\mathrm{a}}{e^{RL}-1}\right) \\ +(1-A)\left(r_\mathrm{t}+(r_\mathrm{a}-r_\mathrm{t})\frac{z}{L}\right) \end{aligned} \tag{3.1}$$

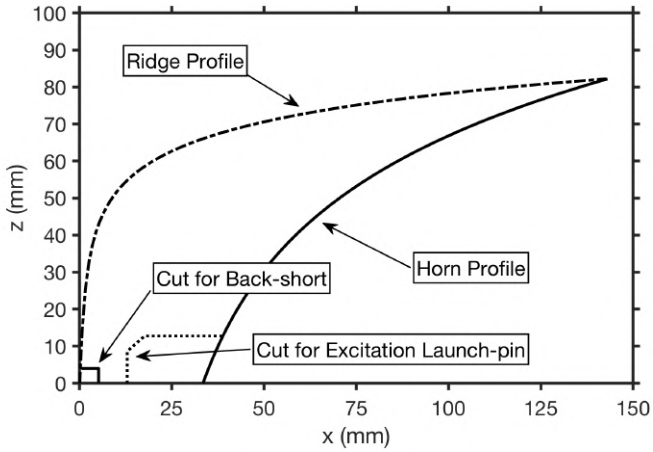

Figure 3.6: Exponential profile using (3.1) with values in Table 3.1.

where r_t and r_a define the throat (near excitation point) and aperture radius respectively. L is the taper length, with an exponential opening rate R. The linear contribution in each taper is defined by A. In Table 3.1, optimized parameters for the horn and ridge profile are presented. The design is found through optimization and presented in further detail in Paper B. The horn profile gives the rotational symmetric horn wall, while the ridge profile is often thickened to a planar profile. A spline-defined profile could also be

Table 3.1: Parameters for profile in Fig. 3.6, H is horn, R is ridge respectively.

Parameter	Value	Parameter	Value
R_H	0.030	R_R	0.093
A_H	0.944	A_R	0.978
$r_{a;\,H}$ ($=r_{a;\,R}$)	143.20 mm	L_H ($=L_R$)	82.20 mm
$r_{t;\,H}$ ($r_{t;\,R}$=0.1 mm, fix)	33.50 mm	Ridge thickness	2.00 mm

used, as is shown in [26] and [27]. The planar spline-defined profile is constructed from a number of points individually defined with an x (width) and z (length) coordinate. The points together make up a cubic-spline profile. In Fig. 3.7 the difference between an analytic exponential function and a spline-

defined planar profile is illustrated. The approach of using analytic functions typically generates a constantly increasing radial flare of the QRFH. With a spline-defined shape, the profile has more degrees of freedom resulting in a more custom shape as the end-product. The SKA Band 1 QRFH design did during early optimization, suffer from a sharp resonant mode phenomena at two frequency points in the band. This form of resonant mode was removed when the spline horn profile was optimized into the hour-glass shape, initially presented in figure 4 of [72] and further improved in the design presented in figure 1 of [26]. The hour-glass shape can be understood as implementing a form of mode-suppression, previously done with a mode-suppression ring near the excitation point of the QRFH [73]. This is to suppress unwanted high-order modes in the throat section of the horn and reduce phase errors in the aperture mode content. The main drawback of the spline-defined profile is a significant increase to the parameter search space for optimization, and less available design data for appropriate design model starting points.

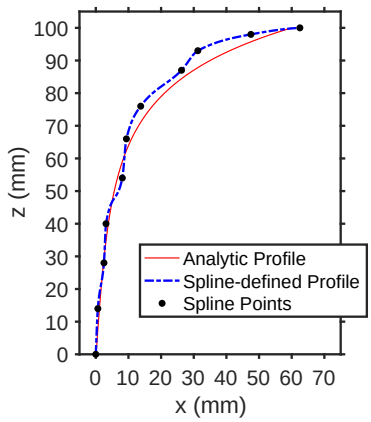

Figure 3.7: Examples of an analytic and a spline-defined profile illustrated.

Analytic-spline-hybrid profile

To reduce the parameter search space while not sacrificing all the degrees of freedom provided by the spline profile, the combined analytic-spline-hybrid (ASH) profile is introduced in Paper A. With this approach, the horn and ridge

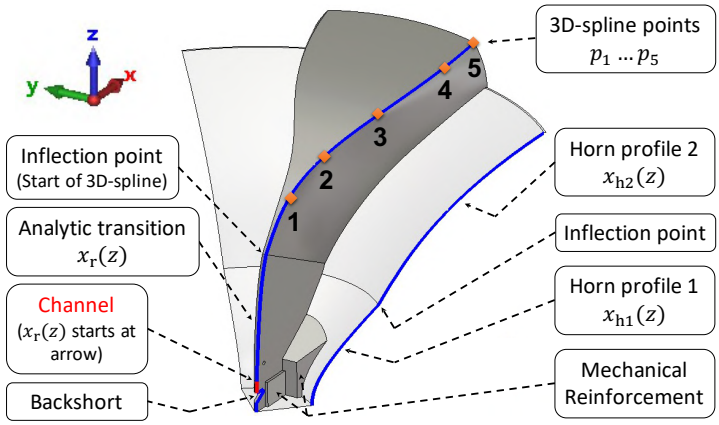

Figure 3.8: Analytic-spline-hybrid profile with 3D-cubic spline and corresponding interpolated points illustrated for a QRFH quarter-piece.

profile can be divided in sections which are either defined through analytic functions or splines. For visualization of this concept, separate analytic and spline-defined profiles are overlayed in Fig. 3.7 but could be combined to each represent different parts of the same profile - analytic-spline-hybrid. A two-step optimization scheme is proposed in Paper A, with initial analytic profile globally optimized due to the small number of variables. The resulting profile is transferred to ASH-profile in the form of spline-points, defined from the original analytic profile, which are then locally optimized. In Paper A, an improvement from the ASH-profile is seen compared to the analytic original profile after a smaller optimization run. Potentially this can offer further control of the QRFH impedance match, beamwidth and high-order mode-suppression while removing the resource demanding global optimization step of an all-spline-defined profile. In [27] the complete spline-defined QRFH consists of 60 parameters, which is a time-consuming effort to optimize and could be avoided if not all sections need to be spline-defined. In Paper D a parameter search space reduced by 25 % is explored where the combination of an analytic section, and spline-defined section of the ridge is used. To control the thickness of the ridge towards the aperture, a 3D-cubic spline is introduced, illustrated in Fig. 3.8, with precision local flare control resulting in improved cross-polarization and impedance match in the low-frequency part

of the band. This is due to further suppression of unwanted high-order modes [74].

3.3 Design optimization

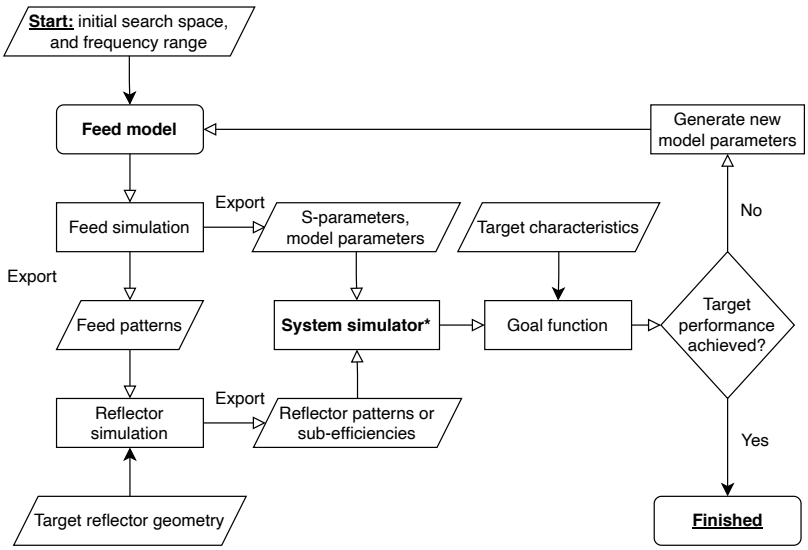

Figure 3.9: Typical optimization scheme in wideband feed design. *System simulator can be different depending on the application, and can also include parts of the outlined schematic.

It is clear from the previous section that the QRFH design is dependent on numerical optimization to find the optimal structure. CST Studio Suite [75] is one of many excellent electromagnetic simulators for modeling and simulating ultra-wideband feed designs such as the QRFH. To navigate the numerical parameter search space, an optimization schematic and procedure is needed. In Fig. 3.9, a common scheme for numerical optimization of the QRFH as a wideband reflector feed is illustrated. With a large search space of interdependent parameters, a stochastic optimization algorithm is normally used to control the process, e.g. particle swarm optimization (PSO) [76]. PSO can search large variable spaces and does not need a gradient to direct the optimization

forward. Commercially available electromagnetic (EM) simulators and toolboxes have internal optimization frameworks available that include a choice for stochastic algorithm. Most often detailed control of the process is needed, further motivated below, and therefore external software (e.g. MATLAB [77]) is used for the overall control. After the final EM-model has been transferred to a mechanical design (e.g. AutoDesk Inventor [78]) it is crucial that the mechanical assembly is checked with EM-simulation for any deviations from nominal performance before the highly time-consuming processes of creating drawings and manufacture begin. As previously mentioned above, the choice of QRFH profile influences how many design parameters are included in the optimization. A QRFH based on analytic profiles typically have 15–20 parameters [40] and the spline-defined profile can have as many as 60 parameters [27]. The starting point for the waveguide structure can be chosen from analytic calculations of the dominant mode's low-frequency cut-off [66]. Due to the large number of designed QRFH feeds available in research, generally good starting dimensions can be found in the literature for the most common frequency bands [40]. Ideally, optimization is set up with a goal function that finds the global minimum (or maximum) without additional input. However, this brute-force approach to optimizing a UWB feed over many frequency points is time-consuming, and a bit unrealistic. Therefore, multiple optimization runs are usually required to reach the desired specifications, with suitable modifications of the parametric design in-between runs being quite common. Typically, when a model close to desired specification is achieved, a local optimization algorithm including all parameters can be used for fine-tuning, as suggested by the ASH approach in Paper A and D. Depending on the application, constraints in the parameter search space to limit feed size and weight are examples of important factors for practical realization. In an offset Gregorian reflector for example, the feed/receiver can physically block the incoming waves if it is too large therefore diminishing one of the benefits of offset optics. In the design presented for Paper D the feed diameter is limited to fit inside an existing dewar, while in Paper E the small-dish prime-focus application put emphasis on reduced feed blockage of the reflector aperture. Desired performance characteristics typically seen in the goal function of a QRFH optimization are sensitivity, aperture efficiency, input reflection coefficient (or return loss), and reflector cross-polarization (IXR). In other approaches, optimization for specific pattern shape [48] or modal-content [43] are used to

indirectly realize some of these goals. Typically the goal function is designed such that penalties proportional to the deviation from the target is given per frequency point that misses the mark. When combining for different target characteristics in wideband design that are not evaluated at the same number of frequency points (e.g. return loss and aperture efficiency) the combined penalty must be weighted so to not lock the optimization in a local minimum for either target. For a wideband feed all these characteristics are evolving in a complex, sensitive way over the frequency range and require careful attention in optimization. In Paper C the importance of understanding the feed pattern evolution over frequency as one of these characteristics is illustrated with analysis of a 10:1 bandwidth QRFH. To keep track of, and evaluate the feed's application-specific characteristics during optimization, and later in the final design, we introduce system simulation as a concept below.

3.4 System simulator

Depending on the application and the complexity of the target characteristics, the system simulator outlined in Fig. 3.9 will have different functions. To achieve a highly optimized reflector-specific feed design, the system figure-of-merit needs to be predicted with good enough accuracy and speed during the design phase. For UWB feeds the frequency resolution used must also be fine enough to represent the large bandwidth. This is because performance can rapidly change over the bandwidth, with sharp in-band resonances not visible if the frequency step is too coarse. For optimization with many thousands of iterations even more emphasis is put on the iteration time. There are many powerful EM-simulator software packages (e.g. CST-MWS, FEKO, TICRA GRASP, HFSS) that offer a variety of toolboxes that partly fulfill this purpose. For maximum sensitivity optimization, each feed model iteration must be evaluated for the specific reflector application with effective area and radiometric noise response. For the wideband SKA Band 1 QRFH this system performance is predicted with a dedicated and custom made simulator [79] that can account for and evaluate all the requirements set by the SKA [23]. In Fig. 3.10a, the schematic of an iteration for such a simulator is illustrated with the main steps of the process. The overall algorithmic control is done in MATLAB, feed simulation is done in CST MWS and resulting feed patterns are imported to the reflector model in GRASP. The full reflector beam

patterns are calculated in GRASP with physical optics (PO) and physical theory of diffraction (PTD). From these patterns, the effective area A_{eff} and the IXR are calculated (among other things). The reflector power patterns are also used to weight the provided brightness temperature model [59] for radiometric antenna noise temperature calculation according to (2.13) over all frequencies and zenith angles. The antenna noise temperature calculation gives a detailed response to specific surrounding brightness temperature and together with the inclusion of receiver noise temperature it gives a predicted T_{sys} for the entire system. The final product is the sensitivity as A_{eff} over T_{sys} calculated from (2.4) and (2.11) which goes into the goal function. In Section 3.4 it is further illustrated why optimization for maximum sensitivity over wide frequency ranges require detailed application understanding. The approximate PO+PTD simulation method has been proven fairly accurate compared to full-wave simulations [80]. For low frequencies, the fullsphere PO+PTD simulation of a 15 m dish is quite fast with only a few minutes for maximum frequency. The integration mesh needed is relatively coarse, and therefore suitable for a large number of iteration. For high frequency feeds (without significant back-lobes), the system simulation can be done by approximate methods where the main-reflector is masked to reduce PO calculation time significantly [81],[61]. Reflector feeds can also be designed for maximizing aperture efficiency η_{a} which can be seen as a partial system simulation. This is often done for large single-dish reflectors where the target is to use as much of the physical reflector area as possible to indirectly design for maximum sensitivity $A_{\text{eff}}/T_{\text{sys}}$. This approach can also be suitable for a reflector geometry strongly shielded, where the spill-over contribution is low. This is further explored in the next chapter and Papers D-E. Designing for η_{a} is compelling in terms of iteration time as it is a property that can be calculated with good accuracy directly from the simulated feed pattern [33], [58]. This allows for finer frequency steps over very wide bandwidths, where normally reduced frequency steps must be used in full reflector pattern evaluation for time-constraint reasons. Over a 20:1 bandwidth ratio, resonances or pattern deviations in-band may be hidden between coarse frequency steps. In Paper A-C, and Paper D the QRFH bandwidth spans a decade or beyond in frequency, and is designed using the η_{a} as the partial target, calculated directly from the feed pattern.

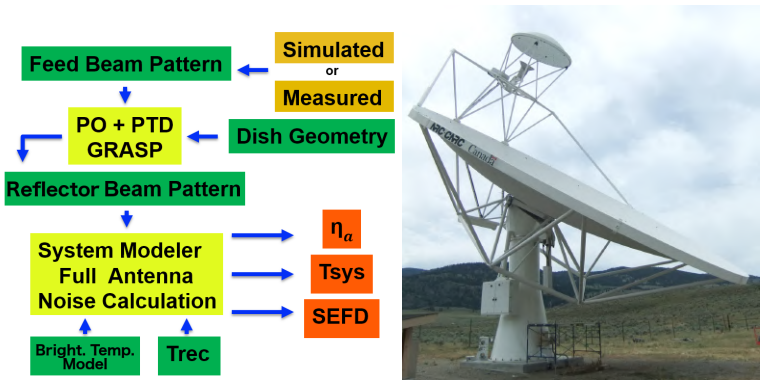

(a) (b)

Figure 3.10: (a) Schematic of a PO+PTD system simulator that models feed performance on a reflector system; (b) Example of a complete reflector system that can be modeled by [79]. The image shows the first SKA Band 1 QRFH prototype mounted on the Dish Verification Antenna 1 (DVA-1) in Penticton, BC, Canada in 2016.

Design for high sensitivity

The figure-of-merit for radio telescope receiver systems, is ultimately the observational sensitivity as introduced in (2.10). Sensitivity is expressed as $A_{\text{eff}}/T_{\text{sys}}$, SEFD, or normalized as $T_{\text{sys}}/\eta_{\text{a}}$ depending on the application. As discussed in Chapter 2; to achieve high sensitivity several factors should be taken into account. The reflector geometry and frequency band are important for the design. The effective area A_{eff} is clearly dependent on the available reflector area, as well as improved aperture efficiency. The total system noise temperature is important, but also understanding the contribution from its components (2.11) is important as this can dictate the design trade-off. The relative improvement in sensitivity by reducing the spill-over a few kelvin, is dependent on if the receiver noise and sky brightness are of the same order of magnitude as the spill-over. With LNA noise contributions on the order of a few kelvin for cryogenic designs [9] and 8–10 K for room temperature designs [7], [13], the spill-over becomes very important. The device noise from transistors increase intrinsically with frequency, but also with bandwidth as it is more

difficult to impedance-match LNAs over large frequency bands. The LNA noise contribution at frequencies below ∼20 GHz is most often comparable in size to the spill-over and sky brightness contributions. This puts stronger emphasis on reducing the spill-over noise for the reflector feed system. The feeds for the SKA are optimized for maximum sensitivity, $max(A_{\mathrm{eff}}/T_{\mathrm{sys}})$, with a required absolute level that must be achieved over each frequency band. The SKA Band 1 feed package fulfills the sensitivity specification over $\theta_{\mathrm{p}} \in [0°, 60°]$ required for the SKA, as shown in Fig. 4a of [26]. It achieves high and stable aperture efficiency with a band-average of 80% and maximum of 85% over 3:1 bandwidth. As a way to reduce edge diffraction, the QRFH is designed with an aperture-matching shape [82]. For frequencies below 600 MHz the galactic brightness temperature contribution is significant, as shown in Fig. 2.4b. For 350 MHz, T_{sky} is in the order of 35 K, which is seven times the spill-over contribution ($\theta_{\mathrm{p}} = 60°$) and two times the receiver noise temperature at this frequency for SKA Band 1, see Fig. 3.11. This results in a lower achievable sensitivity than at the upper frequency range. At 900 MHz the contribution from the sky brightness is in the order of 7-8 K and spill-over close to 2 K, and therefore a higher sensitivity goal is realistic. This again puts emphasis on the importance of understanding the wideband feed performance over frequency, as the environmental conditions change drastically within the same band. The

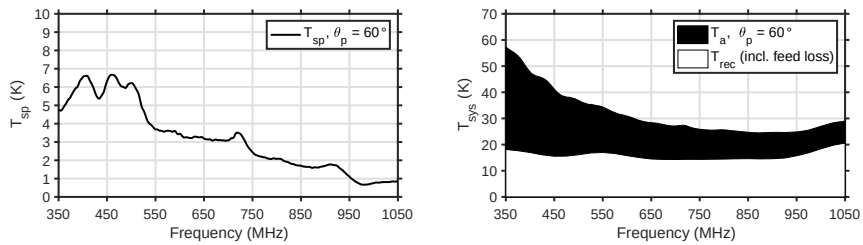

Figure 3.11: (a) Spill-over noise, T_{sp}; (b) Total system noise, T_{sys} for the SKA Band 1 feed simulated on the SKA dish.

shaping of the offset Gregorian reflector has proven to be an effective tool to increase the systems aperture efficiency and therefore sensitivity [30]. For the shaped 15 m SKA offset Gregorian reflector a ∼10% increase in aperture efficiency is achieved compared to an unshaped version, and a spill-over shield is also implemented that extends 40 degrees downward from the sub-reflector

rim [56]. In the feed-down configuration, the shield mitigates ground spill-over pick-up from the feed. The spill-over shield concept is illustrated by a generic offset Gregorian dish in Fig. 3.12. Compared to the non-shielded concept in Fig. 2.6, the spill-over shield improves the system sensitivity significantly (illustration in Figure 6 of [24]). The feed-down configuration also allows for installation and maintenance with the feeds in a horizontal position close to the ground compared to the feed-up technique. The optimal trade-off be-

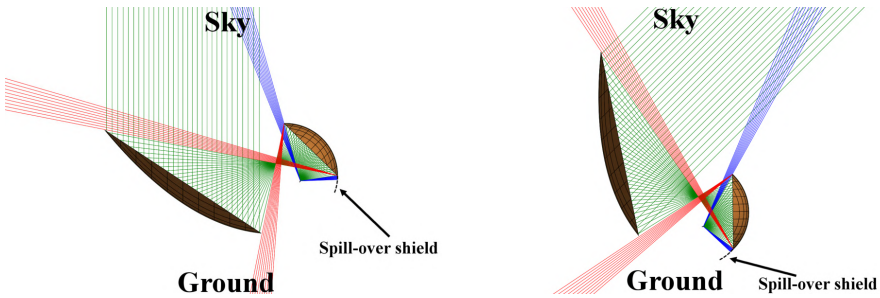

Figure 3.12: Illustration of the spill-over shield effect.

tween spill-over and aperture efficiency achieved by a QRFH design for high sensitivity, is specific to the reflector geometry and frequency range intended. For example, the SKA Band 1 QRFH is optimized for high sensitivity on the shaped SKA dish with half-subtended angle of $\theta_e = 58°$. The MeerKAT dish has a smaller $\theta_e = 49°$. This results in over-illumination of the MeerKAT sub-reflector from the SKA Band 1 feed and higher spill-over. Furthermore, the MeerKAT dish is unshaped with a smaller main-reflector diameter than the SKA dish, which results in a lower expected $A_{\text{eff}}/T_{\text{sys}}$ sensitivity when illuminated by the SKA Band 1 feed, see Fig. 3.13a. Both reflector configurations are feed-down. Once again this emphasizes the need for accurate and fast system simulation during optimization to adapt designs for their application. In Fig. 3.13c, a good example of the obtained agreement between simulated and measured sensitivity is presented for the SKA Band 1 QRFH on a 13.5 m MeerKAT reflector ([26]). The PO+PTD system simulator (Fig. 3.10a) is used for the simulation and to measure the sensitivity drift scans of known sources are performed. A general brightness model of the sky, such as [59], does not account for the brightness temperature near specific sources in the sky. Corrections are therefore applied in the results of [26] by incorporating a more

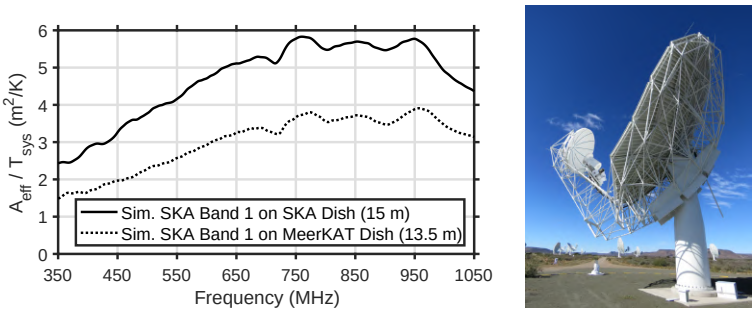

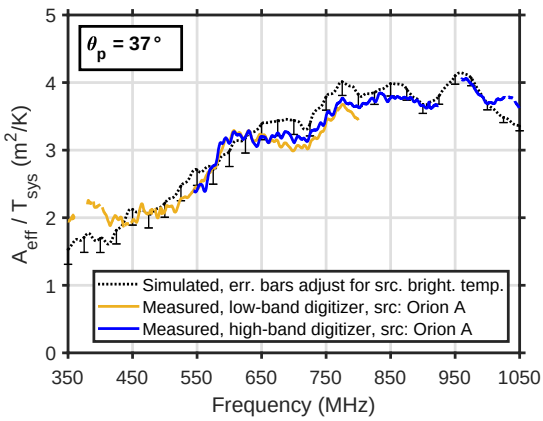

Figure 3.13: Sensitivity of the SKA Band 1 feed package; (a) Simulated in 15 m SKA and 13.5 m MeerKAT reflector; (b) Feed package installed on MeerKAT; (c) Confirmation measurements on MeerKAT [26].

realistic sky brightness model. Another correction that is applied accounts for the slightly larger aperture available in the mechanical model of the MeerKAT reflector than in the theoretical simulation model. The tiles that make up the main reflector, extend the available surface of the mechanical model, as shown in Fig. 3.13b. For the MeerKAT reflector model, this difference in size is ∼7%. In the PO+PTD simulation, the mechanical structure that holds the sub- and

main-reflector is not included, which also could affect the result. For example, back- and side-lobes from the feed could have a scattering effect at the indexer. However, the good agreement between simulation and measurement (Fig. 3.13c, and figures 6 and 7 of [26]), after the aforementioned corrections, indicate that the effect of the mechanical structure is small. To predict all possible effects, a full-wave simulation of the mechanical reflector model and the feed, can be performed.

3.5 Manufacture and tolerances

The fabrication of optimized QRFH designs is done by computer numerically controlled (CNC) machines such as a mill, lathe, water-jet or with electrostatic discharge machining (EDM). The latter used in the form of wire-cutting can achieve very accurate surfaces, specifically for the ridge profiles. With EDM, care should be taken in making sure the final surface emissivity is low enough in cryogenic application as this machining technique does not produce the bright and shiny finish as that of an end-mill. An increased surface emissivity will increase the heat load. This is discussed in Paper D where EDM is partly used. Coating the part-surfaces with material like Surtec 650 [83], or gold for smaller structures, can alleviate this issue. Tolerances in high-frequency structures should therefore account for the coating in the manufactured dimensions to not cause offsets. The emissivity is also important in the case for 3D-printed metal-structures producing grainy surfaces. The techniques of 3D-printing, selective laser sintering, or additive manufacture will be game-changers in the design of UWB-antennas in the coming years. A combined metal, and dielectric printer could produce shapes not possible in traditional machining. With traditional CNC machining, although not being the only techniques for the mechanical realization of QRFH structures, the three most common approaches are listed below. Depending on frequency, budget and QRFH structure they have different advantages. The three techniques are listed with suitable frequency ranges - low (<1 GHz), mid (∼1-20 GHz), and high (>20 GHz) - with motivation:

1. **Horn quarter sections, ridges clamped - *low-mid-high-freq***
   The horn structure is casted (molded) or milled in four quarter-pieces separated with flat surfaces in the plane of the ridges. The ridges (often planar) are milled or water-cut separately and then clamped between

adjacent sides of the quarters with bolted flanges along the horn profile [26], [27]. This approach puts strong emphasis in the manufacturing process on the orthogonality and flatness of the quarter sides, as well as the ridges to ensure proper alignment. The technique is very suitable for low-frequencies which require large and heavy horn structures that are costly to mill or machine-turn in one piece since large amounts of material must be removed. Plaster-molded quarters for frequencies below 1 GHz is a good option. If tolerances are good enough, the technique can be used in most frequency ranges. This technique is used in the manufacture of the feed design in Paper B.

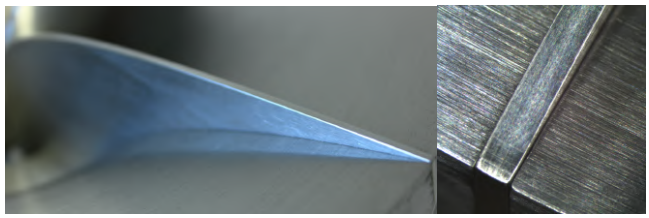

(a) **(b)**

Figure 3.14: (a) Ridge clamped between horn quarter sections; (b) Zoom-in on horn-to-ridge contact for 2 mm thick planar ridge.

2. **Machine-turned horn, bolted ridges - *mid-freq***
   The horn structure is machined in one piece in a lathe, with separately milled ridges that are attached into the horn with bolts through the horn into the back of the ridges [39], [43]. For thick ridges, with steering dowel pins in the bottom plate this technique gives adequate alignment. The technique is best suited for frequencies in the mid-range where the horn structure is not too big and heavy but also not as strict in the tolerances as high-frequency structures would be. The technique is used in the manufacture of the feed design presented in Paper E with a machine-turned pipe as the horn wall for a very low-cost assembly.

3. **Horn and ridge combined in quarter sections - *mid-high-freq***
   The horn together with ridges are milled, wire-cut, molded or printed in four solid quarter or quadrant-pieces. The separation is in the 45-degree

plane relative to the ridges which puts high tolerance requirements on the orthogonality and flatness of the quarter sides to ensure ridge-to-ridge alignment [73]. In general this will be the most expensive option as 5-axis CNC machines or special fixtures are needed and a lot of material needs to be removed. Therefore, this technique is best suited for mid-to-high frequency ranges where the size of the QRFH is smaller. This technique is used in the manufacture of the feed design presented in Paper D.

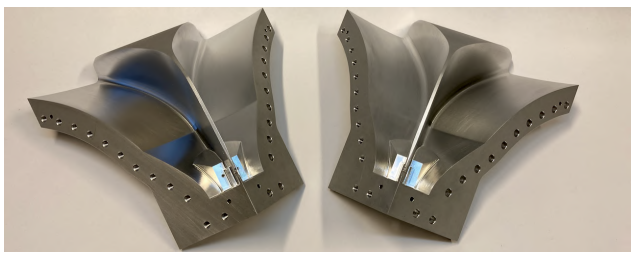

Figure 3.15: Horn and ridge machined as one part in quarter sections

The alignment and electrical contact of ridges (Fig. 3.14) is crucial in all of the methods above to mitigate unwanted mode propagation and pattern skew, impedance mismatch, and port-to-port isolation degradation. The surface currents are strongest along the ridge faces, but separation between the ridge and quarter-piece can degrade the performance if not properly contacted. It is also important to ensure a good thermal contact between ridge and horn for cryogenic application. To clamp the quarters and ridges tight, bolt spacing is typically chosen such that it is less than $\lambda/2$, preferably $\lambda/4$ if practical. For cryogenic application the use of beryllium-copper spring washers can help ensure a good continued contact after cooling. In either method, dowel pins are good practice to implement for the ridge-to-ridge alignment. Typically two pins are needed and they should be maximally separated either along the bottom of a ridge or along the length of the ridges (and quarters) depending on the method used. The single-ended excitation can be realized with a coax launch-pin inserted into a standard, commercially available SMA connector, shown in Fig. 3.17a. The launch-pin is fed through the ridge with either a surrounding dielectric or as an air-coax. In Paper D, a combination is used to reduce the length of the smaller air-line as machining difficulty and cost in-

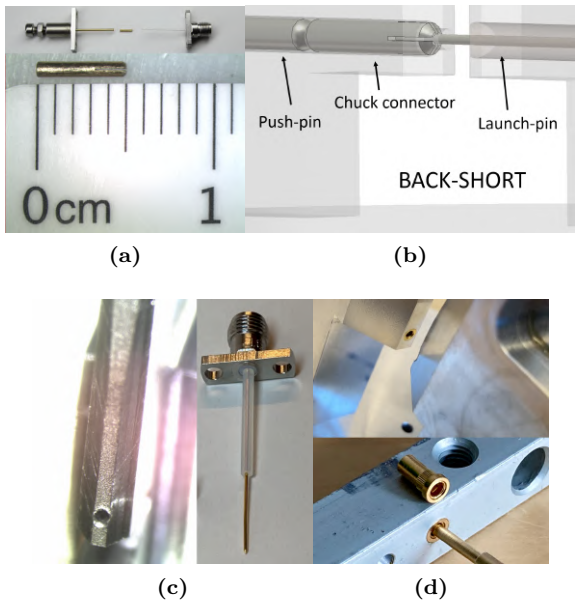

Figure 3.16: (a)-(b) Single-ended launch-pin making contact with the chuck connector in the opposite ridge; (c) Press-fit blind-hole where the launch-pin is inserted for contact; (d) Press-fit receptacles embedded in ridge for launch-pin contact.

creases for holes deeper than 10 times their diameter. The two-step approach also gives the benefit of guiding support for the dielectric for concentric alignment in the coaxial hole. This mitigates the risk of short-circuit towards the ridge or the orthogonal launch-pin. For simplicity and low cost, the launch-pin and hole dimensions can be designed so that off-the-shelf products are applicable. In Fig. 3.17b, a launch-pin made from a UT-047 semi-rigid cable is presented for a 50-Ω interface. The launch-pin with dielectric can suffer from tolerances that vary over length. The launch-pin can be contacted in the opposite ridge in a few different ways. Typically a chuck connector in the contacting ridge is a standard approach. The chuck is either threaded to contact the incoming launch-pin, or pressed from the back by a push-pin and precision-screw. In the latler case, the hole is chamfered from the inside of the

ridge so that the chuck clamps around the launch-pin when pushed towards the ridge-hole, as illustrated in Fig. 3.16b. This method is used in the feed design described in Paper B. For higher frequencies the chuck connector has been used successfully up to 24 GHz [27] Another, simpler method, is to press the

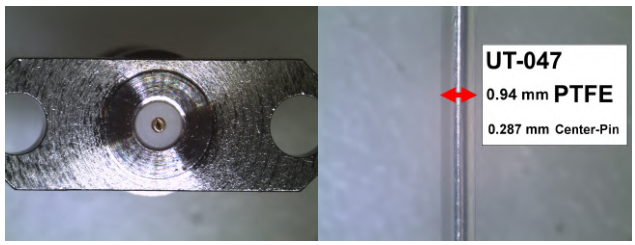

(a) **(b)**

Figure 3.17: (a) SMA connector specified up to 27 GHz with push-fit chuck; (b) semi-rigid UT-047 without outer conductor can be used as launch pin, 0.94 mm Teflon (PTFE), 0.287 mm SPCW pin.

launch-pin into a blind-hole with snug dimensions made after the launch-pins outer diameter. This method has been used successfully up to 50 GHz [73] and depending on the material and coating of the ridge, the connection can also be soldered. In Paper D this method is used with very good result and greatly simplifies assembly (Fig. 3.16c). For QRFHs with a larger ridge-face tip in the channel, gold-plated press-fit receptacles [84] are an alternative for low-cost mass-production with repetitive contact points. This method of construction is introduced in Paper E (Fig. 3.16d). For a large QRFH, the launch-pin can be contacted by screwing it in place inside the ridges. For the SKA Band 1 QRFH this method is used and the LNAs are integrated inside the ridges with direct connection to the launch-pin to mitigate loss in the room temperature system. This type of system concept is further discussed in Section 3.8. It is shown in Paper B how tolerances play a key role to impedance matching at the excitation point of the QRFH. Misalignment in the separation between ridges and the contacting-point of the launch-pin in the opposite ridge, can degrade the input reflection coefficient significantly. The port isolation is further degraded by asymmetries at the excitation point, where an acceptable measured level is often set as 35 dB. With a dielectric load in between the ridges, the combined tolerances of both the dielectric and the ridges are crucial. For any

high frequency design, a tolerance analysis performed before manufacture with focus on the excitation point and ridge-to-ridge alignment will help identify crucial design tolerances. Possible misalignment identified can simultaneously and randomly be varied over a specific range, for a set of simulations, similar to Monte-Carlo analysis [85]. This approach can predict combined effects from different misalignments, narrowing down acceptable intervals of manufactured dimensions for near-nominal performance. For mass production this is an absolute necessity to predict acceptable variations in manufactured pieces and avoid large deviations from specification without individual control of every unit.

3.6 Feed measurements

To confirm manufactured QRFH performance, typically the s-parameters are measured in a network analyzer either on open sky or against absorbers (ideally in anechoic chamber) for reduced environmental effect. For the radiation patterns, they can be characterized conveniently for most QRFHs with frequencies starting at 1 GHz in a farfield anechoic (non-echo) measurement range, illustrated in Fig. 3.18, mitigating the surrounding reflections. In such a measurement range or chamber, the device under test (DUT or AUT for "antenna under test") and the chamber probe are located in the farfield region. The farfield region is defined from the classic Fraunhofer distance of $2D_s^2/\lambda$, where D_s is the largest linear dimension of the antenna or more accurately the diameter of the smallest sphere fully enclosing the antenna. Measurements are typically done in co- and cross-polar setup according to Ludwig's 3rd definition [86] with azimuthal ϕ-cuts of minimum 15° to properly characterize the UWB-pattern's azimuthal symmetry variation [33]. Standard gain-calibration is commonly performed using standard gain horns (SGH) that are waveguide-based for specified accuracy [87]. For very large bandwidth a large number of SGHs are needed to cover the full bandwidth and can, for the sake of time, instead be done in a few representative sub-bands. In nearfield measurements, a Fourier transformation is used to turn the measured pattern into farfield allowing for a more compact chamber footprint and DUT distance, but also resulting in a more complicated and time consuming measurement. The required angular step when sampling the near-field grid decreases with increasing frequency and antenna size. Therefore, in ultra-wideband QRFH

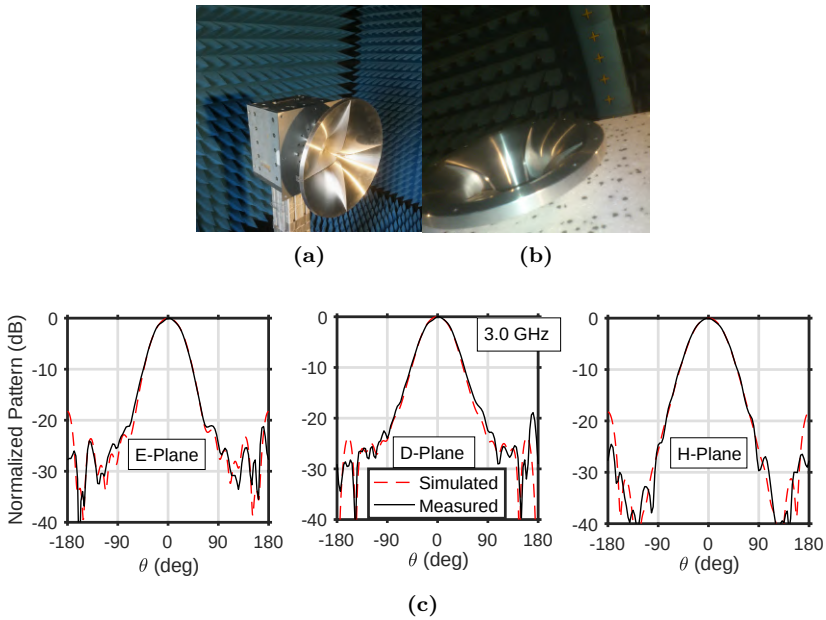

Figure 3.18: (a) QRFH in anechoic farfield chamber where the feed sweeps in azimuth; (b) QRFH in anechoic nearfield chamber with the arc containing the dual-polarized transmitting antennas; (c) Measured co-polarization beam patterns in E- (ϕ=0°), D- (ϕ=45°), and H-(ϕ=90°) plane at 3 GHz for a QRFH covering 1.5–4.5 GHz.

measurements the acquisition time needed can be very long due to the size of the antenna being of the order of the largest wavelength (lowest frequency). A trade-off approximation of practical reduced farfield distance to use can be found in [88], [89]. QRFHs for frequencies below 1 GHz are large and heavy structures which are difficult to mount in an anechoic chamber. For the SKA Band 1 frequencies 350–1050 MHz for example, the wavelengths are up to 0.85 m for the QRFH. The horn size is therefore of the order of a meter both in height and diameter (Fig. 3.1a), which makes the horn difficult to handle in a small chamber. The first confirmation of feed pattern performance was therefore performed indirectly with reflector beam pattern measurements, as presented in figure 3 of [90]. The feed was mounted in the reflector, illus-

trated in Fig. 3.10b, and the telescope main-beam was swept across a bright source (e.g. the Sun). It is important to apply appropriate corrections for efficiency, elevation deformation and source solid angle [50]. This type of measurement is a very time-consuming and demanding way of characterizing feed performance. Furthermore, it does not provide specific information on feed or reflector far-out side-lobe levels only available through accurate simulations. To be able to measure the same reflector gain that is simulated,

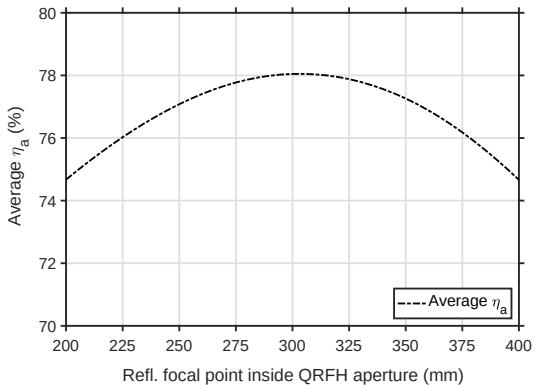

Figure 3.19: Illustration of change in aperture efficiency, η_a, depending on the feed's location relative to the reflector focal point on the optical axis.

it is important that the feed's location relative to the reflector focal point is consistent. This is due to the feed location-dependence in the phase efficiency, η_{ph}, when illuminating the reflector [58]. Aperture efficiency, η_a, can vary significantly over the band depending on η_{ph} as indicated by (2.6). In Fig. 3.19 a simulation of how aperture efficiency for a low-frequency QRFH (size: 1 m diameter) changes when the feed location is varied over a range of 200 mm along the optical axis. For a feed of higher frequency and large bandwidth, this variation is more sensitive and large efficiency deviations can be caused by misplacement of only millimeters in position. For optimal performance, the reflector focal point must coincide with the approximated feed phase center located inside the horn, in this case measured from the QRFH aperture. The best performance is found by optimizing the location in simulations, to achieve maximum phase efficiency in the upper range of the frequency band as it is more sensitive to spatial variation [48]. Then, a simple reference point

for installation can be calculated using some practical plane of reference in the mechanical assembly. As previously mentioned, in an offset system the location of the feed is also important in respect to not blocking the optical path in the reflector. This constraint is specifically important for the case of the SKA Band 1 QRFH, due to the large size of the feed.

3.7 Receiver noise temperature

During optimization the receiver noise is often modeled with an estimation from LNA noise-data and expected noise contributions from other receiver components, such as the feed losses. The modeling of radiation efficiency η_{rad} for low-loss antennas like the QRFH has been proven difficult [91] and so performance should be confirmed from receiver noise measurements. The noise introduced from a potential mismatch between the LNA and feed can introduce an uncertainty in these measurements and should be modeled and later measured. Often it is presumed low for well-designed return loss in both components. The receiver noise temperature is typically measured with the hot-cold Y-factor as a well established approach [92] that can be implemented without installing the feed on the reflector. In Y-factor tests, the power at the output of the receiver (predominantly feed and LNA) is measured in two steps. The first step is when the antenna beam is terminated in a known hot load and the second step is when it is terminated in a known cold load. The Y-factor is then given by the power ratio $Y = P_{\text{hot}}/P_{\text{cold}}$ off the two measurements (linear units). The Band 1 receiver noise was measured in a hot-cold test facility (HCTF) at DRAO, Penticton in Canada [60]. The HCTF is a large flared-out metal box with a sliding roof which is padded with absorbers on the inside, as illustrated in Fig. 3.20. The layout mitigates back- and side-lobes from the feed to hit the ground and instead terminates most of this power on sky. In such a measurement, the hot load is the absorbers' physical temperature T_{hot} and the cold load temperature T_{cold} is the sky background brightness plus any contributions from scattered power towards the ground. In such a measurement without the shielding of the ground, the uncertainties in the cold-reference are much larger. The beam-pattern of a relatively low-gain QRFH covers a broad solid angle, so T_{cold} should be calculated according to (2.13). In this case $P(\theta, \phi, \nu)$ is the power pattern of the feed pointing to zenith, simulated inside the HCTF. T_{rec} is calculated from the Y-factor

according to

$$T_{rec} = \frac{T_{\text{hot}} - T_{\text{cold}} Y}{Y - 1}. \tag{3.2}$$

In figure 2 of [90], good agreement is shown between estimated and measured receiver noise for SKA Band 1 using Y-factor tests. The agreement is presented by using both data sets to calculate the sensitivity. The typical error in the Y-factor technique should be of the order of a few percent, but can vary strongly with atmospheric variation and solar activity over the course of a day [60]. It is important to confirm T_{rec} using measurements for any type of feed-package, to find mismatches between the manufactured feed, couplers and LNAs, or unexpected resonant behavior in the receiver chain.

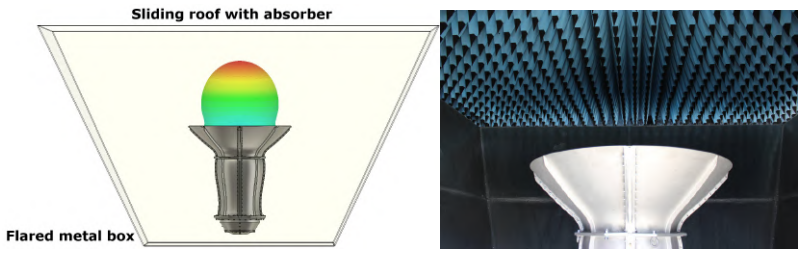

(a) **(b)**

Figure 3.20: (a) Concept of a hot-cold-test-facility (HCTF); (b) QRFH in HCTF ([60]) with the absorber roof closed for hot load reference.

3.8 Low-frequency room temperature system

For QRFHs operating below ∼1 GHz, or designs for shallow reflector configurations, the large size of the horn makes installation inside a dewar extremely difficult if not impossible. The feed can no longer be completely cryo-cooled. Instead a thermal break between the horn and dewar is needed [72], assuming the LNAs are cryogenic. The connecting cables must be long enough to reduce the thermal gradient from the warm part to the cold. The thermal break introduces a noise contribution before the LNA. The trade-off between noise and thermal load must be optimized. Ideally, the LNAs would connect directly to the launch-pin of the QRFH. However, this would introduce a more complex vacuum break with cryogenic cooling of the lower part of

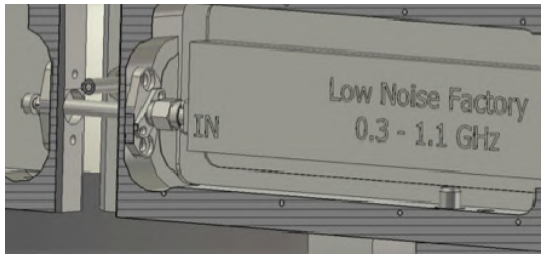

Figure 3.21: Integration of LNA directly inside QRFH ridge [26].

the feed. This technique has though been successfully implemented by other types of feed systems [80]. Another approach is use room temperature LNAs which today can achieve low noise temperature at low frequencies [7], [13]. If the ridges are thick enough, the LNAs can be integrated directly inside the metallic structure and connected to the launch-pin mitigating additional losses. As alluded to earlier, this approach is successfully implemented for the SKA Band 1 QRFH, as shown in Fig 3.21 ([26]). The noise injection is built into the room temperature LNAs which were provided by Low Noise Factory (LNF), Gothenburg, Sweden. Compared to the previously proposed cryogenic design with a thermal break, the final receiver noise temperature is similar (figure 15 in [80]). The room temperature system has obvious advantages in reduced cost, complexity, and maintenance demand. There is also no need for a cryostat which reduces power consumption for the receiver package dramatically.

CHAPTER 4

Dielectric loading of the Quad-ridge Flared Horn

In this chapter we introduce the concept of dielectrically loading the Quad-ridge Flared Horn to improve beamwidth control over wide frequency and reduce cross-polarization. A brief overview is given of the QRFH wideband performance when dielectrically loading the horn, with considerations for both cryogenic and room temperature applications. We also discuss the importance of keeping the QRFH footprint compact, and robust to maintain its usability.

4.1 QRFH with dielectric load

Impedance matching for the QRFH has been performed successfully for more than 10:1 bandwidth [93], but the decrease in pattern beamwidth lowers the performance in the upper frequency range to poor and unstable levels. The narrowing of the beamwidth, most notably in the H-plane, results in reduced aperture efficiency (Fig. 1.10), and increased cross-polarization. An approach to improve the beamwidth control over wideband design, is to add dielectric material into the QRFH structure, as illustrated in Fig. 4.1. The dielectric material increases permittivity along the center of the horn and in-between the ridge-faces where the current density is concentrated. The result is a

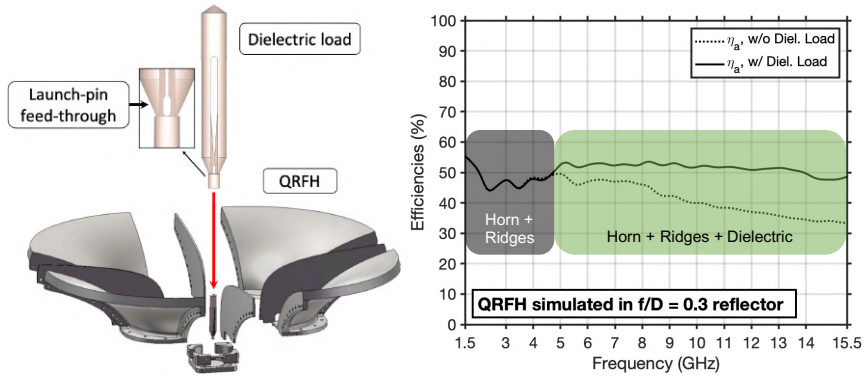

Figure 4.1: The reduction of aperture efficiency over frequency normally seen in QRFHs (Fig. 1.10) is mitigated with dielectric. Dielectric loading of the QRFH mostly affects the upper part of the frequency band.

widened radiation pattern over the upper part of frequency range. This has been explored in several forms, from lenses [46], [47] to more complex multi-layer spear-type structures [48]. In [48], a three-layered dielectric load was designed together with the differential-fed QRFH. The design also included a choke-skirt attached to the aperture for improved low-frequency performance. The result for the 6:1 bandwidth is nearly-symmetric beam patterns in E-, D- and H-plane and very low cross-polarization over 0.7-4.2 GHz. The aperture efficiency is on average 65% for f/D=0.41 and the input reflection coefficient less than -14 dB across the band. However, the complexity of such a QRFH design is considerable in terms of manufacture, cost and assembly. To achieve a feed suitable for cooling to cryogenic temperatures, the shrinkage of the different materials must be accounted for to avoid severe skewing in the dielectric. A large dielectric load can have a significant thermal gradient across the structure [49] potentially increasing losses and misalignment. Measurements indicate that for such a design, feed loss at ∼4 GHz is nearly 2 times that of the LNA contribution [94]. For higher frequencies the dimensions would be smaller and such a complex structure can be hard to realize without expensive manufacture to strict tolerances.

Dielectric load - compact footprint

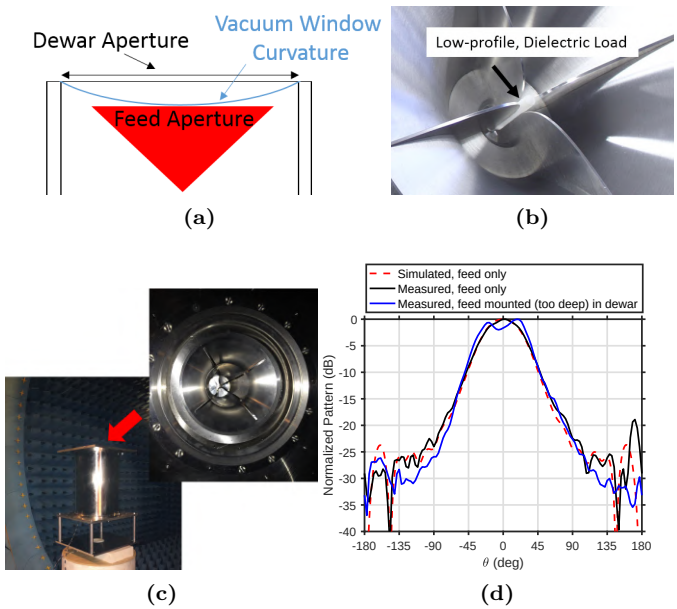

Figure 4.2: (a) Dewar vacuum window curvature; (b) Low-profile, dielectric load in QRFH; (c) Test dewar for 3:1 non-dielectric QRFH, shown without vacuum window. (d) Measured pattern at center frequency, 3 GHz, beam-splitting effect when the feed is mounted too deep in the dewar.

To not jeopardize the QRFH's practical function as the first component in the receiver chains of today and tomorrow, its footprint should be kept simple, robust, compact, and as low-loss as possible. In this thesis a simple and homogeneous dielectric load is proposed for beyond decade bandwidth in QRFHs. Unlike [46]–[48], the dielectric loads proposed in Papers A-D have a compact design ($\leq$80 mm length, $\leq$ 8.2 mm diameter) with no addition to the QRFH aperture footprint. It is based on a simple structure built on cone-cylinder-cone layout, but can also be defined with an analytic function, as in Paper D, or spline-defined profile depending on need. The dielectric load is installed in the center of the QRFH, towards the bottom with clearance to the aperture, as shown in Fig. 4.1a. The excitation can easily be kept single-ended by feed-

ing the launch-pins through a machined hole in the dielectric load, see Fig 4.1. The dielectric can be fastened in different ways, this is explored in Paper B by locking it in the backshort, and in Paper D using fasteners for installation and replacement without disassembly of the rest of the QRFH structure. This type of insert is machinable with standard numerical controlled milling and turning, in dry or mixed-coolant processes. Care must be taken for the material expansion when machined, so that tolerances are not jeopardized or skewed. There are many suitable dielectric materials, predominantly polymers, that can be machined, some of them listed in Table 4.1. All these features, makes the compact dielectric attractive for large scale production in terms of cost and assembly. By clamping the dielectric load between ridges of the QRFH, thermal contact is made, reducing the risk of large temperature gradients in a cryogenic environment. Clamping also prevents the dielectric from sliding out or wobbling when the telescope is in motion. Typically for cryogenic dewars of metal-cylinder type, a vacuum window of multi-layer Mylar or similar material is used. Due to the pressure difference of the vacuum, inwards-curvature of the window needs to be allowed for requiring a certain spacing to the feed aperture, as illustrated in Fig. 4.2a. The clearance between feed and dewar should be kept short in the type of wide beamwidth applications the QRFH is often used for. If the necessary clearance between the feed and the dewar aperture is too large, unwanted resonant affects or beam-splitting can occur. This is exemplified for a non-dielectric 3:1 bandwidth QRFH when mounted too deep in a test dewar, shown in Fig. 4.2c with the effect on the feed pattern shown in Fig. 4.2d. The beam-splitting effect shown here at the center of the band, is even more evident at the lower frequencies of the band. This can reduce the radiation properties and noise temperature performance of the system in the intended reflector. The alternative to enlarge the dewar window is a trade-off with increased infrared (IR) radiation as the penalty. An increased IR load in the dewar leads to an increased power consumption. For the very large reflector arrays of ngVLA [29] and SKA [23], an important requirement is the power consumption and a larger window may therefore not be an option. If a large vacuum window is acceptable, the QRFH can be filled with $\epsilon_r \sim 1$ styrofoam material to support the vacuum-window and reduce the inwards curvature. Such a support is more easily incorporated in the QRFH if the dielectric footprint is small.

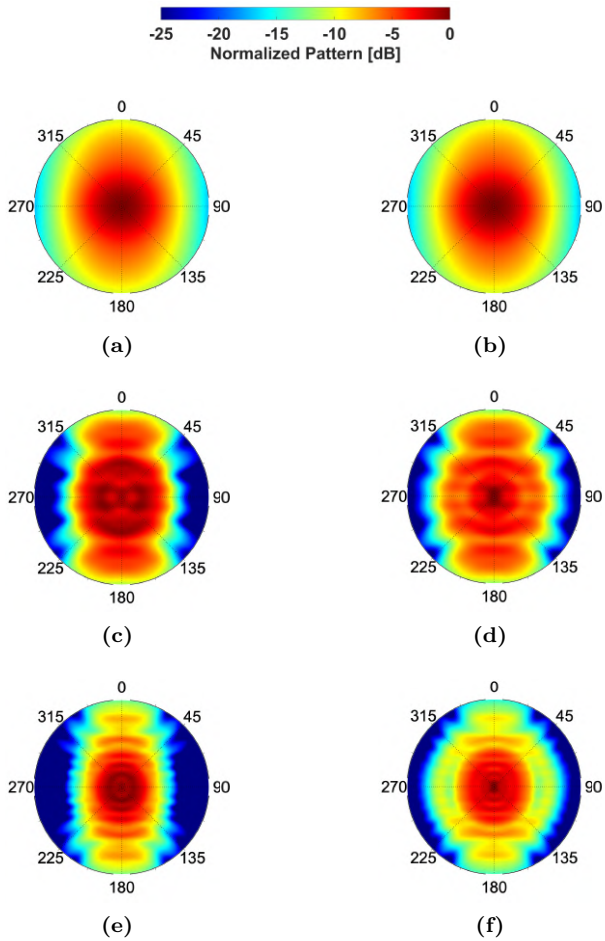

Figure 4.3: Polar plot ϕ=[0°, 360°] QRFH radiation pattern: without dielectric (left), and with dielectric (right); (a)-(b) 1.5 GHz; (c)-(d) 8.5 GHz; (e)-(f) 15.5 GHz; Circular edge represents reflector rim at θ_e=80°, in f/D=0.3. E-plane, ϕ=0°, D-plane, ϕ=45°, H-plane, ϕ=90°

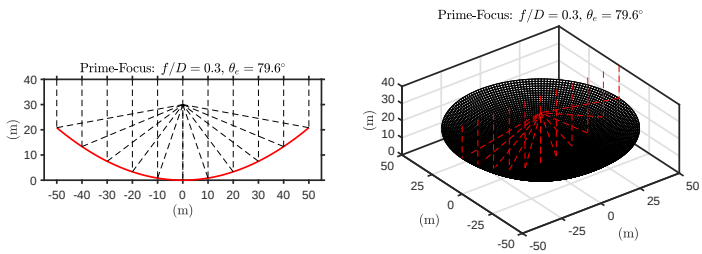

(a) **(b)**

Figure 4.4: f/D=0.3 for the Effelsberg 100 m telescope in prime-focus, θ_e=79.6°. (a) Cross-section view; (b) Perspective view.

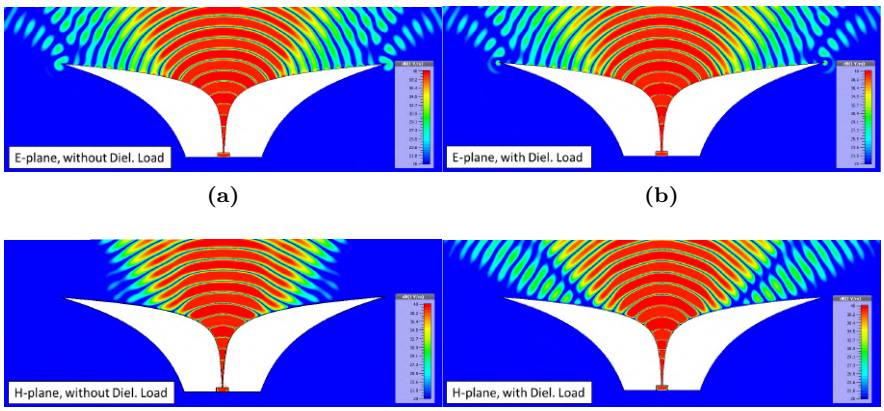

(a) **(b)**

(c) **(d)**

Figure 4.5: Intensity for the co-polarized component of the E-field at 15 GHz. (a) E-plane, without dielectric load; (b) E-plane, with dielectric load; (c) H-plane, without dielectric load; (d) H-plane, with dielectric load.

4.2 Wide beamwidth for deep reflectors

Most QRFHs being used in radio telescopes today, are designed for f/D ratios between 0.4 and 0.5 in dual-reflector configuration. It was pointed out on

pp. 79 in [40] that more work needs to be done for deeper reflectors. In Fig. 4.4 the deep (f/D=0.3) axially-symmetric prime-focus of the Effelsberg 100 m reflector telescope is illustrated with a simplified model. The corresponding half-subtended angle is $\theta_e \approx 80°$, which is a challenging beamwidth to illuminate with an UWB feed. Typically this configuration would use a choke-type horn that can achieve wide beamwidth over octave frequency range. For QRFHs, the beamwidth is challenging with a large flaring angle required, with the low-frequency part of the band suffering from reduced spill-over efficiency. For a prime-focus application this is more severe as the feed is pointing towards the ground. For a large reflector a higher spill-over level can still be acceptable in a wideband application, if good aperture efficiency is achieved over the entire bandwidth to utilize the available area. For an extremely large reflector such as the Effelsberg 100 m dish, the physical available area is more than 40 times that of a 15 m reflector such as the SKA dish. In [40] a proposed QRFH for f/D=0.3 over 4:1 bandwidth has a predicted aperture efficiency of 40-45%. The 7:1 QRFH proposed in the same reference has a minimum η_{a}=35%. In Paper B the expected aperture efficiency of the dielectrically loaded QRFH is above 50% in band-average with a minimum of 44% over 10:1 bandwidth in the same f/D=0.3. The reason is the improved beamwidth and therefore improved edge taper in the upper frequency range due to the dielectric load. In Fig. 4.3 this is illustrated with a polar plot for different frequencies showing the taper from the feed from center of the reflector towards the edge of θ_{e}=80° (circular rim). The dielectric load (right-side plots) has a broadening effect on the beam for mid and upper frequency range, particularly in H-plane. This is further confirmed by looking at the simulated intensity in a cross-section of the E–field component along the co-polarization axis in E- and H-plane, shown for 15 GHz in Fig. 4.5. There is almost no effect in E-plane in this case (see Fig. 4.5b), but in H-plane the radiation is spread at a wider angle when the dielectric load is installed (see Fig. 4.5d). The improved pattern results in better illumination, azimuth mode, and phase efficiency in the reflector at mid and upper frequencies. In Paper B, it is shown that the suggested approach of dielectrically loading the QRFH improves phase efficiency to a high ($>$ 96 % band-average), near-constant, level over decade bandwidth. The performance at the lower frequency range is mostly determined by the QRFH's metallic structure, highlighted in Fig. 4.1. The cross-polarization is also improved for mid and upper frequencies by the dielectric load as the E- and H-plane pat-

tern's difference is reduced. The feed's polarization purity on the reflector is represented by the intrinsic cross-polarization ratio (IXR) [63]. For the SKA, minimum IXR should be better than 15 dB within HPBW and dielectrically loaded QRFHs can fulfill this over extremely wide frequency bands, further detailed in Paper B and D, and in Section 4.2.

Design for "Small-D-Big-N"

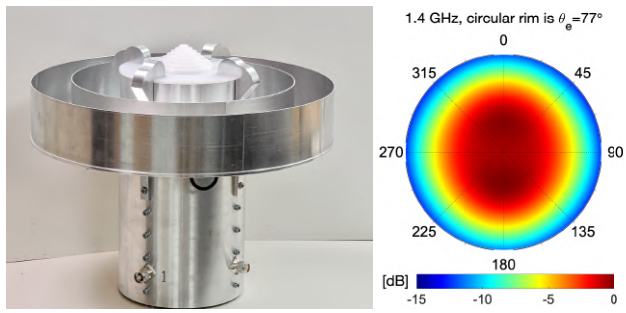

(a) **(b)**

Figure 4.6: (a) The quad-ridge choke horn (QRCH) with a dielectric load in the form of a HDPE-lid improving (b) beamwidth while shielding the inside of the horn to the environment, detailed in Paper E.

The feed development for the large-reflector arrays of SKA and ngVLA are predominantly done for cryogenic receiver applications, with the room temperature system of SKA Band 1 being an exception [25]. The development of competitive room temperature low-noise amplifiers (LNAs) [7], [13], enables not only a simplified and less-expensive receiver solution for large-reflector arrays, but also the possibility to move away from the expensive large reflector itself. The concept of "Small-D-Big-N" is based on low-cost and compact reflector units with room temperature receivers, instead of the bulky and maintenance-heavy cryogenic dewars, and has been proposed for several upcoming projects [21], [95]. The previously introduced Deep Synoptic Array (DSA-2000) is such a project to realize an array of 2000×5 m reflectors, where each reflector is equipped with a room temperature feed package including first-stage LNAs. The frequency ranges of interest is 0.7 to

2 GHz, with the detection and location of fast radio bursts and pulsar timing as the primary applications. The survey speed and sensitivity will outperform that of large-dish arrays over the same frequency range (Fig. 1.7). To mitigate spillover and de-focusing effects, the f/D is chosen to be less than 0.35 (deep reflector) which is normally applicable to choke-type horns [13], [14] and where the QRFH suffers from under-illumination. Furthermore, the size of the feed aperture introduces an important trade-off in blockage of the small reflector aperture over the frequency-range in question. Paper E describes a new concept of a Quad-ridge Choke Horn (QRCH) with dielectric load as a wideband feed over 2.85:1 bandwidth optimized for this type of array concept. The QRCH combines wide beamwidth properties of the choke horn with the broadband properties of the QRFH, while maintaining a compact feed diameter for low blockage. The prototype developed for the DSA-2000 is designed with a low-cost and low-complexity mindset for large scale unit production. The dielectric load is crucial to the wide beamwidth in the upper part of the frequency band and the choke-rings dominate the low-frequency pattern performance. The low-loss dielectric load is realized in the form of a lid further acting as an environmental shield to the inner workings of the horn. To further improve the sensitivity, a shielding concept of the reflector itself has been explored that minimizes the spill-over pick-up from ground. Together with excellent progress in the development of a wideband version of the previously reported room temperature LNAs for DSA-110 [13], the predicted system noise for the QRCH feed package in DSA-2000 is on the order of 25 K.

Dielectric load - decade bandwidth and beyond

The widening effect of the dielectric is continuous over frequency as exemplified in Fig. 4.7 for the feed covering 1.5–15.5 GHz in Paper B. Dielectric loading can further extend the QRFH performance beyond decade bandwidth as shown in Paper D and further increase its useability in radio astronomy applications. The 20:1 bandwidth QRFH proposed can cover SKA Band 2 through Band 5 and beyond, with one single feed for 1-20 GHz. For the development of large interferometric arrays this is a low-cost option removing the need for multiple octave-receiver systems. Simulated aperture efficiency in Fig. 4.8a illustrates the potential of such a system in an unshaped f/D=0.433 prime-focus reflector with band-average η_{a}=62 % and η_{a}=72 % in the shaped

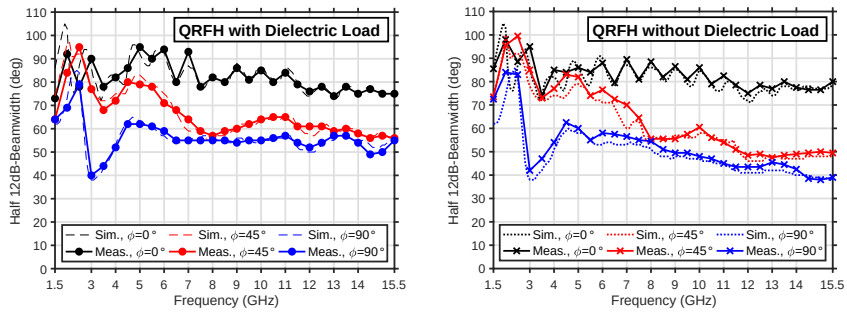

(a) **(b)**

Figure 4.7: QRFH beamwidth over 10:1 frequency band improved (a) with dielectric load compared to (b) without.

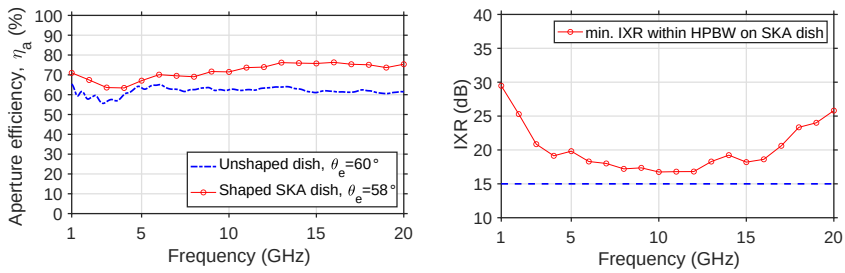

(a) **(b)**

Figure 4.8: Dielectrically loading the QRFH enables consistent performance beyond decade bandwidth. Simulated (a) aperture efficiency, and (b) IXR for 20:1 bandwidth (15 dB is the SKA minimum limit).

SKA dish with similar half-subtended angle. The average aperture efficiency for the dielectrically loaded QRFH in the unshaped reflector is comparable to that of the smaller 6:1 bandwidth of a non-dielectric QRFH in similar f/D [40], but with a stable efficiency-level across the much larger 20:1 bandwidth due to the dielectric. The dielectrically loaded QRFH also clearly fulfills the 15 dB IXR minimum-limit of the SKA, as seen in Fig. 4.8b, showing that

also cross-polarization is on a competitive level. Due to the adaptability of the QRFH and the simple dielectric structure, such a feed could be specifically optimized for both SKA [56], and ngVLA [30] reflectors further tailoring its performance while taking advantage of their spill-over shielded optics for high-sensitivity performance.

Dielectrically loaded QRFH compared with log-periodic feed

(a) **(b)**

Figure 4.9: QRFH with dielectric load in Paper D, installed in (a) glass-dewar mounted in one of the (b) ATA reflectors for tests.

The ultra-wideband dielectrically loaded QRFH presented in Paper D with 20:1 bandwidth is currently under test on one of the reflector arrays with ground-shield, the Allen Telescope Array (ATA). Examples of noise measurements of the receiver, and test-detection of the bright pulsar B0329+54 (or J0332+5434) with wideband frequency response [15] are presented here. Pulsars are rotating neutron stars that emit directed radiation along a light-cone and when observed this appears to be a pulsed pattern in a specific direction. Figure 4.10a and Fig. 4.10b presents the pulse profile of J0332+5434 as detected with the dielectrically loaded QRFH and the current log-periodic Antonio feed respectively. Plots are from 10 minutes of recorded data where 20 available antennas at the ATA were used with the digital signal processing backend frequency-centered at 1.5 GHz with an effective bandwidth of 672 MHz. In Fig. 4.10c, hot-cold Y-factor measurement results (3.2) of the receiver noise temperature are presented for the two different feeds as well.

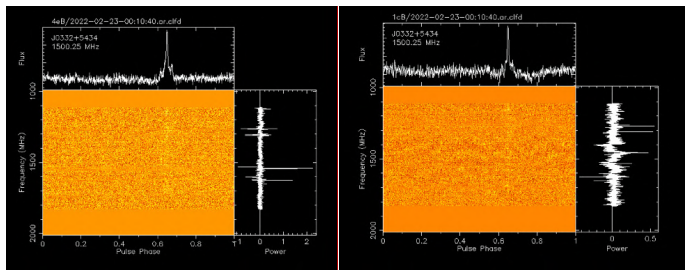

(a) **(b)**

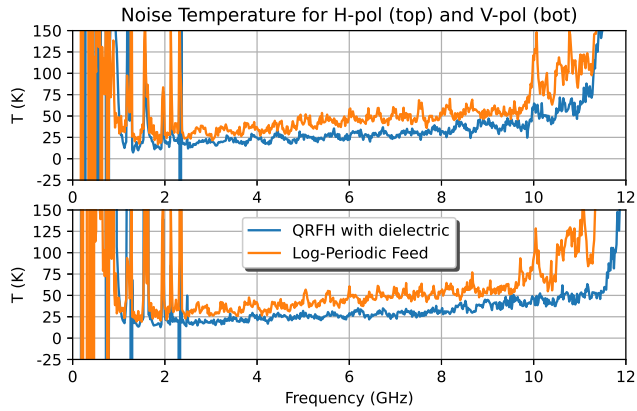

(c)

Figure 4.10: Pulsar detection-test (J0332+5434) on the ATA using (a) Dielectrically loaded QRFH in Paper D, and (b) log-periodic feed. (c) Receiver noise temperature from Y-factor measurements. Bandwidth limited by post amplifier transmitter to ∼11 GHz.

The noise tests presented here are limited by the post amplifier transmitter (PAX) to approximately 11.2 GHz. Measurements up to 15 GHz are presented in Paper D, limited by the functional bandwidth of the LNAs. The prototype QRFH has been cooled to cryogenic temperature of 100 K, and then warmed back up to room temperature three and two times respectively to this date, with highly repeatable results for the low-noise measurements

showing the usability of the concept. Tests of pointing, and long-term stability is forthcoming and will bring further understanding of performance over extreme bandwidth and the requirements needed for further development.

4.3 Wideband dielectric material data

The dielectric properties of a material is for engineering purposes often characterized by the components of its complex dielectric permittivity

$$\hat{\epsilon} = \epsilon' - i\epsilon'' \tag{4.1}$$

where the real part is $\epsilon'=\epsilon_r\epsilon_0$. The unit-less, ϵ_r, is often called the relative permittivity or dielectric constant and $\epsilon_0 \approx 8.854 \cdot 10^{-12}$ [F/m] the vacuum permittivity. Therefore, per definition the dielectric constant for vacuum is $\epsilon_r=1$ (for air $\epsilon_r=1.0006$). The imaginary part of (4.1) characterizes the losses in the material, normally expressed as the loss tangent

$$\tan\delta = \frac{\epsilon''}{\epsilon'}. \tag{4.2}$$

The suitable ϵ_r to use and shape of the dielectric load is found in optimization together with the QRFH structure for best radiation and impedance performance. For a homogeneous dielectric load, a material with corresponding ϵ_r or in close proximity to what is found in optimization can then be used for realization. For the dielectric in Paper B, PTFE with $\epsilon_r=2.1$ is selected for its low-loss properties, while in Paper D the ϵ_r has to be larger for the full 20:1 bandwidth. Therefore, polyimide with good cryogenic properties is explored. The material is tested in cryogenic environment by submerging it in liquid nitrogen (T=77 K, Fig. 4.11a) and then performing mechanical stress tests, and shrinkage estimation to account for in the design performance. The loss-contribution of the insert to the overall feed loss, depends on the design, frequency, temperature, and the aforementioned material loss tangent. High-density polyethylene has a stable relative permittivity of $\epsilon_r=2.35$, and loss tangent $\tan\delta=0.0001$. Broadband measurements show good stability of these values up to 50 GHz [96]. Due to the low loss tangent, the HDPE material is suitable for room temperature application, and is explored in Paper E with only a small penalty to the total feed loss. The availability of *wideband* dielectric material data from suppliers of common polymers is surprisingly poor,

(a) (b)

Figure 4.11: (a) Sample of dielectric (polyimide) in Liquid Nitrogen (77 K); (b) Samples of HDPE in TRL setup for dielectric characterization.

especially above 1 GHz. For ultra-wideband design the general lack of dielectric property data over frequency is a clear challenge. Typically the material is assumed to be near-constant in performance over frequency. Since specific brands of the same polymer-type can behave differently, vary over frequency and with material density ([97]), the most appropriate way to choose material with the desired electrical properties is to test samples over the frequencies of interest. The real part of (4.1) can be measured in different ways with good accuracy, for example with a thru-line-reflect (Fig. 4.11b) setup and Nicolson-Ross-Weir (NRW) algorithm [98], [99]. However, to calculate the loss tangent the measured accuracy needed is not as straightforward to achieve for low-loss polymers [96]. Measurements are a very time consuming process, and sometimes not possible especially over ultra-wideband frequency ranges. In Table 4.1 machinable dielectric materials are listed, mostly polymers, with reported ϵ_r in the range of 2.1-3.8 suitable for the frequency ranges and applications investigated in this thesis. The loss tangents for the listed materials vary in usability for low-loss applications, where some may only be used for prototyping of dielectric structures. For low-frequency application, a loss tangent value of the order of 10^{-4} is suitable for room temperature applications. For cryogenic use within the frequency range of tens of gigahertz, the span of allowable loss tangent value is larger, but noise increases rapidly when the value significantly exceeds 10^{-3}.

Table 4.1: Dielectric materials suitable for machining. Properties are normally frequency and temperature dependent. An excellent source of dielectric material data for mm-frequencies is [100].

Material properties	f[GHz]	ϵ_r	tanδ 10^{-3}	Ref.
Polytetrafluoroethylene (PTFE)	11.5	2.1-2.05	0.1-0.7	[96], [101]
Polyethylene (PE)				
- HDPE/PE-HD (Generic)	11.3	2.35	0.1	[96], [101]
Polystyrene (PS)				
- REXOLITE 1422	10	2.53	0.66	[102]
- Eccostock HIK K=3.5	10	3.5	2.0	[103]
Polymethylmethacrylate (PMMA)				
- Acrylic (Generic)	11	2.6	8	[101]
Polyphenylene Ether (PPE)				
- PREPERM PPE260	2.4	2.6	0.9	[104]
- PREPERM PPE350	22	3.5	2.4	[105]
Polyether-ether-ketone (PEEK)	0.001	3.3	3.0	[106]
Polyimide (PI, unfilled)				
- Ensinger TECASINT 2011	0.0001	3.4	1.0*	[107]
- DuPont Vespel SP1	0.001	3.55	3.4	[108]
Polyoxymethylene (POM)	10	3.6	30	[109]
Fused Quartz**	30	3.81	0.4	[110]

*From the similar stock TECASINT 4011 datasheet. **The machinability of Fused Quartz has not been explored by the author, but was successfully manufactured in [48].

CHAPTER 5

Contributions and Future Work

The dielectric loading of QRFHs is an approach with large potential and yet far, few documented examples of implemented designs used in practice. The work presented in this thesis and appended papers, further contributes to the understanding of the potential of this concept. A compact, homogeneous low-loss dielectric insert in the QRFH design can offer ultra-wideband performance with improved radiation properties and impedance matching up to 20:1 bandwidth. The example designs presented in this thesis and the appended papers, strengthen the case for dielectrically loaded QRFHs as a critical technology for future radio telescope design. A summary of the properties of these designs are listed in Table 5.1 together with other QRFH designs with dielectric load of some form. With the emergence of shaped reflectors and shielding, interesting progress is currently being made towards dielectrically loaded QRFHs for very high sensitivity performance in cryogenic applications, potentially changing the typical wideband vs narrowband trade-off for radio astronomy. Several radio astronomical projects around the world are currently exploring QRFH with dielectric load. Low-loss dielectric loading has also shown applicability for feed designs in low-frequency room temperature systems of small-diameter reflector arrays (Small-D-Big-N), such as the design proposed for the DSA-

2000. Once 3D-printing technology achieves high enough accuracy combined with low cost for the most common dielectrics and metal, any potential shape can be realized. With combined printing of metal and dielectric, it is feasible to think of future mass-produced low-cost single-feed packages combined with compact reflector units, covering large parts of the radio spectrum as an array concept. With further advancement in room temperature LNAs, integrated feed and LNA packages should also be further explored.

Table 5.1: Performance characteristics of some wideband quad-ridge based horns with dielectric load, insert, spear or lens-type configuration. Data is compiled from published results, extrapolated from available figures and tables, estimated band-averages are presented.

Design	Bandwidth	Frequency	η_a	S_{11}	Dielectric
Dunning [48], [49], [94]	6 : 1	0.7-4.2 GHz	65 % in f/D=0.41	-20 dB	Fused Quartz/PTFE, 3-layer**
Flygare [Paper A-C]	10.3 : 1	1.5-15.5 GHz	50 % in f/D=0.3	-9.4 dB	PTFE, Homogeneous
Flygare [Paper D]	20 : 1	1-20 GHz	62 % in f/D=0.433	-13.6 dB	Polyimide, Homogeneous
Flygare [Paper E]	2.85 : 1	0.7-2 GHz	66 % in f/D=0.315	-15.1 dB	HDPE, Homogeneous
Lai [46]*	≈10:1	??	50 % in f/D= ?	-17 dB	??, Homogeneous (?)
Bauerle [47]*	3 : 1	5-15 GHz	70 % in f/D= ?	-15 dB	C-Stock Low-34, Homogeneous

*The author cannot deduce information on f/D and reflector application in these published result, and a frequency range. They are also lacking in wideband performance data, and tabulated data is taken from the frequency samples presented. They are included as additional references on previous work in QRFHs with dielectrics. **The third layer is in the form of machined grooves in the outside of the intermediate PTFE layer.

Future work

With the introduction of dielectric loading of QRFHs, or for that matter Vivaldi- and choke-horns, improved feed designs for future receiver systems are wide-open to explore. Specifically for the QRFH some future work could include:

- Further practical evaluation of dielectric QRFHs in receivers. Effect of thermal variations over time on the small dielectric components, including potential warping or skewing of the structure, should be monitored and evaluated over continued cycling. How the telescope pointing-model over ultra-wideband frequency range is affected is important.

- Modal analysis, and phase errors in aperture-mode content of higher-order modes for the QRFH with dielectric insert. This can increase the understanding of the best design approach for both the differential-fed, and single-ended QRFH.
- Investigation of the minimum degrees of freedom needed for beamwidth control over specific frequency bandwidths, including ridge and horn profiles, and dielectric.
- Compiling dielectric material databases over the frequency ranges of interest, both cryogenic and room temperature. Inclduing the effect of machining material and the potential changes in dielectric and mechanical properties due to this (e.g. milling vs 3D-printing).
- Studying dielectric multilayers with compact footprints where effective dielectric constants can be constructed with grooves or holes in homogeneous materials that alleviate some of the issues caused by different thermal shrinkage/expansion coefficients in a multilayer structure.
- Exploring adding dielectric loads to existing QRFH designs without altering footprint (e.g. SKA Band B, VGOS-systems). The designs in this paper have been optimized with all the degrees of freedom of the QRFH and dielectric available from the start. To what extent existing QRFH designs can be improved in radiation performance in the upper frequency-range by adding dielectric loads or inserts, is an interesting topic.
- Further combinations of choke-rings, ridges and dielectric loads for decade-bandwidth applications where the expanded footprint is appropriate. Combined dewar and feed-design is an interesting subtopic to explore.
- Combining room temperature QRFH and LNA packages, together with small-diameter reflector units designed for wide bandwidth as part of either a Small-D-Big-N array or as far-out remote stations monitoring the sky for events. Such units could be solar-powered and satellite-connected, assuming appropriate self-shielding and filtering, for low maintenance and low cost.

Below follows a brief summary of the included papers:

5.1 Paper A

Jonas Flygare, Miroslav Pantaleev, and Simon Olvhammar
BRAND: Ultra-wideband feed development for the European VLBI network - A dielectrically loaded decade bandwidth quad-ridge flared horn
in *Proceedings of the 12th European Conference on Antennas and Propagation (EuCAP)*, London, UK, Apr. 2018.
 DOI: 10.1049/cp.2018.0817 .

In this paper, preliminary simulation results of dielectrically loading the QRFH shows the potential to cover decade bandwidth. A compact homogeneous PTFE dielectric load inserted at the center of the QRFH is proposed for 1.5-15.5 GHz bandwidth. The dielectric load improves beamwidth stability in the upper frequency range. The analytic-spline-hybrid (ASH) concept is introduced.

My contributions: *Electromagnetic design, simulation, analysis, and I wrote the paper.*

5.2 Paper B

Jonas Flygare and Miroslav Pantaleev
Dielectrically Loaded Quad-Ridge Flared Horn for Beamwidth Control Over Decade Bandwidth - Optimization, Manufacture, and Measurement
in *IEEE Transactions on Antennas and Propagation*, vol. 68, no. 1, pp. 207–216, Jan. 2020
 10.1109/TAP.2019.2940529 .

In this paper, we present a dielectrically loaded QRFH designed, manufactured and tested over 1.5-15.5 GHz. The 10.3:1 bandwidth has stable beamwidth due to the introduction of a compact, low-loss, and homogeneous dielectric load made from PTFE. The feed is designed for the BRoad-bAND (BRAND) project within EU Horizon2020 with the first prototype made for

the prime-focus of the Effelsberg 100 m telescope with f/D=0.3. The feed has a simulated band-average aperture efficiency of 50 % in this reflector geometry, and measured input-reflection band-average of -9.4 dB over the design band. Simulated and measured feed patterns agree, and a tolerance analysis of the excitation point explains the deviation from nominal performance in the input-reflection and acceptable tolerance intervals for future fabrication.

My contributions: *Electromagnetic design, simulation, analysis, mechanical assembly, feed measurements, and I wrote the paper.*

5.3 Paper C

Jonas Flygare and Jian Yang
Strategy and Overview for Development of Beyond-Decade-Bandwidth Quad-ridge Flared Horns for Radio Astronomy
in *Proceedings of the 15th European Conference on Antennas and Propagation (EuCAP)*, Dusseldorf, Germany, Mar. 2021.
 DOI: 10.23919/EuCAP51087.2021.9410964 .

In this paper, analysis of the feed pattern evolution of an existing decade bandwidth QRFH with dielectric load is presented. Analysis of the feed is done beyond its design frequency range 1.5-15.5 GHz up to 18 GHz where it still functions with a reduced aperture efficiency of 40 %. The importance of the feed pattern evolution for extended bandwidth in ultra-wideband design is put into context of reflector illumination by analyzing the sub-efficiencies of the aperture efficiency for the feed in f/D=0.3 reflector.

My contributions: *Electromagnetic design, simulation, analysis, and I wrote the paper.*

5.4 Paper D

Jonas Flygare, Jian Yang, Alexander W. Pollak, Robert E. J. Watkins, Fiona Hillier, Leif Helldner, and Sven-Erik Ferm
Beyond-decade Ultra-wideband Quad-ridge Flared Horn with Dielectric Load for Beamwidth Stability over 1-20 GHz

Submitted to IEEE Transactions on Antennas and Propagation .

In this paper, we present the design, manufacture, and measurement of a dielectrically loaded QRFH with dual-linear polarization over 1-20 GHz. The unprecedented 20:1 fractional bandwidth is made possible with a compact dielectric load made from homogeneous polyimide, a space-graded polymer for cryogenic application. The feed is predicted to achieve 62 % band-average aperture efficiency in a reflector with 60-degree half-subtended angle. Measured input reflection is better than -13 dB in band-average with single-ended excitation. The feed is fabricated in four quarters with the ridge implementing analytic-spline-hybrid profiles with 3D-cubic splines for improved cross-polarization in the low-frequency range. The feed is tested with cryogenic LNAs on the Allen Telescope Array in Hat Creek, California, USA with good agreement to predicted system noise temperature. This feed offers an alternative approach to cover 1-20 GHz with one feed package for the large-reflector arrays of today and tomorrow.

My contributions: *Electromagnetic design, simulation, analysis, mechanical design, drawings, assembly, feed measurements, and I wrote the paper.*

5.5 Paper E

Jonas Flygare, Sander Weinreb, and David P. Woody
Quad-ridge Choke Horn with Dielectric Load as a Wideband Feed for Non-cryogenic Reflector Arrays in Radio Astronomy
Submitted to IEEE Transactions on Antennas and Propagation .

In this paper, we introduce the Quad-ridge Choke Horn (QRCH) with dielectric load as a compact low-frequency feed for non-cryogenic small-diameter reflector arrays. A homogeneous low-loss dielectric lid made from HDPE is used to achieve wide beamwidth across 0.7-2 GHz for low f/D reflectors. The feed is developed for the Deep Synoptic Array (DSA-2000), and achieves 66 % aperture efficiency, including blockage, in a 5 m prime-focus reflector. The measured band-average input reflection is better than -15 dB for the dual-linear polarized feed with single-ended excitation. We explore a reflector-shield to reduce spill-over noise to very low levels. Together with preliminary data from room temperature low-noise amplifier development for the DSA-

2000, system noise temperature is predicted to be 25 K. The feed fabrication is focused on low-cost units in mass-production for 2000 reflectors.

My contributions: *Electromagnetic design, simulation, analysis, mechanical design, drawings, assembly, feed measurements, and I wrote the paper.*

References

[1] J. W. M. Baars, *The Paraboloidal Reflector Antenna in Radio Astronomy and Communication: Theory and Practice*, ser. Astrophysics and Space Science Library. Springer New York, 2007, ISBN: 9780387697345.

[2] T. L. Wilson, K. Rohlfs, and S. Hüttemeister, *Tools of Radio Astronomy*, 6th Edition, A. Library and Astrophysics, Eds. Springer, 2013, ISBN: 9783642399497.

[3] W. A. van Cappellen *et al.*, "Apertif: Phased array feeds for the Westerbork Synthesis Radio Telescope. System overview and performance characteristics", *Astronomy & Astrophysics*, vol. 658, no. A146, Feb. 2022.

[4] M. De Vos, A. W. Gunst, and R. Nijboer, "The LOFAR telescope: System architecture and signal processing", *Proceedings of the IEEE*, vol. 97, no. 8, pp. 1431–1437, 2009.

[5] P. S. Kildal, L. A. Baker, and T. Hagfors, "The Arecibo Upgrading: Electrical Design and Expected Performance of the Dual-Reflector Feed System", *Proceedings of the IEEE*, vol. 82, no. 5, pp. 714–724, 1994.

[6] D. Li *et al.*, "The Five-hundred-meter Aperture Spherical Radio Telescope (FAST) project", in *International Topical Meeting on Microwave Photonics (MWP)*, Paphos, Cyprus, Oct. 2015.

[7] J. Schleeh, N. Wadefalk, P. A. Nilsson, and J. Grahn, "10 K room temperature LNA for SKA band 1", in *IEEE MTT-S Int. Microw. Symp. Dig. (IMS 2016)*, San Francisco, CA, USA, Aug. 2016.

[8] J. Flygare *et al.*, "Wideband single pixel feed system over 4.6-24 GHz for the Square Kilometre Array", in *2019 Int. Conf. Electromagn. Adv. Appl. (ICEAA)*, Granada, Spain, Sep. 2019, pp. 0630–0635.

[9] J. Schleeh *et al.*, "Cryogenic LNAs for SKA band 2 to 5", in *IEEE MTT-S Int. Microw. Symp. Digest (IMS 2017)*, Honololu, HI, USA, Jun. 2017, pp. 164–167.

[10] N. Wadefalk, P.-S. Kildal, and H. Zirath, "A low noise integrated 0.3-16 GHz differential amplifier for balanced ultra wideband antennas", in *Tech. Dig. IEEE Compound Semicond. Integrated Circuit Symp. (CSIC 2010)*, 2010, pp. 3–6.

[11] A. H. Akgiray *et al.*, "Noise measurements of discrete HEMT transistors and application to wideband very low-noise amplifiers", *IEEE Trans. Microw. Theory Techn.*, vol. 61, no. 9, pp. 3285–3297, 2013.

[12] J. Schleeh *et al.*, "Cryogenic 0.5-13 GHz low noise amplifier with 3 K mid-band noise temperature", in *IEEE MTT-S Int. Microw. Symp. Dig. (IMS 2012)*, Montreal, QC, Canada, 2012, pp. 15–17.

[13] S. Weinreb and J. Shi, "Low Noise Amplifier With 7-K Noise at 1.4 GHz and 25 °C", *IEEE Trans. Microw. Theory Techn.*, vol. 69, no. 4, pp. 2345–2351, Apr. 2021.

[14] R. Lehmensiek and I. P. Theron, "L-band feed horn and orthogonal mode transducer for the KAT-7 radio telescope", *IEEE Trans. Antennas Propag.*, vol. 59, no. 6, pp. 1894–1901, Jun. 2011.

[15] T. E. Hassall *et al.*, "Wide-band simultaneous observations of pulsars: Disentangling dispersion measure and profile variations", *Astronomy and Astrophysics*, vol. 543, 2012.

[16] A. L. Fey *et al.*, "The second realization of the international celestial reference frame by very long baseline interferometry", *Astronomical Journal*, vol. 150, no. 2, 2015.

[17] A. Pasetto *et al.*, "Broadband radio spectro-polarimetric observations of high Faraday rotation measure AGN", *Astronomy & Astrophysics*, vol. 613, no. 1998, A74, Jan. 2018.

[18] A. E. Niell *et al.*, "VLBI2010: Current and future requirementsfor geodetic VLBI systems (WG3—final report)", In 2005 IVS Annual Report NASA/TP-2006-214136. International VLBI Service for Geodesy and Astrometry (IVS), 2005. [Online]. Available: `https://ivscc.gsfc.nasa.gov/about/wg/wg3/IVS_WG3_report_050916.pdf`.

[19] B. Petrachenko *et al.*, "Design Aspects of the VLBI2010 System", In Progress Report of the IVS VLBI2010 Commitee, NASA/TM-2009-214180, 2009. [Online]. Available: `https://ntrs.nasa.gov/search.jsp?R=20090034177`.

[20] G. Elgered *et al.*, "The Onsala Twin Telescopes Project", in *Proc. 23rd Working Meeting of the Euro. Very Long Baseline Interferometry Group for Geodesy and Astrometry (EVGA 2017)*, EVGA, 2017.

[21] G. Hallinan *et al.*, "The DSA-2000 - A Radio Survey Camera", *Bull. AAS (Astro2020 APC White Paper)*, vol. 51, no. 7, Sep. 2019. [Online]. Available: `https://baas.aas.org/pub/2020n7i255`.

[22] L. Connor *et al.*, "Galactic Radio Explorer: An All-sky Monitor for Bright Radio Bursts", *Publ. Astron. Soc. Pacific*, vol. 133 075001, no. 1025, Jul. 2021.

[23] P. E. Dewdney *et al.*, "SKA1 System Baseline Design (SKA-TEL-SKO-DD-001)", SKA Organisation, Mar. 2013. [Online]. Available: `https://www.skatelescope.org/wp-content/uploads/2012/07/SKA-TEL-SKO-DD-001-1_BaselineDesign1.pdf`.

[24] I. P. Theron, R. Lehmensiek, and D. I. L. de Villiers, "The design of the MeerKAT dish optics", in *Proc. Int. Conf. Electromagn. Advanced Appl. (ICEAA 2012)*, Sep. 2012, pp. 539–542.

[25] A. Pellegrini *et al.*, "Mid-radio telescope, single pixel feed packages for the square kilometer array: An overview", *IEEE J. Microw.*, vol. 1, no. 1, pp. 428–437, Jan. 2021.

[26] J. Flygare *et al.*, "Sensitivity simulation and measurement of the SKA Band 1 wideband feed package on MeerKAT", in *Proc. 13th Eur. Conf. Antennas Propag. (EuCAP)*, Krakow, Poland, Apr. 2019.

[27] B. Dong *et al.*, "Optimization and Realization of Quadruple-ridge Flared Horn with New Spline-defined Profiles as a High-efficiency Feed over 4.6-24 GHz", *IEEE Trans. Antennas Propag.*, vol. 67, no. 1, pp. 585–590, Jan. 2019.

[28] W. J. Welch *et al.*, "New cooled feeds for the allen telescope array", *Publ. Astron. Soc. Pacific*, vol. 129 045002, no. 974, Mar. 2017.

[29] M. McKinnon, C. Carilli, and T. Beasley, "The next generation very large array", in *Proc. SPIE*, vol. 9906, Jul. 2016, p. 990 627.

[30] R. Lehmensiek and D. I. L. de Villiers, "An Optimal 18 m Shaped Offset Gregorian Reflector for the ngVLA Radio Telescope", *IEEE Trans. Antennas Propag.*, vol. 69, no. 12, pp. 8282–8290, Dec. 2021.

[31] S. Weinreb *et al.*, "Cryogenic 1.2 to 116 GHz Receiver for Large Arrays", in *Proc. 12th Euro. Conf. Antennas Propag. (EuCAP)*, London, UK, Apr. 2018.

[32] G. Tuccari *et al.*, "BRAND: A very wide-band receiver for the EVN", in *Proc. 23th Eur. VLBI Group Geodesy Astrometry Work. Meeting (EVGA)*, Gothenburg, Sweden, May 2017, pp. 81–83. [Online]. Available: `https://publications.lib.chalmers.se/records/fulltext/253604/local_253604.pdf`.

[33] J. Yang, "Calculation of Aperture Efficiency of Reflector Antenna with the Measured Far-field Function of its Feed in Ludwig's Third Definition", in *15th Eur. Conf. Antennas Propag. (EuCAP)*, Dusseldorf, Germany, Mar. 2021.

[34] P.-S. Kildal, J. Yang, and M. Ivashina, "New BOR1 and Decoupling Efficiencies for Characterizing Ultra-Wideband Reflectors and Feeds for Future Radio Telescopes", in *Proc. 5th Euro. Conf. Antennas Propag. (EuCAP 2011)*, Rome, Italy, Apr. 2011, pp. 3712–3714.

[35] J. Yang *et al.*, "Cryogenic 2-13 GHz eleven feed for reflector antennas in future wideband radio telescopes", *IEEE Trans. Antennas Propag.*, vol. 59, no. 6, pp. 1918–1934, Jun. 2011.

[36] J. Yang, M. Pantaleev, P.-S. Kildal, and L. Helldner, "Design of compact dual-polarized 1.2-10 GHz eleven feed for decade bandwidth radio telescopes", *IEEE Trans. Antennas Propag.*, vol. 60, no. 5, pp. 2210–2218, May 2012.

[37] G. Cortes-Medellin, "Non-planar quasi-self-complementary ultra-wideband feed antenna", *IEEE Trans. Antennas Propag.*, vol. 59, no. 6, pp. 1935–1944, Jun. 2011.

[38] K. A. Abdalmalak *et al.*, "Ultrawideband Conical Log-Spiral Circularly Polarized Feed for Radio Astronomy", *IEEE Trans. Antennas Propag.*, vol. 68, no. 3, pp. 1995–2007, Mar. 2020.

[39] A. Akgiray, S. Weinreb, W. A. Imbriale, and C. Beaudoin, "Circular quadruple-ridged flared horn achieving near-constant beamwidth over multioctave bandwidth: Design and measurements", *IEEE Trans. Antennas Propag.*, vol. 61, no. 3, pp. 1099–1108, Mar. 2013.

[40] A. H. Akgiray, "New technologies driving decade-bandwidth radio astronomy : quad-ridged flared horn and compound-semiconductor LNAs", PhD thesis, California Institute of Technology (Caltech), 2013. [Online]. Available: `http://thesis.library.caltech.edu/7644/`.

[41] T. S. Beukman, P. Meyer, M. V. Ivashina, and R. Maaskant, "Modal-based design of a wideband quadruple-ridged flared horn antenna", *IEEE Trans. Antennas Propag.*, vol. 64, no. 5, pp. 1615–1626, May 2016.

[42] T. S. Beukman, "Modal-Based Design Techniques for Circular Quadruple-Ridged Flared Horn Antennas", PhD thesis, Stellenbosch University, 2015. [Online]. Available: `http://hdl.handle.net/10019.1/96948`.

[43] T. S. Beukman, P. Meyer, M. V. Ivashina, and R. Maaskant, "Modal-based design of a wideband quadruple-ridged flared horn antenna", *IEEE Trans. Antennas Propag.*, vol. 64, no. 5, pp. 1615–1626, 2016.

[44] K. Kotze and P. Meyer, "Improving Modal Purity in Quadraxially Fed Quadruple-Ridged Flared Horn Antennas", in *Proc. 14th Euro. Conf. Antennas Propag. (EuCAP)*, Mar. 2020.

[45] T. Satoh, "Dielectric-loaded horn antenna", *IEEE Trans. Antennas Propag.*, vol. 20, no. 2, pp. 199–201, 1972.

[46] H. Lai, R. Franks, D. Kong, D. Kuck, and T. Gackstetter, "A broad band high efficent quad ridged horn", in *1987 Antennas and Propagation Society International Symposium*, vol. 25, 1987, pp. 676–679.

[47] R. J. Bauerle, R. Schrimpf, E. Gyorko, and J. Henderson, "The Use of a Dielectric Lens to Improve the Efficiency of a Dual-Polarized Quad-Ridge Horn From 5 to 15 GHz", *IEEE Trans. Antennas Propag.*, vol. 57, no. 6, pp. 1822–1825, 2009.

[48] A. Dunning, M. Bowen, M. Bourne, D. Hayman, and S. L. Smith, "An ultra-wideband dielectrically loaded quad-ridged feed horn for radio astronomy", in *Proc. IEEE-APS Conf. Antennas Propag. Wireless Communic. (APWC 2015)*, Turin, Italy, Sep. 2015, pp. 787–790.

[49] K. W. Smart *et al.*, "Pattern Measurements of Cryogenically Cooled Ultra-Wideband Feed Horn", *13th European Conference on Antennas and Propagation (EuCAP)*, 2019.

[50] C. A. Balanis, *Modern Antenna Handbook*. New York, NY, USA: Wiley-Interscience, 2008, ISBN: 9780470036341.

[51] P.-S. Kildal, *Foundations of Antennas - A Unified Approach for Line-Of-Sight and Multipath*. 2014, ISBN: 9789004310087.

[52] D. M. Pozar, *Microwave Engineering*, 4th Edition. Wiley, 2012, ISBN: 9780470631553.

[53] C. A. Balanis, *Antenna Theory: Analsysi and Design*. New York, NY, USA: Wiley-Interscience, 2005, ISBN: 0471714623.

[54] B. Dong, J. Yang, M. Pantaleev, J. Flygare, and B. Billade, "Design of an Asymmetrical Quadruple-ridge Flared Horn Feed : a Solution to Eliminate Polarization Discrepancy in the Offset Reflecting Systems", in *Proc. 12th Euro. Conf. Antennas Propag. (EuCAP)*, London, UK, Apr. 2018.

[55] T. Carozzi and J. Flygare, "Enhancing SKA Band 1 Polarimetry by Using Two Different Feed Rotations", in *Proc. 2nd URSI Atlantic Radio Sci. Meeting (AT-RASC)*, Gran Canaria, Spain, Jun. 2018.

[56] R. Lehmensiek, I. P. Theron, and D. I. De Villiers, "Deriving an Optimum Mapping Function for the SKA-Shaped Offset Gregorian Reflectors", *IEEE Trans. Antennas Propag.*, vol. 63, no. 11, pp. 4658–4666, 2015.

[57] IEEE, "IEEE Standard for Definitions of Terms for Antennas (IEEE Std 145)", IEEE Antennas and Propagation Society, Tech. Rep., 2013.

[58] P.-S. Kildal, "Factorization of the feed Efficiency of Paraboloids and Cassegrain Antennas", *IEEE Trans. Antennas Propag.*, vol. 33, no. 8, pp. 903–908, 1985.

[59] G. Cortes-Medellin, "MEMO 95 Antenna noise temperature calculation", SKA Memo, Jul. 2007, pp. 1–13. [Online]. Available: `https://www.skatelescope.org/uploaded/6967_Memo_95.pdf`.

[60] G. J. Hovey, R. Messing, A. G. Willis, and B. Veidt, "An automated system for measurement of sensitive microwave radiometers", in *18th International Symposium on Antenna Technology and Applied Electromagnetics (ANTEM)*, Aug. 2018.

[61] D. I. De Villiers and R. Lehmensiek, "Rapid calculation of antenna noise temperature in offset gregorian reflector systems", *IEEE Trans. Antennas Propag.*, vol. 63, no. 4, pp. 1564–1571, 2015.

[62] J. Welch *et al.*, "The Allen Telescope Array: The First Widefield, Panchromatic, Snapshot Radio Camera for Radio Astronomy and SETI", *Proceedings of the IEEE*, vol. 97, no. 8, pp. 1438–1447, Aug. 2009.

[63] T. D. Carozzi and G. Woan, "A fundamental figure of merit for radio polarimeters", *IEEE Trans. Antennas Propag.*, vol. 59, no. 6, pp. 2058–2065, Jun. 2011.

[64] S. B. Cohn, "Properties of Ridge Wave Guide", *Proceedings of the IRE*, vol. 35, no. 8, pp. 783–788, 1947.

[65] S. Hopfer, "The Design of Ridged Waveguides", *IRE Transactions on Microwave Theory and Techniques*, vol. 3, no. 5, pp. 20–29, 1955.

[66] M. H. Chen, G. N. Tsandoulas, and F. G. Willwerth, "Modal Characteristics of Quadruple-Ridged Circular and Square Waveguides", *IEEE Trans. Microw. Theory Techn.*, vol. 22, no. 8, pp. 801–804, 1974.

[67] J. Helszajn, *Ridge Waveguides and Passive Microwave Components*, ser. Electromagnetic Waves. Institution of Engineering and Technology, 2000, ISBN: 9780852967942.

[68] Zhongxiang Shen and Chao Feng, "A new dual-polarized broadband horn antenna", *IEEE Antennas and Wireless Propagation Letters*, vol. 4, no. 1, pp. 270–273, 2005.

[69] V. Rodriguez, "An open-boundary quad-ridged guide horn antenna for use as a source in antenna pattern measurement anechoic chambers", *IEEE Antennas and Propagation Magazine*, vol. 48, pp. 157–160, 2 Apr. 2006.

[70] D. I. D. Villiers, P. Meyer, and K. D. Palmer, "Design of a wideband orthomode transducer", in *IEEE AFRICON Conference*, 2009.

[71] A. Akgiray and S. Weinreb, "Ultrawideband square and circular quad-ridge horns with near-constant beamwidth", in *Proc. IEEE International Conference on Ultra-Wideband*, Syracuse, NY, USA, 2012, pp. 518–522.

[72] B. Billade, J. Flygare, M. Dahlgren, B. Wästberg, and M. Pantaleev, "A wide-band feed system for SKA band 1 covering frequencies from 350 - 1050 MHz", in *Proc. 10th Euro. Conf. Antennas Propag. (EuCAP)*, Davos, Switzerland, Apr. 2016.

[73] J. Shi, S. Weinreb, W. Zhong, X. Yin, and M. Yang, "Quadruple-Ridged Flared Horn Operating From 8 to 50 GHz", *IEEE Trans. Antennas Propag.*, vol. 65, no. 12, pp. 7322–7327, Dec. 2017.

[74] A. Dunning, M. Bowen, and Y. Chung, "Offset quad ridged orthomode transducer with a 3.4:1 bandwidth", in *Asia-Pacific Microwave Conference Proceedings, APMC*, 2013, pp. 146–148.

[75] Dassault Systemes, *Cst studio suite*, 2022. [Online]. Available: `https://www.3ds.com/products-services/simulia/products/cst-studio-suite/`.

[76] J. Kennedy and R. Eberhart, "Particle swarm optimization", in *Proc. IEEE International Conference on Neural Networks (ICNN 2015)*, Perth, WA, Australia, 1995, pp. 1942–1948.

[77] MathWorks, *Matlab*, 2022. [Online]. Available: `https://se.mathworks.com/products/matlab.html`.

[78] AutoDesk, *Inventor*, 2022. [Online]. Available: `https://www.autodesk.com/products/inventor`.

[79] M. V. Ivashina, O. Iupikov, R. Maaskant, W. A. Van Cappellen, and T. Oosterloo, "An optimal beamforming strategy for wide-field surveys with phased-array-fed reflector antennas", *IEEE Trans. Antennas Propag.*, vol. 59, no. 6, pp. 1864–1875, 2011.

[80] G. H. Tan *et al.*, "An innovative, highly sensitive receiver system for the Square Kilometre Array Mid Radio Telescope", vol. 9906, no. 990660, Jul. 2016.

[81] W. A. Imbriale, "Faster antenna noise temperature calculations using a novel approximation technique", in *IEEE International Symposium on Antennas and Propagation and CNC-USNC/URSI Radio Science Meeting (APSURSI 2010)*, 2010.

[82] W. D. Burnside and C. W. Chuang, "An Aperture-Matched Horn Design", *IEEE Trans. Antennas Propag.*, vol. 30, no. 4, pp. 790–796, 1982.

[83] Surtec, *Surtec 650*, 2022. [Online]. Available: `https://www.surtec.com/en/products-services/surtec-650/`.

[84] Mill-Max Corp., *Gold-plated press-fit receptacle*, 2022. [Online]. Available: `https://www.mill-max.com/products/receptacle/0366/0366-0-15-15-13-27-10-0`.

[85] A. Algaba Brazalez *et al.*, "Design of F-Band Transition from Microstrip to Ridge Gap Waveguide Including Monte Carlo Assembly Tolerance Analysis", *IEEE Trans. Microw. Theory Techn.*, vol. 64, no. 4, pp. 1245–1254, Apr. 2016.

[86] A. C. Ludwig, "The Definition of Cross Polarization", *IEEE Trans. Antennas Propag.*, vol. 21, no. 1, pp. 116–119, 1973.

[87] D. G. Bodnar, "Standard Gain Horn Computations Versus Measured Data", in *14th International Symposium on Antenna Technology and Applied Electromagnetics & the American Electromagnetics Conference*, Ottawa, ON, Canada, 2010.

[88] B. Derat, "5G antenna characterization in the far-field: How close can far-field be?", in *IEEE International Symposium on Electromagnetic Compatibility and IEEE Asia-Pacific Symposium on Electromagnetic Compatibility (EMC/APEMC)*, Suntec City, Singapore, May 2018, pp. 959–962.

[89] B. Derat, G. F. Hamberger, and F. Michaelsen, "On the Minimum Range Length for Performing Accurate Direct Far-Field Over-the-Air Measurements", in *2019 Antenna Measurement Techniques Association Symposium (AMTA)*, San Diego, CA, USA, Oct. 2019.

[90] J. Flygare *et al.*, "Beam pattern measurement on offset Gregorian reflector mounted with a wideband room temperature receiver for the Square Kilometre Array", in *2018 IEEE Int. Symp. Antennas Propag. & USNC/URSI Nat. Radio Sci. Meeting (APSURSI)*, Boston, MA, USA, Jul. 2018, pp. 1759–1760.

[91] R. Maaskant, D. J. Bekers, M. J. Arts, W. A. Van Cappellen, and M. V. Ivashina, "Evaluation of the radiation efficiency and the noise temperature of low-loss antennas", *IEEE Antennas Wireless Propag. Lett.*, vol. 8, pp. 1166–1170, 2009.

[92] D. M. Pozar and B. Kaufman, "Comparison of Three Methods for the Measurement of Printed Antenna Efficiency", *IEEE Trans. Antennas Propag.*, vol. 36, no. 1, pp. 136–139, 1988.

[93] A. Akgiray, S. Weinreb, and W. Imbriale, "Design and measurements of dual-polarized wideband constant-beamwidth quadruple-ridged flared horn", in *IEEE Antennas and Propagation Society, AP-S International Symposium (Digest)*, 2011, pp. 1135–1138.

[94] G. Hobbs *et al.*, "An ultra-wide bandwidth (704 to 4 032 mhz) receiver for the parkes radio telescope", *Publications of the Astronomical Society of Australia*, vol. 37, no. E012, 2020.

[95] K. Vanderlinde *et al.*, "LRP 2020 Whitepaper: The Canadian Hydrogen Observatory and Radio-transient Detector (CHORD)", *Canadian Astronomical Society (LRP2020 White Paper)*, Nov. 2019. [Online]. Available: `http://arxiv.org/abs/1911.01777`.

[96] J. Krupka, "Measurements of the Complex Permittivity of Low Loss Polymers at Frequency Range From 5 GHz to 50 GHz", *IEEE Microwave and Wireless Components Letters*, vol. 26, no. 6, pp. 464–466, Jun. 2016.

[97] V. L. Lanza and D. B. Herrmann, "The density dependence of the dielectric constant of polyethylene", *Journal of Polymer Science*, vol. 28, no. 118, pp. 622–625, 1958.

[98] A. M. Nicolson and G. F. Ross, "Measurement of the Intrinsic Properties of Materials by Time-Domain Techniques", *IEEE Transactions on Instrumentation and Measurement*, vol. 19, no. 4, pp. 377–382, Nov. 1970.

[99] W. Weir, "Automatic measurement of complex dielectric constant and permeability at microwave frequencies", *Proceedings of the IEEE*, vol. 62, no. 1, pp. 33–36, 1974.

[100] J. W. Lamb, "Miscellaneous data on materials for millimetre and submillimetre optics", *International Journal of Infrared and Millimeter Waves*, vol. 17, pp. 1997–2034, 12 1997.

[101] B. Riddle, J. Baker-Jarvis, and J. Krupka, "Complex permittivity measurements of common plastics over variable temperatures", *IEEE Trans. Microw. Theory Techn.*, vol. 51, no. 3, pp. 727–733, 2003.

[102] Rexolite, *REXOLITE 1422*, 2022. [Online]. Available: `http://www.rexolite.com/specifications/` (visited on 02/09/2022).

[103] Laird, *Eccostock HiK - K=3.5*, 2022. [Online]. Available: `https://www.laird.com/products/microwave-absorbers/low-loss-dielectrics/eccostock-hik` (visited on 02/09/2022).

[104] Avient, *Preperm Standard Grade - PPE260*, 2022. [Online]. Available: `https://www.preperm.com/products/raw-materials/` (visited on 02/09/2022).

[105] ——, *Preperm Standard Grade - PPE350*, 2022. [Online]. Available: `https://www.preperm.com/products/raw-materials/` (visited on 02/09/2022).

[106] Victrex, *Peek 90g*, 2022. [Online]. Available: `https://www.victrex.com/-/media/downloads/literature/en/material-properties-guide%5C_us-4-20.pdf` (visited on 02/09/2022).

[107] Ensinger, *TECASINT 2011 - Datasheet*, 2022. [Online]. Available: `https://www.ensingerplastics.com/en/shapes/products/polyimide-tecasint-2011-natural` (visited on 02/09/2022).

[108] DuPont, *Vespel SP-1*, 2022. [Online]. Available: `https://www.dupont.com/content/dam/dupont/amer/us/en/vespel/public/documents/en/VPE-A10861-00-B0614.pdf` (visited on 02/09/2022).

[109] H. Manh Cuong, N. Trong Duc, and V. Van Yem, "Measurement of Complex Permittivity of Materials Using Electromagnetic Wave Propagation in Free Space and Super High-Resolution Algorithm", in *2017 International Conference on Advanced Technologies for Communications (ATC)*, Quy Nhon, Vietnam, Oct. 2017, pp. 156–160.

[110] Heraeus, *Hsg fused quartz*, 2022. [Online]. Available: `https://www.heraeus.com/media/media/hca/doc_hca/products_and_solutions_8/rods/Quartz_Rods_EN.pdf`.